

<sup>1</sup>

## Analysis Note

# Measurement of charged particle production in diffractive proton-proton collisions at $\sqrt{s} = 200$ GeV with tagging of the forward scattered proton

Leszek Adamczyk<sup>1</sup>, Łukasz Fulek<sup>1</sup>, Mariusz Przybycień<sup>1</sup>, and Rafał Sikora<sup>1</sup>

<sup>1</sup>*AGH University of Science and Technology, FPACS, Kraków, Poland*

<sup>2</sup>

23rd November 2020

In this note we present the analysis of the Single Diffractive Dissociation process with the STAR Roman Pot (RP) detectors at RHIC. The measurement is focused on the charged particle multiplicity, its dependence on the transverse momentum and pseudorapidity in three regions of  $\xi$ :  $0.02 < \xi < 0.05$ ,  $0.05 < \xi < 0.1$  and  $0.1 < \xi < 0.2$ . The identified particle to antiparticle (pion, kaon, proton and their antiparticle) multiplicity ratios as a function of transverse momentum in above three  $\xi$  regions are also measured. The data come from proton-proton collisions collected in 2015. The forward proton was tagged in the STAR Roman Pot system while the charged particle tracks were reconstructed in the STAR Time Projection Chamber (TPC). We describe all stages of the analysis involving comparison of the data with MC simulations and systematic uncertainty studies. More technical parts of the analysis are described in a supplementary analysis note [1].

<sup>3</sup> **List of contributions**

---

Leszek Adamczyk	Analysis coordination/supervision, production of picoDST, production of embedded MC samples
Lukasz Fulek*	Main analyzer, write-up author
Mariusz Przybycień	Analysis supervision
Rafal Sikora	Analysis support

---

<sup>7</sup> \* - contact editor

<sup>9</sup> **Change log**

---

23rd Novem-	ver. 1.0	Initial revision
ber		
2020		

---

# Contents

14	<b>List of contributions</b>	<b>2</b>
16	<b>Change log</b>	<b>2</b>
17	<b>1 Introduction</b>	<b>1</b>
18	<b>2 Monte Carlo Samples</b>	<b>2</b>
19	<b>3 Data Sample and Event Selection</b>	<b>4</b>
20	3.1 Track Selection . . . . .	5
21	3.2 Fiducial Region of the Measurement . . . . .	8
22	<b>4 Background Contribution</b>	<b>11</b>
23	4.1 Background from Non-Primary Tracks . . . . .	13
24	4.2 Control Plots . . . . .	20
25	<b>5 Selection Efficiencies</b>	<b>24</b>
26	5.1 Vertex Reconstruction . . . . .	24
27	5.2 Correction to BBC-Small . . . . .	29
28	<b>6 Migrations into and out of the Fiducial Region</b>	<b>33</b>
29	6.1 Migrations of Tracks into and out of the Fiducial Region . . . . .	33
30	6.2 Migrations in $\xi$ . . . . .	34
31	<b>7 Event Corrections and Unfolding Procedure</b>	<b>37</b>
32	7.1 Correction to $dN/dn_{\text{sel}}$ . . . . .	37
33	7.2 Correction to Transverse Momentum and Pseudorapidity Distributions . . . . .	40
34	7.3 Closure Tests . . . . .	41
35	7.4 EAST-WEST asymmetry . . . . .	41
36	7.5 Particle Identification . . . . .	42
37	7.6 Antiparticle-to-Particle Ratios . . . . .	48
38	<b>8 Systematic Uncertainties</b>	<b>49</b>
39	<b>9 Results</b>	<b>54</b>
40	9.1 Comparison of Charged-Particle Densities at Central Rapidities . . . . .	61
41	<b>10 Kaon to Pion Ratio</b>	<b>63</b>
42	<b>11 Summary and Conclusions</b>	<b>64</b>
43	<b>Appendices</b>	<b>67</b>
44	<b>A Proton and Antiproton DCA Distributions</b>	<b>68</b>



<sup>46</sup> **Acronyms**

<sup>47</sup>	<b>CD</b>	Central Diffraction
<sup>48</sup>	<b>DD</b>	Double Diffraction
<sup>49</sup>	<b>MBR</b>	Minimum Bias Rockefeller
<sup>50</sup>	<b>MC</b>	Monte Carlo
<sup>51</sup>	<b>ND</b>	Non-Diffractive
<sup>52</sup>	<b>QCD</b>	Quantum Chromodynamics
<sup>53</sup>	<b>RP</b>	Roman Pot
<sup>54</sup>	<b>SaS</b>	Schuler and Sjöstrand
<sup>55</sup>	<b>SD</b>	Single Diffraction
<sup>56</sup>	<b>TPC</b>	Time Projection Chamber

# 1. Introduction

Inclusive measurements of charged-particle distributions in proton–proton ( $pp$ ) collisions probe the strong interaction in the low-momentum transfer, non-perturbative regime of Quantum Chromodynamics (QCD). In this kinematic region interactions are usually described by phenomenological models implemented in Monte Carlo (MC) event generators. Measurements can be used to constrain the free parameters of these models. An accurate description of low-energy strong interaction processes is essential for understanding and precise simulation of different types of  $pp$  processes and the effects of multiple  $pp$  collisions in the same bunch crossing at high instantaneous luminosity at hadron colliders. Measurements with tagging of the forward-scattered proton are of special interest. They give direct access to specific but still significant part of  $pp$  processes called diffraction. In addition precise modelling of forward particle production is essential for better understanding of the longitudinal development of air showers observed in experiments studying cosmic radiation.

We present a measurement of charged particle production in events with single forward proton tagging (dominated by Single Diffraction (SD):  $p + p \rightarrow p + X$ ). The following observables are studied:

$$\frac{1}{N_{\text{ev}}} \frac{dN_{\text{ev}}}{dn_{\text{ch}}}, \quad \frac{1}{N_{\text{ev}}} \frac{1}{2\pi p_{\text{T}}} \frac{d^2 N}{d\bar{\eta} dp_{\text{T}}}, \quad \frac{1}{N_{\text{ev}}} \frac{dN}{d\bar{\eta}} \quad (1.1)$$

where  $n_{\text{ch}}$  is the number of primary charged particles within kinematic range given by  $p_{\text{T}} > 200$  MeV and  $|\eta| < 0.7$ ,  $N_{\text{ev}}$  is the total number of events with  $2 \leq n_{\text{ch}} \leq 8$ ,  $N$  is the total number of charged particles within the above kinematic acceptance and  $\bar{\eta}$  is the pseudorapidity of the charged particle with longitudinal momentum taken with respect to direction of the forward scattered proton. To suppress non-SD events the trigger system required no signal in BBC-small in the direction of forward scattered proton and signal in BBC-small in opposite direction. The measurements are performed in a fiducial phase space of the forward scattered protons of  $0.04 < -t < 0.16$  GeV $^2/c^2$  and  $0.02 < \xi < 0.2$ , where  $\xi$  is the fractional energy loss of the scattered proton and  $t$  is the squared four momentum transfer. In case of SD process  $\xi = M_X^2/s$ , where  $M_X$  is the mass of the state  $X$  into which one of the incoming proton dissociates and  $s$  is the center of mass energy squared of the  $pp$  system. The Mandelstam variable  $t$  is defined by  $t = (p_1 - p_3)^2$ , where  $p_1$  is the four-momentum of the incoming proton,  $p_3$  is the four-momentum of the outgoing proton. The above mentioned observables are presented in three  $\xi$  regions:  $0.02 < \xi < 0.05$ ,  $0.05 < \xi < 0.1$  and  $0.1 < \xi < 0.2$ . In addition their average values are presented as a function of  $\xi$ .

We have also studied an identified particle to antiparticle (pion, kaon, proton and their anti-particle) multiplicity ratios as a function of  $p_{\text{T}}$  also in the above mentioned three regions of  $\xi$ . The system  $X$  into which proton diffractively dissociates has net charge and baryon number +1. It is believed that initial charge and barion number should appear in the very forward direction leading to the equal amount of particles and antiparticles in the central region created by fragmentation and hadronization processes. However other scenarios are also possible where extra baryon is uniformly distributed over rapidity [2] or even appear close to the gap edge [3]. It is natural to expect that possible charge and baryon number transfer to central region will be better visible at small  $\xi$  where amount of particle-antiparticle creation is smaller due to the generally smaller particle multiplicity or due to the fact that gap edge is inside our fiducial region of  $|\eta| < 0.7$ .

## 98 2. Monte Carlo Samples

99 MC samples used to correct data for detector effects were obtained by the embedding MC technique  
100 [4], in which simulated particles are mixed with the real Zerobias events at the raw data  
101 level. Zerobias data events used in the embedding were sampled over the entire data-taking period  
102 in order to properly describe the data set used in the analysis. Two samples of embedding MC  
103 were produced:

- 104 1. Single particle MC, in which particles are generated from flat distributions in  $\eta$  and  $p_T$ , in  
105 order to have similar statistics in all bins.
- 106 2. The Schuler and Sjöstrand (SaS) model implemented in PYTHIA 8 with 4C tune.

107 Generated particles were passed through the full simulation of the STAR TPC and RP system  
108 detectors using GEANT3 and GEANT4, respectively, and then embedded into real data sample.  
109 These embedding events were next processed through the full event reconstruction chain.

110 It is preferred to get the detector corrections from a MC, which is dedicated to simulate  
111 the studied physics process. However, for this purpose, the statistics in the MC should be several  
112 times greater than in the analysed data sample. Since this is not possible with low efficiency of  
113 TPC and TOF, the basic method of corrections used in the analysis for  $p_T$  and  $\bar{\eta}$  distributions  
114 is a method of factorization of global efficiency into the product of single-particle efficiencies. In  
115 this way, statistically precise multidimensional corrections on TPC and TOF were obtained from  
116 the single particle MC. The energy loss correction was also determined from the same MC sample.  
117 The charged-particle multiplicity distributions were unfolded from the measured multiplicities of  
118 TPC tracks based on the response matrix, which takes into account all detector effects. In this  
119 procedure single particle MC samples were not used.

120 All other detector corrections were obtained from PYTHIA 8 4C (SaS). In order to keep  
121 statistical precision coming from the corrections high, samples filtered on true-level values of  $\xi$   
122 and  $t$  (not necessarily with reconstructed proton track in RP) are used.

123 Several additional MC samples were generated, in which simulated particles were propagated  
124 through full simulation and reconstruction chain but were not embedded into Zerobias events.  
125 Systematic uncertainty related to hadronization of the diffractive system was determined by using  
126 alternative hadronization models as implemented in HERWIG and EPOS. Results are compared  
127 to model predictions from PYTHIA 8 4C (SaS), HERWIG, EPOS and alternative PYTHIA 8  
128 model Minimum Bias Rockefeller (MBR) with A2 tune. EPOS predicts very large contribution  
129 of forward protons, which originate from Non-Diffractive (ND) events and are well separated in  
130 rapidity from other final state particles. This is the result of low mass excitation of the proton  
131 remnant ( $< 1$  GeV) leading to hadronization of the beam remnant back to the proton. Therefore  
132 EPOS predictions were separated in two classes: diffractive (EPOS SD) modelled by Pomeron  
133 exchange and ND modelled by low mass excitation of the proton remnant (EPOS SD'). Such  
134 remnant treatment is very unique in EPOS compared to other string models, especially, to that  
135 used in PYTHIA 8, where ND forward protons are rare and arise from string fragmentation and  
136 hadronization. In all PYTHIA 8 models, diffractive cross-sections are scaled by the factors, which  
137 were introduced in order to describe the full phase space [5, 6]. In the SaS model, the scaling  
138 factors for SD and DD,  $F_{SD}$  and  $F_{DD}$ , are defined as a function of diffractive masses:

$$F_{SD} = \left(1 - \frac{M^2}{s}\right) \left(1 + \frac{c_{res} M_{res}^2}{M_{res}^2 + M^2}\right) \quad (2.1)$$

$$F_{DD} = \left(1 - \frac{M_a^2 + M_b^2}{s}\right) \left(\frac{sm_p^2}{sm_p^2 + M_a^2 M_b^2}\right) \times \left(1 + \frac{c_{res} M_{res}^2}{M_{res}^2 + M_a^2}\right) \left(1 + \frac{c_{res} M_{res}^2}{M_{res}^2 + M_b^2}\right) \quad (2.2)$$

139 where  $M$  and  $M_a, M_b$  are the invariant masses of the systems  $X$  and  $X_a, X_b$  for SD and DD,  
140 respectively,  $c_{\text{res}} = 2$  and  $M_{\text{res}} = 2 \text{ GeV}/c^2$  were obtained from a fit to  $pp/\bar{p}p$  data [5]. On  
141 the other hand, in the MBR model the scaling factor is given as a function of the rapidity gap [6]:  
142

$$S = \frac{1}{2} \left[ 1 + \text{erf} \left( \frac{\Delta y - \Delta y_S}{\sigma_S} \right) \right] \quad (2.3)$$

143 where  $\Delta y$  is the rapidity gap,  $\Delta y_S = 2$  and  $\sigma_S = 0.5$ . As a result, diffractive cross sections are  
144 artificially suppressed at relatively large values of  $\xi (> 0.05)$ . This artificial suppression significantly  
145 changes predicted distribution of  $\xi$  and fractions of different processes in our fiducial phase space.  
146 Therefore data is also compared with expectations obtained without suppression of the diffractive  
147 cross sections (MBR-tuned).  
148

149 Figure 2.1 (left) shows the distribution of  $\xi$  generated with EPOS (SD and SD+SD') and  
150 PYTHIA 8 SD (SaS, MBR and MBR-tuned). PYTHIA 8 (MBR) predicts a strong dependence of  
151 the cross section on  $\xi$ , which is much weaker in PYTHIA 8 (SaS and MBR-tuned) and the weakest  
152 in EPOS. This difference between PYTHIA 8 SaS and MBR models is expected since they are  
153 based on different Pomeron trajectories ( $\epsilon_{\text{SaS}} = 0, \epsilon_{\text{MBR}} = 0.104$ ). Only 30% of events in EPOS  
154 are SD, while the rest are SD'. Since all MC samples were generated with forward proton filter  
155 (a cut on the proton position in front of the RPs), the shapes of  $|t|$  distributions for these samples  
156 are biased. In order to compare them with each other, only their ratio to PYTHIA 8 (MBR)  
157 predictions is presented as a function of  $|t|$ . EPOS SD is only relevant for very small  $|t|$  (below  
158 0.04  $\text{GeV}^2/c^2$ ) and is suppressed in the STAR acceptance region,  $0.04 < |t| < 0.16$ , where EPOS  
159 SD' contribution dominates. The  $t$ -slope is very different for EPOS SD and EPOS SD', while it  
160 is similar for EPOS SD+SD' and PYTHIA 8 (SaS and MBR-tuned), EPOS SD and PYTHIA 8  
(MBR). This is related to the smaller average value of  $\xi$  for EPOS SD and PYTHIA 8 (MBR)  
compared to EPOS SD+SD' and PYTHIA 8 (SaS and MBR-tuned).

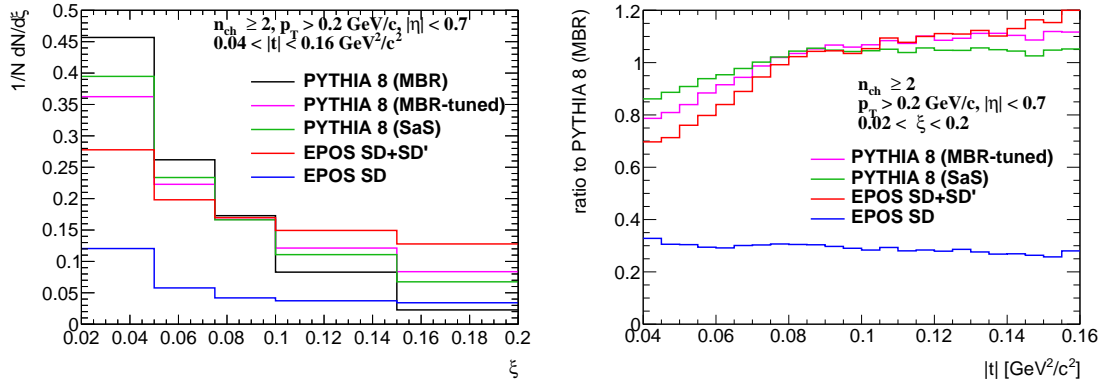


Figure 2.1: (left)  $\xi$  distribution for various MC generators and (right) ratios of different MCs to PYTHIA 8 (MBR) predictions as a function of  $|t|$  at  $\sqrt{s} = 200 \text{ GeV}$ .

161

# 3. Data Sample and Event Selection

The data sample used in this analysis was collected in proton-proton collisions at centre-of-mass energy of  $\sqrt{s} = 200$  GeV during RHIC Run 15.

All of the studies in this analysis use data from only the SDT trigger condition, which was the main trigger designed for SD studies in Run 15. The logic of the trigger was formed by the following conditions combined with the logical AND:

1. RP\_EOR || RP\_WOR - signal in at least one RP on any side of the STAR central detector,
2. veto on any signal in small BBC tiles or ZDC on the triggered RP side of the STAR central detector,
3. at least two TOF hits.

The above requirements were imposed in accordance with the diffractive event topology. Veto on any signal in small BBC tiles and ZDC allowed to accept only events with rapidity gap and reject diffractive events with simultaneous pile-up event. The requirement of at least two TOF hits was applied to ensure activity in the mid-rapidity.

Integrated luminosity delivered by the RHIC to the STAR experiment in  $pp$  collisions during Run 15 amounts to  $185.1 \text{ pb}^{-1}$  [9], whereas about 34.4M SDT events were gathered by the STAR detector, shown in Fig. 3.1, which corresponds to  $16 \text{ nb}^{-1}$  of integrated luminosity.

## Event Selection

Events were selected from those passing the SDT trigger condition. In order to remove events of poor quality and to suppress background the following conditions were required:

1. trigger signals in exactly two stations of one arm of RP system (this requirement divides the sample into four sub-samples, which were later analysed independently, e.g. for background studies),
2. any trigger signal in small BBC tiles on the opposite side of the STAR central detector to the triggered RP station,

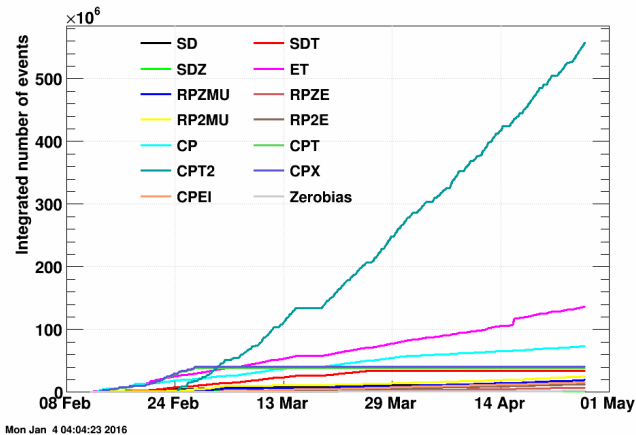


Figure 3.1: Cumulative number of events collected for each trigger in the RP data stream during Run 15 [7, 8].

- 188     3. exactly one proton track in the above RP stations with  $0.02 < \xi < 0.2$  and  $0.04 < -t <$   
 189      $0.16 \text{ GeV}^2/c^2$ .
- 190     4. exactly one vertex reconstructed from TPC tracks matched with hits in TOF (later in the text  
 191       such vertex is referred as a TOF vertex),
- 192     5. TOF vertex within  $|V_z| < 80 \text{ cm}$  - events with vertices away from the nominal IP have low  
 193       acceptance for the central and forward tracks,
- 194     6. at least two but no more than eight primary TPC tracks,  $2 \leq n_{\text{sel}} \leq 8$ , matched with hits  
 195       in TOF and satisfying the selection criteria described in Sec. 3.1,
- 196     7. if there are exactly two primary tracks satisfying the above criteria and exactly two global  
 197       tracks used in vertex reconstruction (Sec. 5.1), the longitudinal distance between these global  
 198       tracks should be smaller than 2 cm,  $|\Delta z_0| < 2 \text{ cm}$ .

199     Figure 3.2 shows the multiplicity of TOF vertices  $n_{\text{vrt}}$  (left) and the  $z$ -position of reconstructed  
 200       vertices in single TOF vertex events (right). Data are compared to embedded PYTHIA 8 SD  
 201       sample. These distributions are not significantly process-dependent, therefore, contributions from  
 202       other processes are not included in these plots. Most events with  $n_{\text{vrt}} > 1$  originate from in-time  
 203       pile-up and are excluded from the analysis.

#### 204     **ZDC Veto**

205     The SDT trigger conditions imposed a veto on any signal in the same-side ZDC. However, all MC  
 206       samples do not contain ZDC simulation. To check the impact of this veto on the measurement,  
 207       the total energy of neutral particles, such as  $n$ ,  $\gamma$ ,  $\pi^0$ , produced within ZDC acceptance ( $|\eta| > 6$ )  
 208       was measured using true-level PYTHIA 8 (SaS). In most of the events, the energy measured on  
 209       the proton side of the IP is smaller than trigger thresholds (as shown in Fig. 3.3). Therefore,  
 210       the ZDC veto has a negligible effect on the analysis and ZDC simulation is not needed.

### 211     **3.1 Track Selection**

212     The following quality cuts had to be passed by the selected primary tracks:

- 213     1. the tracks must be matched with hits reconstructed in TOF,  
 214     2. the number of the TPC hits used in the helix fit  $N_{\text{hits}}^{\text{fit}}$  must be greater than 24,

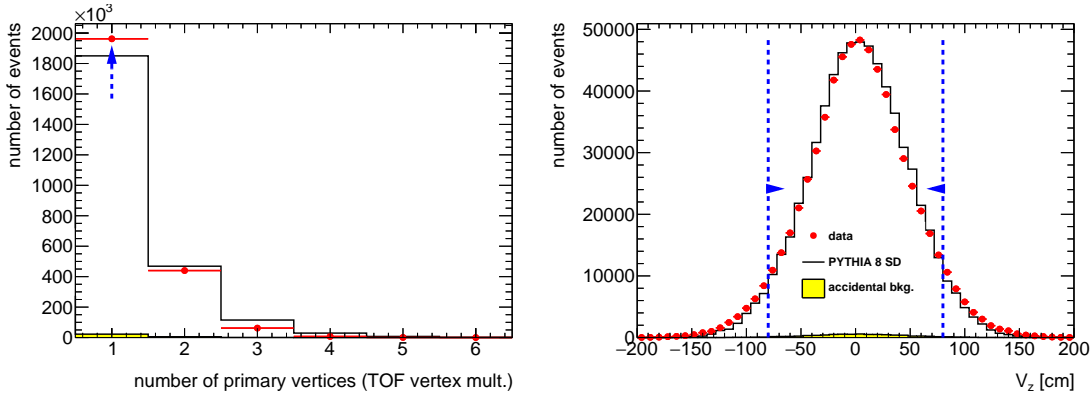


Figure 3.2: (left) Vertex multiplicity and (right) the  $z$ -position of reconstructed vertices in single TOF vertex events before applying the cut on the quantity shown. Blue lines indicate regions accepted in the analysis.

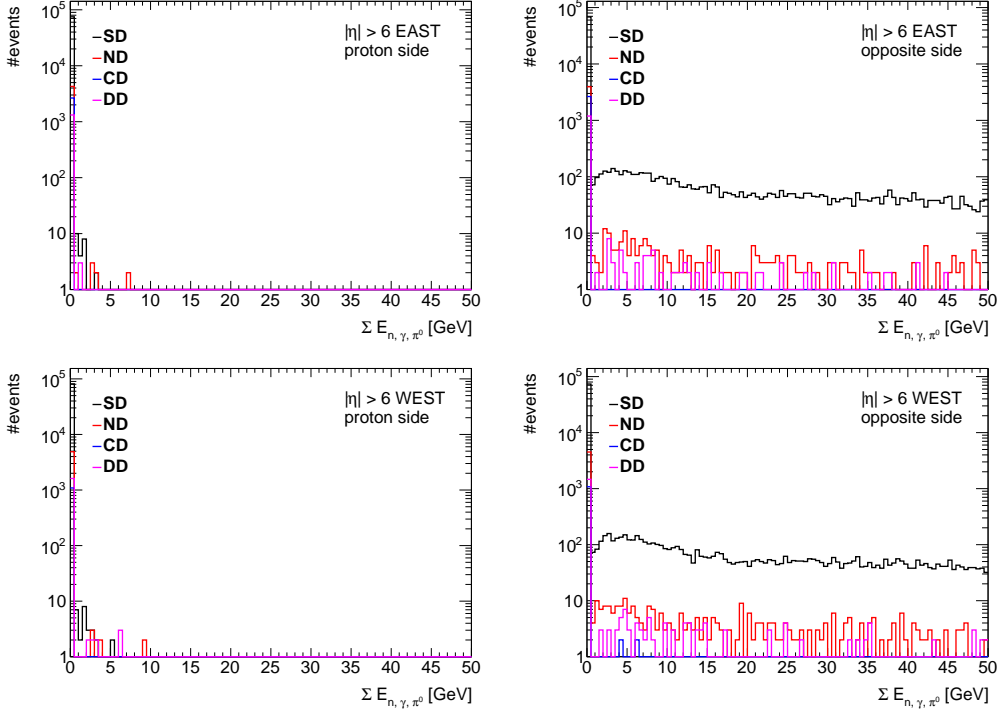


Figure 3.3: Total energy of neutral particles ( $n, \gamma, \pi^0$ ) produced within ZDC acceptance ( $|\eta| > 6$ ) for events in which forward-scattered proton is on (top) west and (bottom) east side of the IP. Distributions are presented separately for neutral particles produced on (left) the proton and (right) opposite side of the IP. PYTHIA 8 predictions for different processes are shown as colour histograms.

- 215     3. the number of the TPC hits used to determine the  $dE/dx$  information  $N_{\text{hits}}^{\text{dE/dx}}$  must be  
216     greater than 14,
- 217     4. the transverse impact parameter with respect to the beamline  $d_0$  must be less than 1.5 cm,
- 218     5. the radial component of the distance of the closest approach between the global helix and  
219     the vertex  $\text{DCA}_{xy}$  must be less than 1.5 cm,
- 220     6. the absolute magnitude of longitudinal component of the distance of the closest approach  
221     between the global helix and the vertex  $|\text{DCA}_z|$  must be less than 1 cm,
- 222     7. the track's transverse momentum  $p_T$  must be greater than 0.2 GeV/c,
- 223     8. the track's absolute value of pseudorapidity  $|\eta|$  must be smaller than 0.7.

224     The  $N_{\text{hits}}^{\text{fit}}$  and  $N_{\text{hits}}^{\text{fit}}/N_{\text{hits}}^{\text{possible}}$  cuts are used to reject low quality TPC tracks and avoid track  
225     splitting effects. The  $d_0$  and global  $\text{DCA}_{xy}$ ,  $|\text{DCA}_z|$  cuts are used to select tracks that originate  
226     from the primary interaction vertex. The cut on  $N_{\text{hits}}^{\text{dE/dx}}$  is used to ensure that selected tracks  
227     have sufficient energy loss information for particle identification purposes. In this analysis tracks  
228     without identification are required to have  $p_T > 0.2$  GeV/c and  $|\eta| < 0.7$  due to high track  
229     reconstruction and TOF matching efficiencies in this region. For the identified particle-antiparticle  
230     ratio analysis, where charged pions, charged kaons and (anti)protons are measured, the  $p_T$  cut  
231     was increased for kaons and (anti)protons to 0.3 and 0.4 GeV/c, respectively. The distributions  
232     of the  $\text{DCA}_{xy}$ ,  $|\text{DCA}_z|$ ,  $d_0$ ,  $N_{\text{hits}}^{\text{fit}}$  and  $N_{\text{hits}}^{\text{dE/dx}}$  quantities together with applied cuts are shown in

233 Fig. 3.4, while the  $p_T$ ,  $\eta$  and the azimuthal angle,  $\phi$ , of the reconstructed tracks are shown in  
 234 Fig. 3.5. Data are compared to embedded PYTHIA 8 SD sample.

235 The azimuthal angle of the reconstructed tracks for runs  $\leq 16073050$  is not described by PY-  
 236 THIA 8. The inner sector #19 in the TPC was dead for this running period and some effects  
 237 related to it were presumably not taken into account in the TPC detector simulation. There-  
 238 fore, additional data-driven corrections to track efficiencies are used [1]. The larger accidental  
 239 background is observed for runs  $> 16073050$ , probably due to the higher bunch intensities in this  
 240 running period [10].

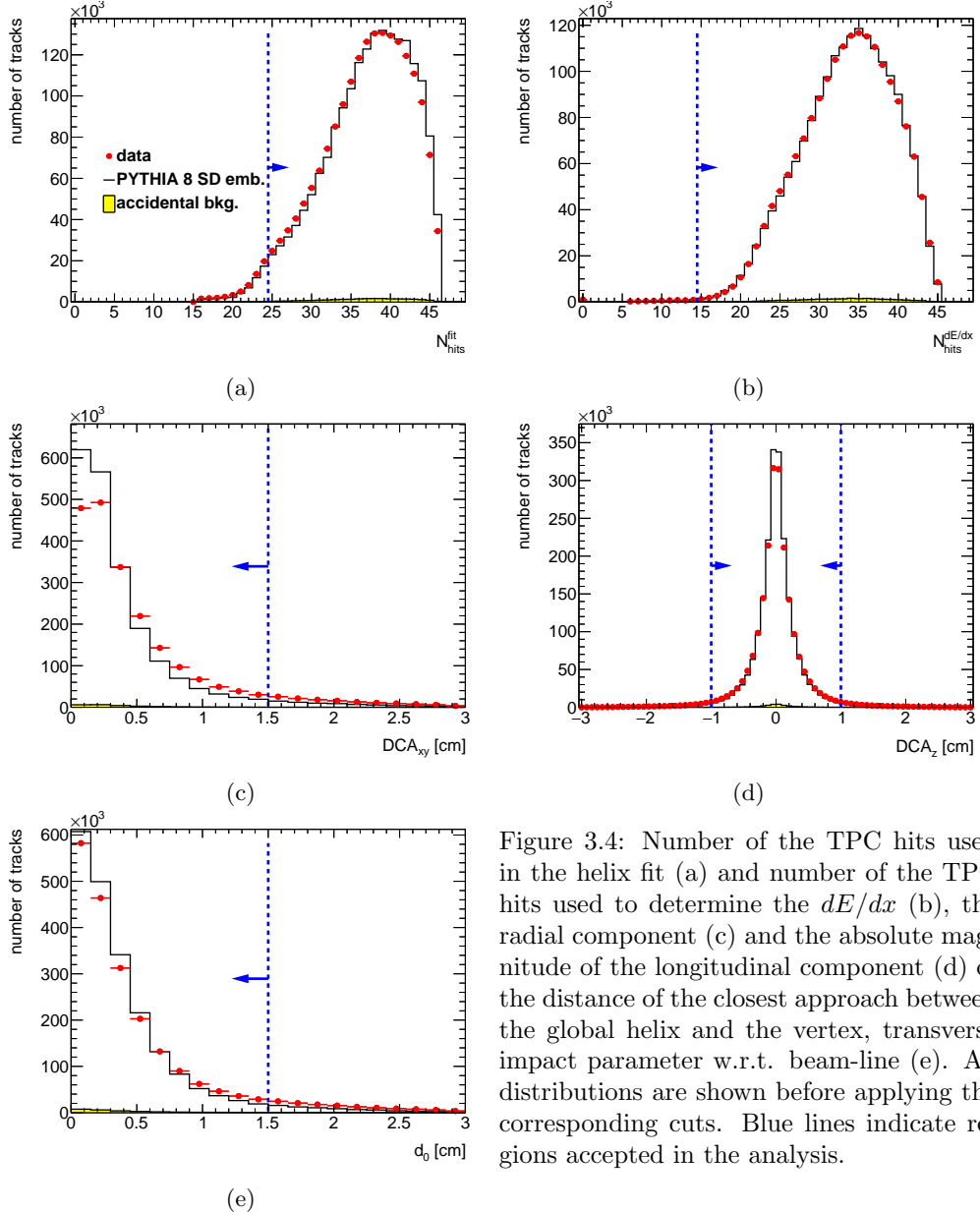


Figure 3.4: Number of the TPC hits used in the helix fit (a) and number of the TPC hits used to determine the  $dE/dx$  (b), the radial component (c) and the absolute magnitude of the longitudinal component (d) of the distance of the closest approach between the global helix and the vertex, transverse impact parameter w.r.t. beam-line (e). All distributions are shown before applying the corresponding cuts. Blue lines indicate regions accepted in the analysis.

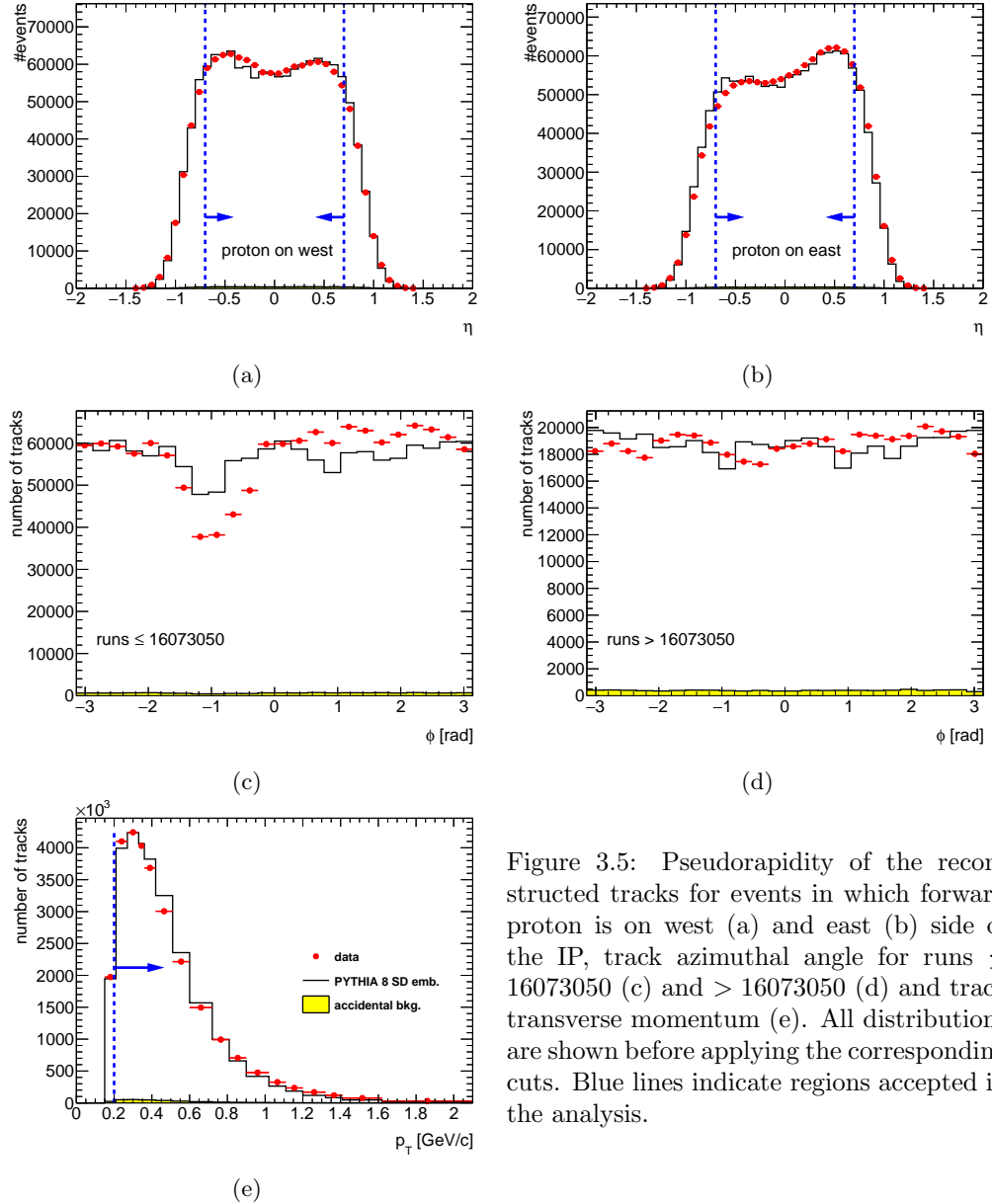


Figure 3.5: Pseudorapidity of the reconstructed tracks for events in which forward proton is on west (a) and east (b) side of the IP, track azimuthal angle for runs  $\leq 16073050$  (c) and  $> 16073050$  (d) and track transverse momentum (e). All distributions are shown before applying the corresponding cuts. Blue lines indicate regions accepted in the analysis.

## 241 3.2 Fiducial Region of the Measurement

242 A fiducial phase space of measurement is defined by the following criteria. Primary charged  
 243 particles are defined as charged particles with a mean lifetime  $\tau > 300$  ps, either directly produced  
 244 in  $pp$  interaction or from subsequent decays of directly produced particles with  $\tau < 30$  ps. Primary  
 245 charged particles had to be contained within the kinematic range of  $p_T > 0.2$  GeV/c and  $|\eta| < 0.7$ .  
 246 The results are corrected to the region of the total number of primary charged particles (without  
 247 identification),  $2 \leq n_{ch} \leq 8$ . In identified charged antiparticle to particle ratio measurement, the  
 248 lower transverse momentum limit was set for the analysed particles as follows: 0.2 GeV/c (pions),  
 249 0.3 GeV/c (kaons), 0.4 GeV/c (protons and antiprotons).

250 The measurements were performed in a fiducial phase space of the forward-scattered protons  
 251 of  $0.04 < -t < 0.16$  GeV $^2/c^2$  and  $0.02 < \xi < 0.2$ . Figure 3.6 shows that the fraction of events  
 252 containing at least two primary charged particles,  $\epsilon_{n_{ch}\geq 2}(\log_{10} \xi)$ , is reduced by half for  $\xi < 0.02$   
 253 compared to the region of larger  $\xi$ . In addition, the accidental background contribution at  $\xi < 0.02$   
 254 is significant and approximately equal to 10% (Sec. 4). For these reasons the lower  $\xi$  cut was  
 255 introduced. The upper  $\xi$  cut was required since the region of larger  $\xi$  is dominated by Double

256 Diffraction (DD) and ND (Sec. 4.2). The joint RP acceptance and track reconstruction efficiency  
 257 was defined as the probability that true-level proton was reconstructed as a track passing the  
 258 selection criteria. This efficiency was calculated as a function of  $-t$  for three ranges of  $\xi$  separately  
 259 and is shown in Fig. 3.7. Events were accepted only if the reconstructed values of  $-t$  for protons  
 260 fall within  $> 5\%$  acceptance regions, which were required to be the same for each  $\xi$  region and  
 261 similar to those defined in the elastic analysis [11]. Therefore, cuts on  $0.04 < -t < 0.16 \text{ GeV}^2/c^2$   
 262 were introduced. All measured observables are presented in three  $\xi$  regions:  $0.02 < \xi < 0.05$ ,  
 263  $0.05 < \xi < 0.1$  and  $0.1 < \xi < 0.2$ .

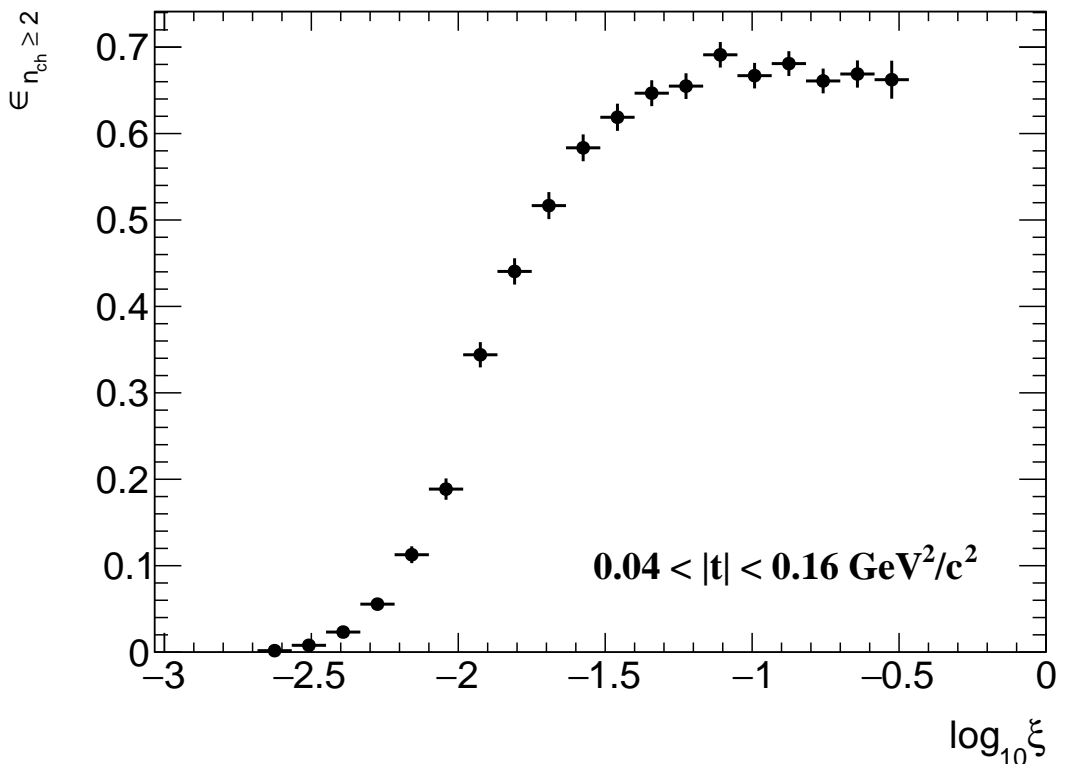


Figure 3.6:  $\epsilon_{n_{ch} \geq 2}$  as a function of  $\log_{10} \xi$  calculated from PYTHIA 8 (MBR).

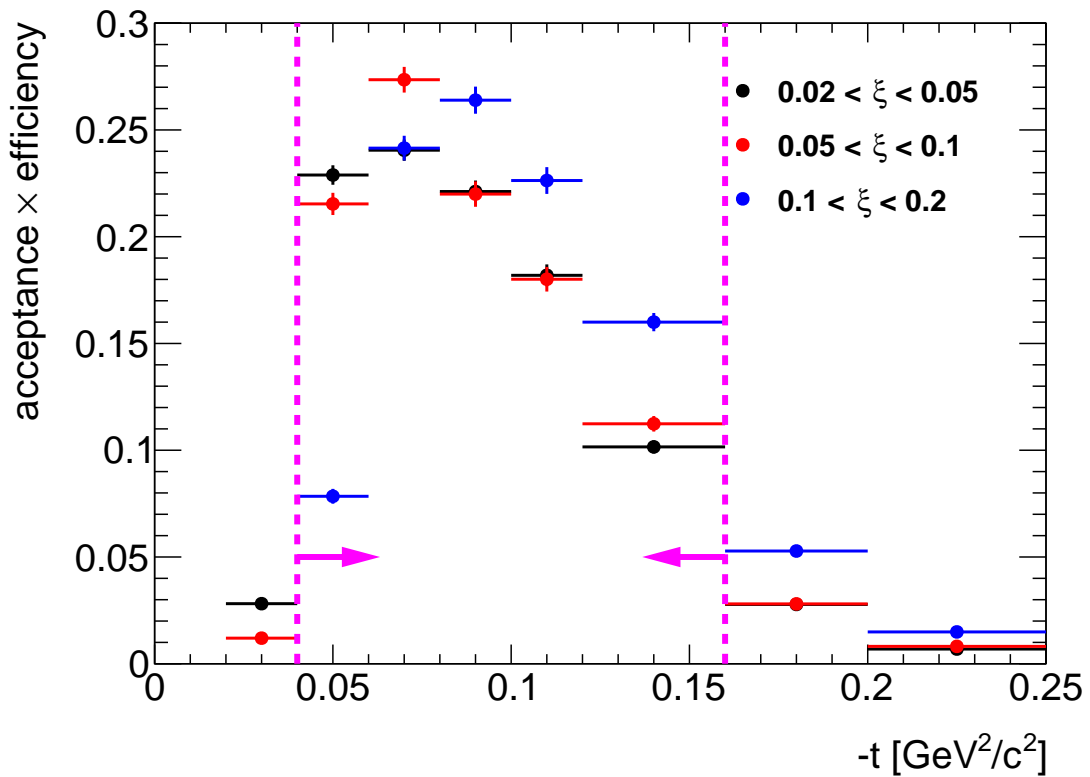


Figure 3.7: RP acceptance and track reconstruction efficiency as a function  $-t$  in three ranges of  $\xi$ , calculated using PYTHIA 8 4C (SaS). Magenta lines indicate region accepted in the analysis.

# 4. Background Contribution

The background contributions to the charged-particle distributions can be divided into event-level and track-level backgrounds, and are described in detail below:

- Accidental background refers to events which do not originate from a single collision of two protons.
- Track backgrounds from non-primary tracks consist of secondary tracks and fake tracks; the first come mostly from decays, the short-lived particles with mean life  $30 < \tau < 300$  ps, or secondary interactions with the detector dead material, while the second comes from the track reconstruction algorithms and out-of-time pile-up with no corresponding true particles.

## Accidental Background

The accidental backgrounds (same bunch pile-up background) are quantified using data-driven method and defined as a process where in single bunch crossing there is coincidence of two interactions, where any single-side proton signal is collected in coincidence with an independent signal in the TPC+TOF+BBC detector. This type of background may come from the overlap of a signal in RP (proton from beam-halo, low mass SD process without activity in TOF, elastic or low mass Central Diffraction (CD) processes with undetected proton on the other side) with a signal in TPC+TOF+BBC (mainly ND events without forward-scattered proton).

The accidental background contribution was calculated from Zerobias data (colliding bunches), where two signatures of such background were investigated: the reconstructed proton in RP and the reconstructed vertex from TPC tracks matched with TOF. The analysis was done for each RP arm separately and thus the Zerobias data was firstly required to pass the following criteria:

1. no trigger in any RP or trigger in exactly one arm (two RPs) with exactly one reconstructed proton track in that arm,
2. veto on any signal in small BBC tiles or ZDC on the same side of the IP as the RP arm under consideration,
3. no or exactly one reconstructed vertex with at least two TOF-matched tracks passing the quality criteria. The latter includes also signal in BBC small tiles on the opposite side of the IP to the RP arm under study.

The sample of selected Zerobias data with total number of events  $N$  was divided into four classes:

$$N = N_{PS} + N_{RS} + N_{PT} + N_{RT} \quad (4.1)$$

where:  $N_{PS}$  is the number of events with reconstructed proton in exactly one RP and reconstructed TOF vertex,  $N_{RS}$  is the number of events with no trigger in any RP and reconstructed TOF vertex,  $N_{PT}$  is the number of events with reconstructed proton in exactly one RP and no reconstructed TOF vertex,  $N_{RT}$  is the number of events with no trigger in any RP and no reconstructed TOF vertex. Since the signature of the signal is a reconstructed proton in exactly one RP and a reconstructed TOF vertex, the number of such events can be expressed as:

$$N_{PS} = N(p_3 + p_1 p_2) \quad (4.2)$$

where:  $p_1$  is the probability that there is a reconstructed proton in RP and there is no reconstructed TOF vertex,  $p_2$  is the probability that there is no reconstructed proton in RP and there is a reconstructed TOF vertex,  $p_3$  is the probability that there is a reconstructed proton in RP and there is a reconstructed TOF vertex (not accidental).

304        The other classes of events given in Eq. (4.1) can be expressed in terms of the above probabilities  
 305        as:

$$\begin{aligned} N_{RS} &= N(1 - p_1)p_2(1 - p_3) \\ N_{PT} &= N(1 - p_2)p_1(1 - p_3) \\ N_{RT} &= N(1 - p_1)(1 - p_2)(1 - p_3) \end{aligned} \quad (4.3)$$

306        Finally, the accidental background contribution  $A_{\text{bkg}}^{\text{accidental}}$  is given by:

$$A_{\text{bkg}}^{\text{accidental}} = \frac{p_1 p_2}{p_3 + p_1 p_2} = \frac{N_{RS} N_{PT} N}{N_R N_T N_{PS}} \quad (4.4)$$

307        where:  $N_R = N_{RS} + N_{RT}$  and  $N_T = N_{PT} + N_{RT}$ .

308        The shapes of the accidental background related to TPC distributions come from the above  
 309        Zerobias data events which pass all the analysis selection except having no trigger in any RP.  
 310        The templates corresponding to RP distributions are from protons in the above data sets but  
 311        with no reconstructed TOF vertex. The normalization is given by Eq. (4.4). Figure 4.1 shows  
 312        distributions of the reconstructed  $\xi$  with the accidental background contribution for events with  
 313        proton reconstructed in EU, ED, WU and WD arms. Accidental background in the range of  
 314         $0.02 < \xi < 0.2$  is below 1% and increases to 10% at  $\xi < 0.02$ . Unphysical negative values of  
 315        reconstructed  $\xi$  are due to the detector resolution.

316        The selection of Zerobias events, which is not unique, may provide some bias to the normalization  
 317        of the accidental background. As a systematic check, two criteria for Zerobias selection were  
 318        changed to:

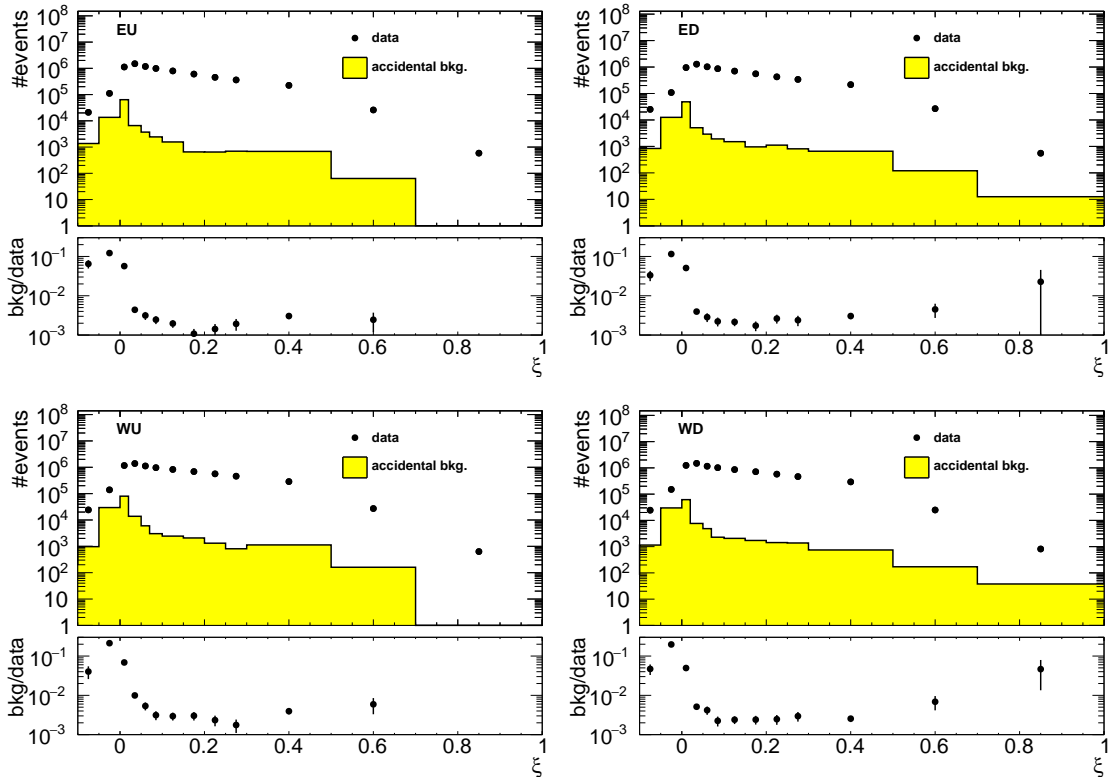


Figure 4.1: Uncorrected distributions of the reconstructed  $\xi$  for events with proton reconstructed in (top left) EU, (top right) ED, (bottom left) WU and (bottom right) WD arms. Data is shown as black markers, whereas the accidental background contribution is shown as yellow histogram. The ratio of accidental background and data is shown in the bottom panels.

- 319     1. no trigger in any RP or trigger in exactly one arm (two RPs) with *no more* than one  
 320       reconstructed proton track in that arm, i.e. events with trigger signals in exactly one arm  
 321       and without reconstructed proton track in that arm were also used,  
 322     2. no or exactly one reconstructed TOF vertex (*without any additional requirements*), i.e.  
 323       events with a reconstructed TOF vertex that does not have at least two primary tracks  
 324       satisfying the selection criteria (Sec. 3.1), or with a reconstructed TOF vertex that is out of  
 325       the range of  $|V_z| < 80$  cm, were also accepted. The requirement of signal in BBC small tiles  
 326       remains unchanged.

327     As a result of this change, the accidental background normalization increases of about 50% with  
 328     respect to the nominal value. A symmetric systematic uncertainty of 50% of the normalization of  
 329     accidental background is applied to the measurement.

## 330     4.1 Background from Non-Primary Tracks

331     Reconstructed tracks matched to a non-primary particle, so-called background tracks, originate  
 332     mainly from the following sources:

- 333       • decays of short-lived primary particles with strange quark content (mostly  $K^0, \Lambda^0$ ),  
 334       • photons from  $\pi^0$  and  $\eta$  decays which are converting to  $e^+e^-$ ,  
 335       • hadronic interactions of particles with the beam-pipe or detector dead material.

336     Figure 4.2 (left) shows the background from non-primary tracks,  $f_{\text{bkg}}(p_T, \eta)$ , as a function  
 337     of tracks'  $p_T$  and  $\eta$ , predicted by PYTHIA 8 SD model. There were no differences observed in  
 338     the background contribution in different  $\xi$  ranges, hence, all three  $\xi$  ranges were merged for this  
 339     study. The highest background fraction, which varies between 5 – 10%, was found to be at low  
 340      $p_T$ .

341     Figure 4.2 (right) shows the background track contribution to reconstructed tracks as a function  
 342     of  $p_T$  and  $\eta$  calculated from EPOS SD+SD'. The differences between PYTHIA 8 and EPOS,  
 343     which are up to 50% for  $p_T > 0.5$  GeV/c (as shown in Fig. 4.3), were symmetrized and taken as  
 344     a systematic uncertainty.

345     There is also a small (< 0.5%) contribution from fake tracks,  $f_{\text{fake}}(p_T, \eta)$ , i.e. tracks not associated  
 346     with true-level particles, coming from out-of-time pile-up or formed by a random combination  
 347     of TPC hits. The change by  $\pm 100\%$  in this contribution was taken as a systematic uncertainty.

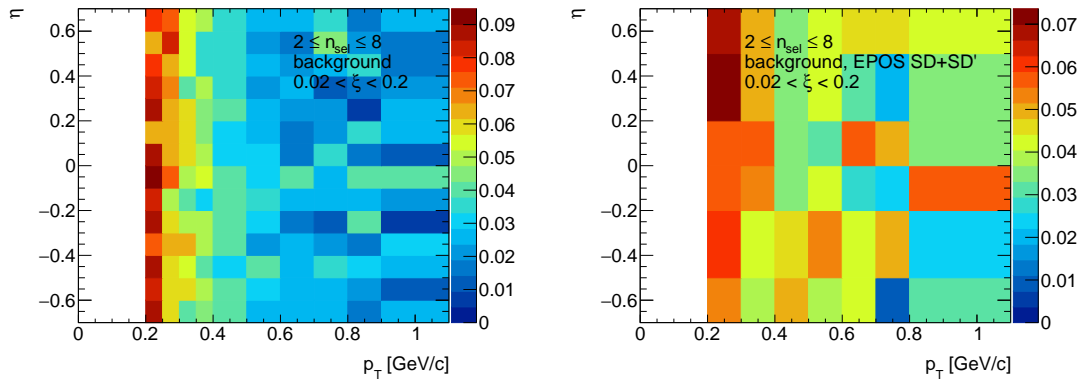


Figure 4.2: Distribution of fraction of selected tracks associated with non-primary particles in the range  $0.02 < \xi < 0.2$  as predicted by (left) PYTHIA 8 4C (SaS) embedding and (right) EPOS SD+SD'.

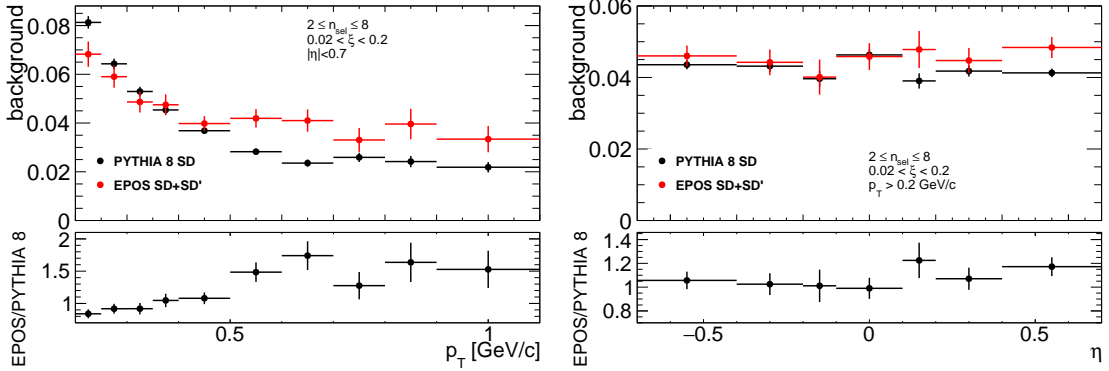


Figure 4.3: PYTHIA 8 SD and EPOS SD+SD' predictions of fraction of selected tracks associated with non-primary particles as a function of (left)  $p_T$  and (right)  $\eta$ . The ratio of EPOS and PYTHIA 8 predictions is shown in the bottom panels.

### 348 Proton Background

349 Secondary particles can be created due to the interaction of particles with detector dead-material.  
 350 The proton sample contains background from such protons knocked out from the detector materials [12].  
 351 Most of these protons have large DCA to the primary vertex and are not associated with  
 352 it. However, the protons with small DCA are included in the primary track sample. Antiprotons  
 353 do not have knockout background, hence the DCA tail is almost absent in their DCA distributions.

354 The fraction of knock-out background protons depends on a number of factors, including  
 355 the amount of detector material, analysis cuts and the  $\xi$  of diffractive proton. While it is natural  
 356 to calculate the fractions of primary and background protons in the MC sample, the MC models  
 357 do not necessarily predict the fraction of knock-out background protons without any bias. Hence,  
 358 data-driven methods should be used to calculate this type of background.

359 In order to correct for the knock-out background protons, sample enriched in proton back-  
 360 ground was used for background normalization, where  $\text{DCA}_{xy}$ ,  $\text{DCA}_z$  and  $d_0$  cuts were aban-  
 361 doned. Additionally, at least one, instead of exactly one, reconstructed vertex was allowed in this  
 362 sample. Figures 4.4 and 4.5 show the DCA distributions of protons and antiprotons, respectively,  
 363 for nominal (bottom) and background enriched (top) samples. The distributions for other  $p_T$   
 364 and  $\xi$  regions are shown in Appendix A. The protons and antiprotons are selected by a  $dE/dx$   
 365 cut of  $-1 < n\sigma_{p,\bar{p}} < 3$  where  $n\sigma_{p,\bar{p}}$  is given by Eq. (7.10). In some  $p_T$  regions, the  $dE/dx$  of  
 366 (anti)protons and pions starts to overlap, hence, the asymmetric  $n\sigma_{p,\bar{p}}$  cut was introduced in or-  
 367 der to select as clean (anti)proton sample as possible. The fraction of knock-out protons within  
 368 the selected sample is determined via MC template fits. The templates of reconstructed tracks  
 369 with  $dE/dx$  corresponding to the proton and antiproton are obtained from PYTHIA 8 embedding  
 370 MC separately for:

- 371     • primary (anti)protons,
- 372     • knock-out background protons (labeled as dead-material),
- 373     • fake tracks,
- 374     • secondary particles with  $dE/dx$  of (anti)proton (labeled as wrong PID - sec.),
- 375     • tracks associated with primary (anti)protons, but with the reconstructed vertex not matched  
       376        to true-level primary vertex (labeled as wrong vtx),
- 377     • reconstructed track is partially matched to true-level particle (labeled as wrong match, track  
       378        to true-level particle matching is described in [1]), i.e. track and true-level particle have  
       379        appropriate number of common hit points but the distance between true-level particle and

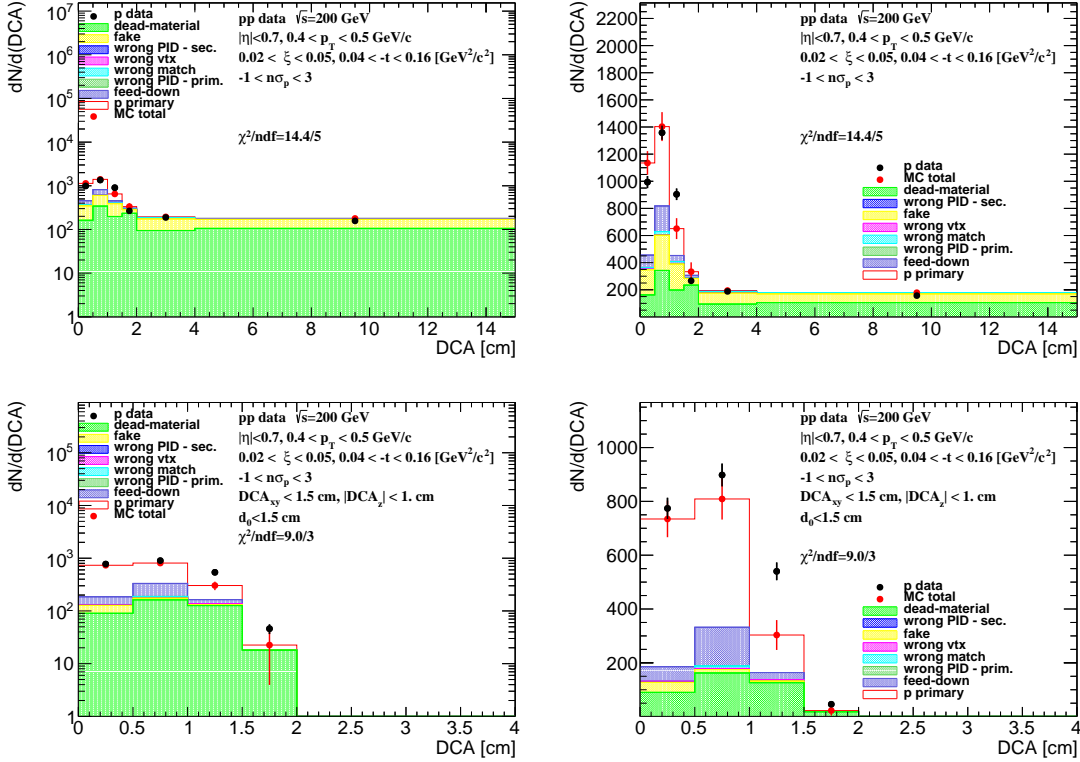


Figure 4.4: The DCA distributions of protons for  $0.4 < p_T < 0.5 \text{ GeV}/c$  shown for single range of  $0.02 < \xi < 0.05$  (shown in log and linear scale in left and right column, respectively). The MC contributions are shown after scaling the dead-material template to the tail of large DCA values,  $2 < \text{DCA} < 15 \text{ cm}$ . (top) Background enriched samples were used in the normalization procedure, whereas (bottom) the proton background was estimated from the nominal sample.

380 track is too large,  $\delta^2(\eta, \phi) > (0.15)^2$ , thus, track is not considered as primary particle  
381 according to discussion in [1],

- 382 • primary particles with  $dE/dx$  of (anti)proton (labeled as wrong PID - prim.),  
383 • (anti)proton as a product of short-lived decays, mainly  $\Lambda^0$  (labeled as feed-down).

384 First, the background enriched sample was analyzed (Fig. 4.4, top), where the template of  
385 knock-out background protons was normalized to the number of events in the fake-subtracted tail  
386 of the DCA distribution,  $2 < \text{DCA} < 15 \text{ cm}$ . Next the knock-out proton and fake background  
387 was subtracted from the DCA distribution and the sum of other templates was normalized to  
388 the number of events in the signal region,  $\text{DCA} < 1.5 \text{ cm}$ .

389 The fraction of the knock-out proton background in the signal region,  $\text{DCA} < 1.5$ , was es-  
390 timated from the nominal sample (Fig. 4.4, bottom), where  $\text{DCA}_{xy}$ ,  $\text{DCA}_z$  and  $d_0$  track cuts  
391 were applied and exactly one reconstructed vertex was required. The normalization of each MC  
392 contribution was kept the same as that estimated for the background enriched sample. Figure 4.6  
393 shows the knock-out proton background as a function of  $p_T$  in three ranges of  $\xi$ . The following  
394 functional form was found to describe the background protons:

$$f_{\text{bkg}}^p(p_T) = p_0 \exp(p_1 p_T) \quad (4.5)$$

395 where  $p_0$  and  $p_1$  are free parameters obtained from a fit.

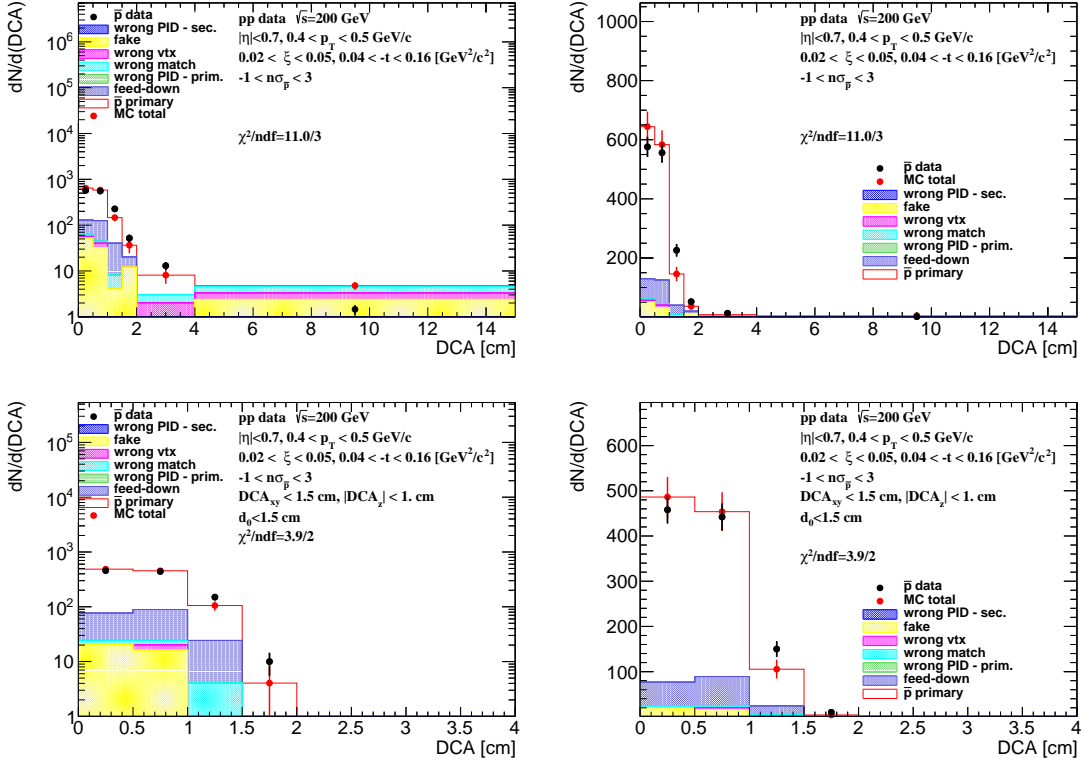


Figure 4.5: The DCA distributions of antiprotons for  $0.4 < p_T < 0.5 \text{ GeV}/c$  shown for one range of  $0.02 < \xi < 0.05$  (log and linear scale in left and right column, respectively). The MC contributions are shown as colour histograms. (top) Background enriched and (bottom) nominal samples were used.

396     The obtained fraction of knock-out background protons is approximately 20% at  $p_T = 0.45$   
397     GeV/c and less than 10% at  $p_T = 1.0 \text{ GeV}/c$ . In PYTHIA 8 SD predictions (also shown in Fig. 4.6),  
398     such fraction is much smaller and equals to approximately 7% at  $p_T = 0.45 \text{ GeV}/c$  and about 5%  
399     at  $p_T = 1.0 \text{ GeV}/c$ . This may suggest that there are differences in the amount of dead material in  
400     front of TPC between data and simulation, which is consistent with the studies presented in [1].

401     Figure 4.5 shows the corresponding DCA distributions with MC templates for antiprotons,  
402     where the background from knock-out particles is not present. Therefore, there was no need for  
403     any fit to be performed in this comparison. The MC templates fairly well describe the DCA  
404     distribution for both, protons, after tuning the fraction of knock-out background to data, and  
405     antiprotons.

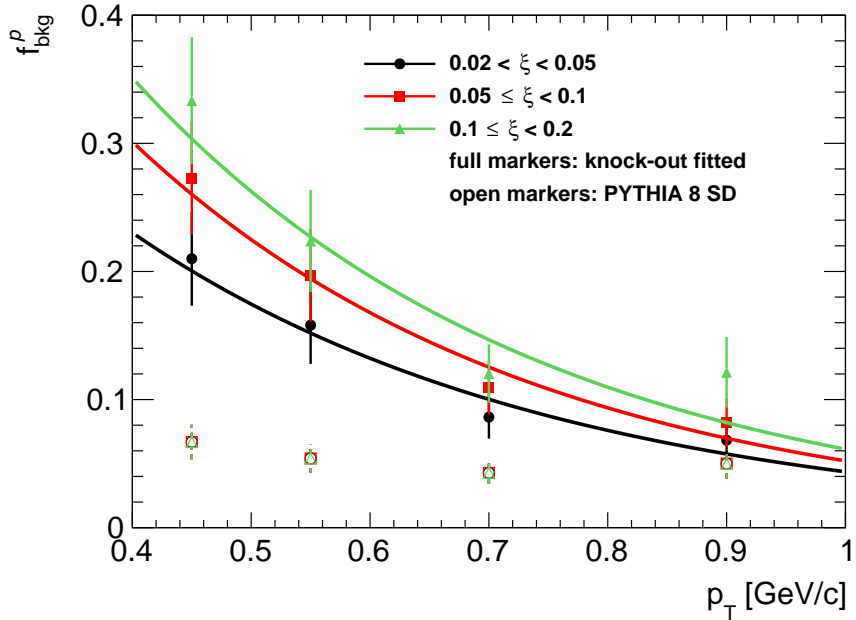


Figure 4.6: The fraction of knock-out proton background as a function of  $p_T$  in three ranges of  $\xi$  with fitted parametrizations. Full markers represent fitted knock-out background and open markers represent PYTHIA 8 SD predictions.

#### 406 Systematic Uncertainty Related to Proton Background

407 The knock-out proton background estimation introduces systematic uncertainties. First, the nor-  
 408 malization interval of the knock-out proton background template in the background enriched  
 409 sample was changed to  $4 < \text{DCA} < 15$  cm. This introduced a relative systematic uncertainty of  
 410 up to 30% for  $p_T \approx 0.9$  GeV/c.

411 The knock-out proton background contribution was parameterized as it is shown in Eq. (4.5).  
 412 The systematic uncertainty related to the parameterization procedure was estimated by varying the  
 413 parameters,  $p_0$  and  $p_1$ , by their statistical uncertainties ( $\pm 1\sigma$ ). As a result, a relative systematic  
 414 uncertainties of about 10% were obtained.

415 Differences in the shape of the DCA distribution between data and MC can affect the knock-  
 416 out proton background estimation procedure. Figure 4.7 (top left) shows the data to MC ratio of  
 417 the number of events in the background dominated region,  $2 < \text{DCA} < 15$  cm. Since this region  
 418 is used to estimate background normalization, and the shape of the DCA distribution in the data  
 419 differs from that observed in the simulation, the predicted background in the  $\text{DCA} < 1.5$  cm region  
 420 can change. Thus, the following functional form was used to estimate the slope between data and  
 421 MC:

$$\frac{\text{data}}{\text{MC}}(\text{DCA}) = A(\text{DCA} - 8.5) + B \quad (4.6)$$

422 where  $A$  (slope) and  $B$  are fit free parameters. Differences in slope between data and MC were used  
 423 to estimate how many more background tracks would fit into the signal region and a systematic  
 424 uncertainty, which varies up to 5% for  $0.02 < \xi < 0.05$ , was introduced.

425 All above components of the systematic uncertainty related to the knock-out proton back-  
 426 ground, shown in Fig. 4.7, are added in quadrature. Those related to the fit range and the shape  
 427 of the proton background are symmetrized. Figure 4.8 shows the fraction of knock-out proton  
 428 background in three ranges of  $\xi$  and the total systematic uncertainty related to it.

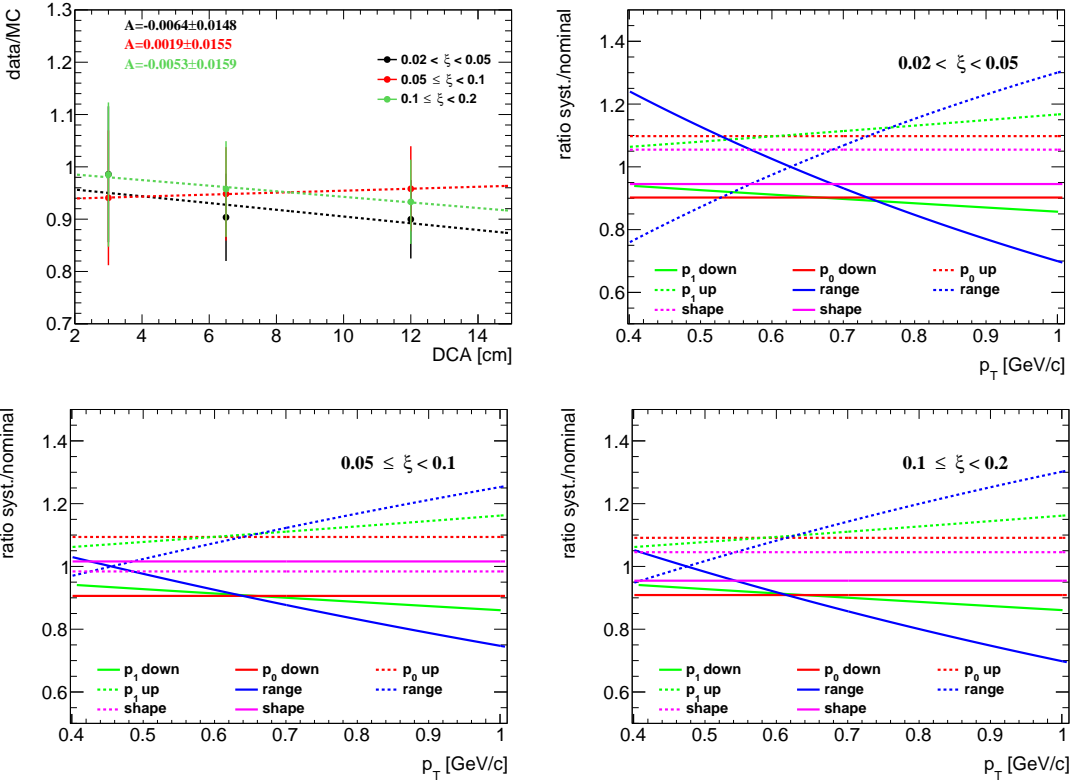


Figure 4.7: (top left) Data to MC ratio of the number of events in the background dominated region in three ranges of  $\xi$  with fitted functional form given by Eq. (4.6). (top right and bottom) Components of the systematic uncertainty related to the knock-out background protons contribution in three  $\xi$  ranges.

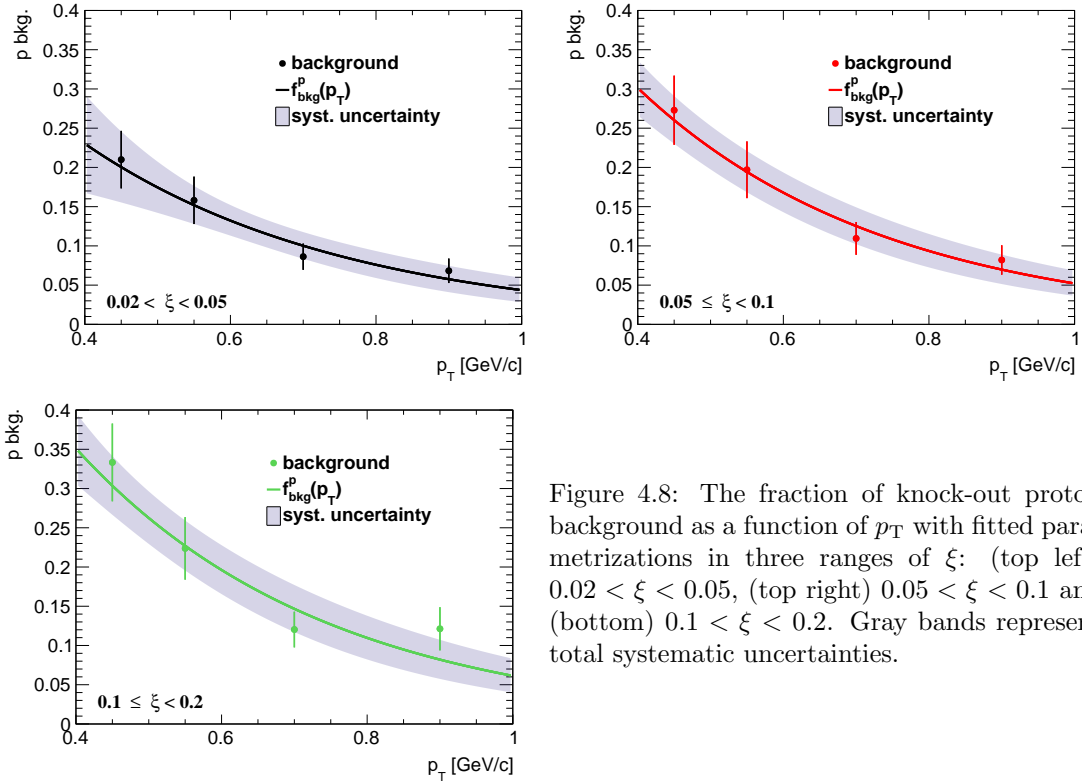


Figure 4.8: The fraction of knock-out proton background as a function of  $p_T$  with fitted parametrizations in three ranges of  $\xi$ : (top left)  $0.02 < \xi < 0.05$ , (top right)  $0.05 \leq \xi < 0.1$  and (bottom)  $0.1 \leq \xi < 0.2$ . Gray bands represent total systematic uncertainties.

429 **Pion Background**

430 The pion spectra are corrected for weak decays (mainly of  $K_S^0$  and  $\Lambda^0$ ), muon contribution and  
 431 background from the detector dead-material interactions. The pion decay muons can be identified  
 432 as pions due to the similar masses. These background contributions are obtained from PYTHIA 8  
 433 SD. Figure 4.9 shows the background contribution to the pion spectra as a function of  $p_T$  in  
 434 three ranges of  $\xi$ , separately for  $\pi^-$  and  $\pi^+$ . Since there were negligible differences observed  
 435 between these three ranges of  $\xi$ , the background contribution was averaged over  $\xi$ . The following  
 436 parametrization was found to describe it:

$$f_{\text{bkg}}^\pi(p_T) = a_0 \exp(a_1 p_T) + a_2 p_T^2 + a_3 p_T \quad (4.7)$$

437 where  $a_i$ ,  $i = 0, \dots, 3$  are free parameters of the fitted function.

438 The pion background contribution varies between 5% at low- $p_T$  ( $p_T = 0.25$  GeV/c) and about  
 439 1% at  $p_T = 1.0$  GeV/c for both negatively and positively charged pions. In addition, the back-  
 440 ground was calculated from EPOS SD+SD' for the full range of  $\xi$ . The differences between  
 441 PYTHIA 8 and EPOS are up to 1% for  $\pi^-$ .

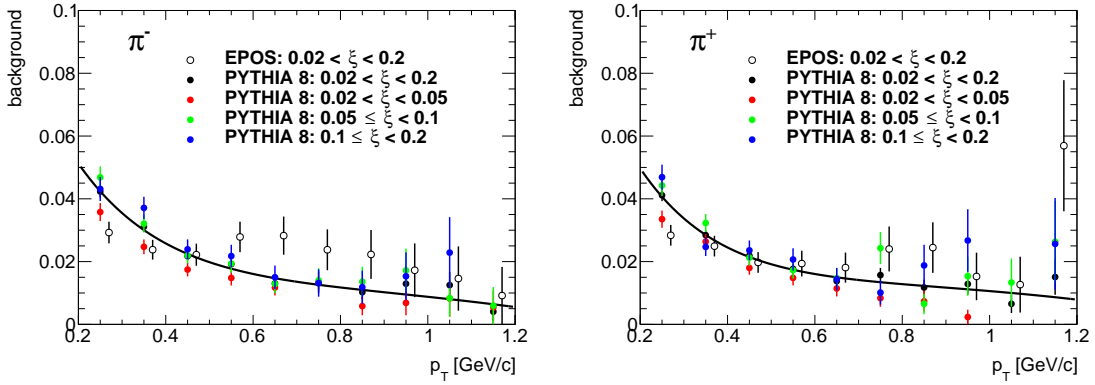


Figure 4.9: Pion background fraction as a function of  $p_T$  shown separately for (left) negatively and (right) positively charged pions in three ranges of  $\xi$ : (red)  $0.02 < \xi < 0.05$ , (green)  $0.05 < \xi < 0.1$ , (blue)  $0.1 < \xi < 0.2$ . (full black points) The pion background averaged over three ranges of  $\xi$  with fitted parametrization is also shown. Open black points represent EPOS predictions for the full  $\xi$  range.

## 4.2 Control Plots

Events, in which forward-scattered proton and reconstructed TOF vertex are the result of the same  $pp$  interaction, may originate from ND, DD, SD, and CD processes. It is preferred to estimate the background contribution from data, using dedicated control regions. Since such regions were not found, the relative contributions from the above processes were estimated from MC models and are therefore model dependent. Tracks reconstructed in RPs may also be:

- forward-scattered protons produced in the SD, CD or DD diffractive systems or from ND events,
- secondary particles from showering initiated by interaction of forward-scattered protons with beam-line elements. This contribution is negligible.

Figure 4.10 shows the uncorrected  $\xi$  and  $t$  distributions in data compared to various MC models: PYTHIA 8 A2 (MBR), PYTHIA 8 A2 (MBR-tuned), PYTHIA 8 4C (SaS) and EPOS. The MC distributions are split into SD, ND, DD and CD components. For EPOS, SD' is separated from the ND events. Additionally, the accidental background is also shown. PYTHIA 8 A2 (MBR) predictions, shown in Fig. 4.10 (a-b), do not agree with the data, especially there is small number of events in the region of large values of  $\xi$ . This effect may be due to the scaling factors, which are introduced in PYTHIA 8 to artificially suppress diffractive cross sections in the high mass region, or due to too large Pomeron intercept ( $\epsilon = 0.104$ ). Therefore, additional two samples of PYTHIA 8 were generated: without this artificial suppression (MBR-tuned) and with  $\epsilon = 0$  (SaS). Their predictions, shown in Fig. 4.10 (c-f), agree much better with the data than PYTHIA 8 A2 (MBR) and result also in a suppression of non-SD events. Amongst PYTHIA 8 models, PYTHIA 8 A2 (MBR-tuned) shows the best agreement with the data. EPOS predictions, shown in Fig. 4.10 (g-h), describes data better than PYTHIA 8 but shows a dominant contribution of SD' events. The CD contribution in EPOS is several times greater than in PYTHIA 8 (MBR), but it was never tuned to describe any data, as opposed to PYTHIA 8 (MBR) in which the CD cross sections are constrained by CDF measurements [13]. The CD component in the SaS model is based on simple scaling assumption, therefore, it is not usually used by the experimental communities. All MCs predict significant DD and ND background at large  $\xi$ , thereby the analysis was limited to  $\xi < 0.2$ .

Figures 4.11 to 4.13 show the uncorrected distributions of variables used in the later analysis:  $n_{\text{sel}}$ ,  $p_T$  an  $\bar{\eta}$ . The contributions from non-SD (except EPOS SD') interactions differ a bit between each other, i.e. EPOS predicts significantly larger CD contribution, whereas DD and ND are suppressed in PYTHIA 8 A2 (MBR-tuned) and PYTHIA 8 4C (SaS). PYTHIA 8 A2 (MBR) is used as the default model of non-SD contribution subtracted from the data with systematic uncertainty  $\pm 50\%$ , which covers all differences between the models except EPOS SD'. In this analysis EPOS SD' is considered as an alternative to PYTHIA 8 SD model of events with forward-scattered proton in the final state, where one of the proton remnants hadronizes back to a single proton (non-diffractive process), while in PYTHIA 8 the initial proton stays intact (diffractive process). As a consequence, results are compared with the sum of SD and SD' processes for EPOS model.

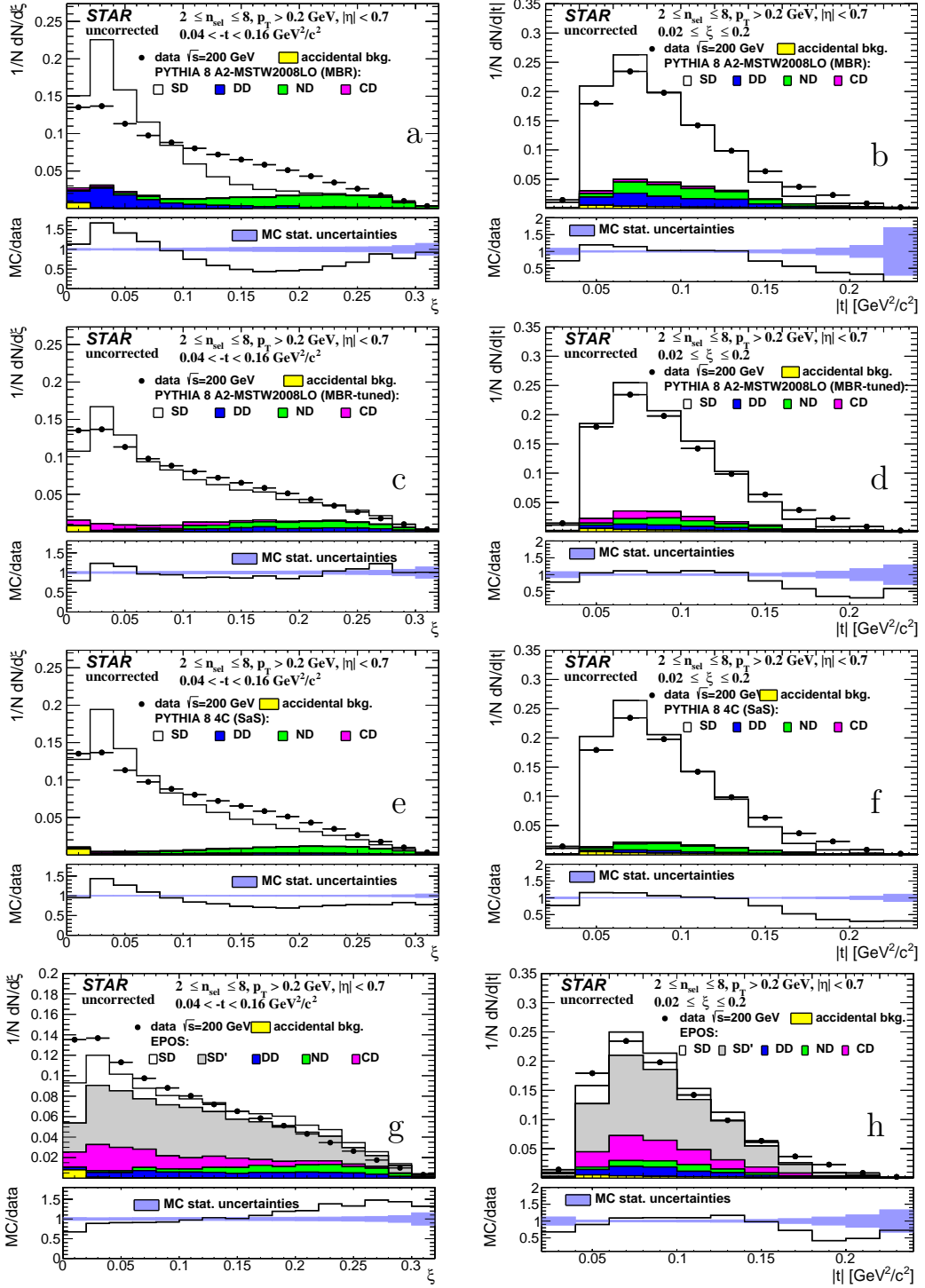


Figure 4.10: Uncorrected distributions of data compared to various MC models: (a-b) PYTHIA 8 A2 (MBR), (c-d) PYTHIA 8 A2 (MBR-tuned), (e-f) PYTHIA 8 4C (SaS) and (g-h) EPOS, as a function of (left column)  $\xi$  and (right column)  $|t|$ . The ratio of MC predictions and data is shown in the bottom panels.

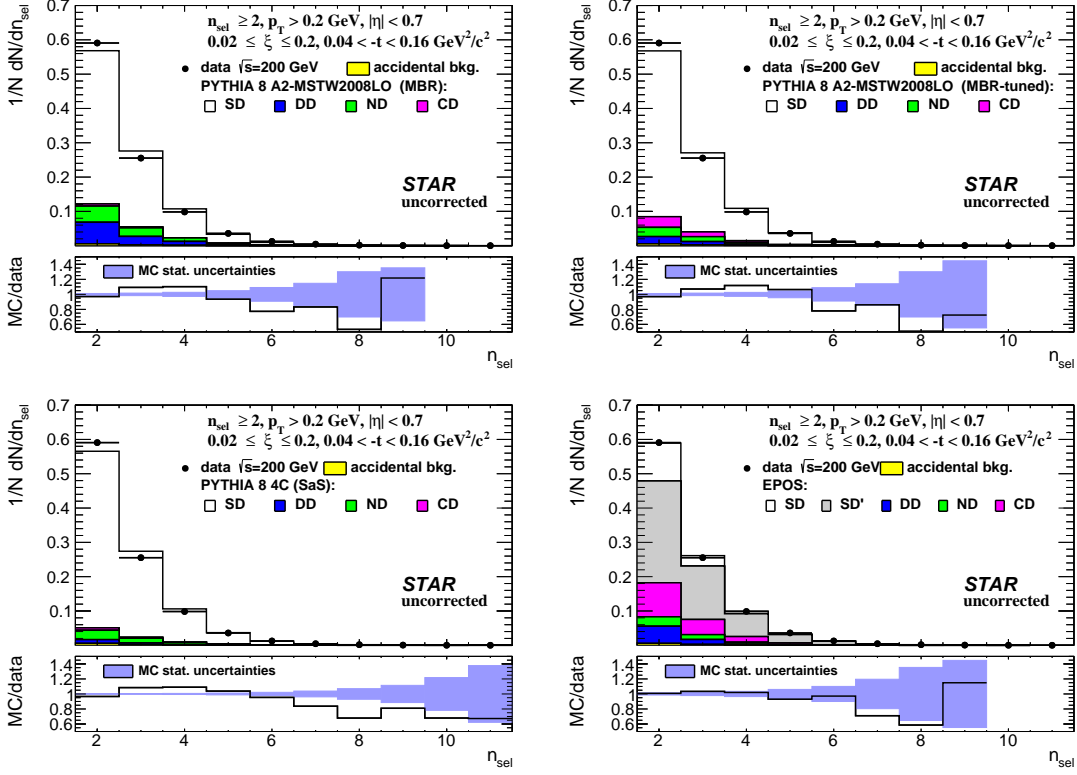


Figure 4.11: Uncorrected distributions of data compared to various MC models: (top left) PYTHIA 8 A2 (MBR), (top right) PYTHIA 8 A2 (MBR-tuned), (bottom left) PYTHIA 8 4C (SaS) and (bottom right) EPOS, as a function of  $n_{\text{sel}}$ . The ratio of MC predictions and data is shown in the bottom panels.

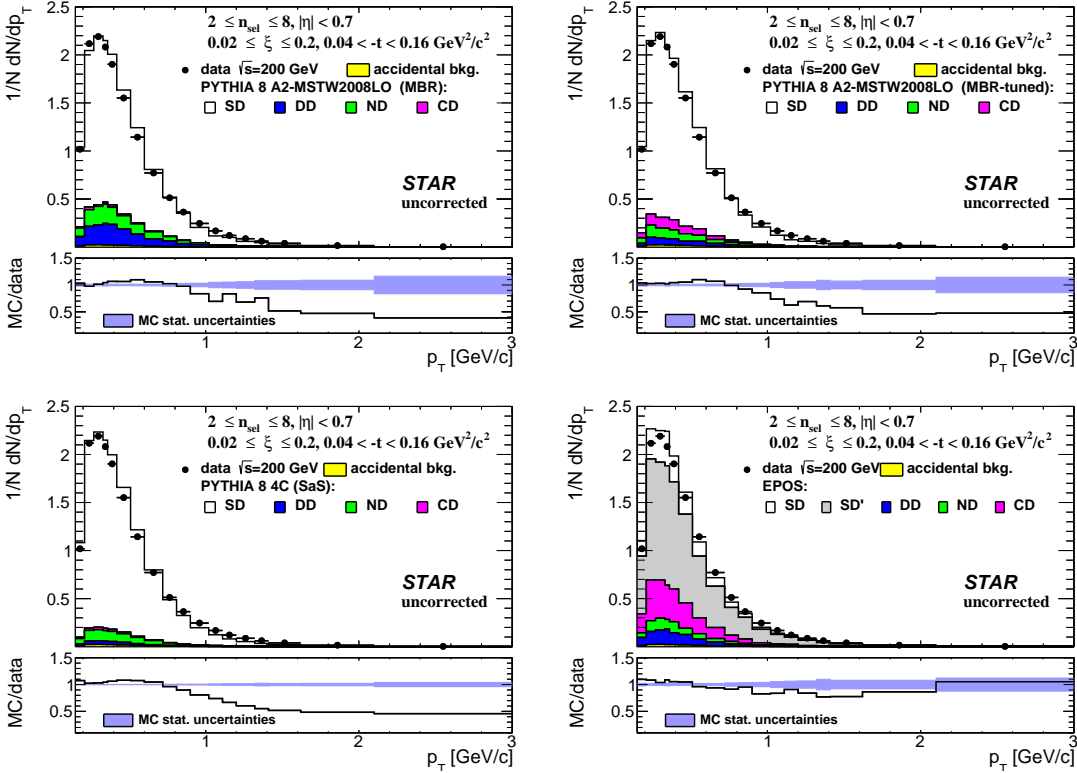


Figure 4.12: Uncorrected distributions of data compared to various MC models: (top left) PYTHIA 8 A2 (MBR), (top right) PYTHIA 8 A2 (MBR-tuned), (bottom left) PYTHIA 8 4C (SaS) and (bottom right) EPOS, as a function of  $p_T$ . The ratio of MC predictions and data is shown in the bottom panels.

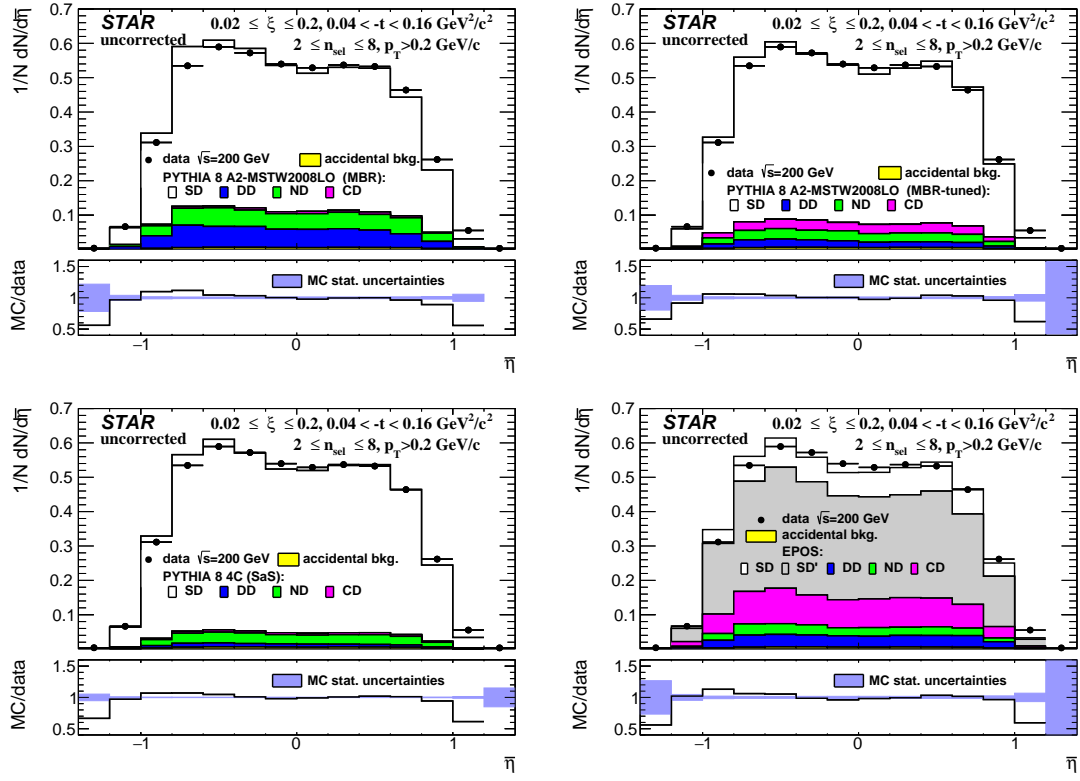


Figure 4.13: Uncorrected distributions of data compared to various MC models: (top left) PYTHIA 8 A2 (MBR), (top right) PYTHIA 8 A2 (MBR-tuned), (bottom left) PYTHIA 8 4C (SaS) and (bottom right) EPOS, as a function of  $\bar{\eta}$ . The ratio of MC predictions and data is shown in the bottom panels.

# 5. Selection Efficiencies

## 5.1 Vertex Reconstruction

When the charged-particle multiplicity is low, the vertex-finding algorithm sometimes fails to find the primary vertex. In addition, at high luminosity, vertex finder can fail due to the contribution of pile-up interactions, providing a wrong reconstructed vertex. In the study of vertex reconstruction efficiency we required at least two reconstructed global tracks  $n_{\text{sel}}^{\text{global}} \geq 2$  passing all the quality cuts listed in Sec 3.1, except vertex-related cuts on  $\text{DCA}_{xy}$  and  $\text{DCA}_z$ , and associated to true-level primary particles. Additionally, MC events were accepted if the  $z$ -coordinate of the true-level primary vertex was between  $-80$  and  $80$  cm and  $n_{\text{ch}} \geq 2$ . All corrections, described in this section, were calculated in three ranges of  $\xi$  separately using PYTHIA 8 SD embedding MC.

The global tracks (not necessarily associated to a true-level primary particles), which are used by the vertex-finder algorithm, had to pass the following quality cuts:

1. tracks must be matched with hits reconstructed in TOF,
2. the number of the TPC hits used in the helix fit  $N_{\text{hits}}^{\text{fit}}$  must be greater than 20,
3. the ratio of the number of TPC hits used in the helix fit to the number of possible TPC hits  $N_{\text{hits}}^{\text{fit}}/N_{\text{hits}}^{\text{poss}}$  must be greater than 0.52,
4. the transverse impact parameter with respect to the beamline  $d_0$  must be less than 2 cm,
5. the track's transverse momentum  $p_T$  must be greater than 0.2 GeV/c.

The above track selection criteria are different than those used in the nominal analysis. Primary vertex reconstruction efficiency and fake vertex rate were calculated as a function of the number of global tracks used in vertexing  $n_{\text{virt}}^{\text{global}}$  instead of  $n_{\text{sel}}^{\text{global}}$  ( $n_{\text{virt}}^{\text{global}} \geq n_{\text{sel}}^{\text{global}}$ ).

In the nominal analysis exactly one vertex with  $n_{\text{sel}} \geq 2$  is required. However, in the study of vertex reconstruction, events with additional vertices were studied. Therefore, we define the best vertex as the reconstructed vertex with the highest number of TOF-matched tracks. This vertex does not have to be associated to true-level primary vertex (fake or secondary vertex). The algorithm, which matches reconstructed vertices to true-level vertices, checks for reconstructed tracks originating from them. If at least one reconstructed track is assigned to a true-level particle, then the reconstructed vertex is assigned to the true-level vertex from which the true-level particle originates. Since the fake vertices (not matched to the true-level primary vertex) are allowed in the analysis, the overall vertex-finding efficiency,  $\epsilon_{\text{virt}}(n_{\text{virt}}^{\text{global}})$ , is expressed as:

$$\epsilon_{\text{virt}}(n_{\text{virt}}^{\text{global}}) = \epsilon_{\text{virt}}^{\text{best}}(n_{\text{virt}}^{\text{global}}) + \delta_{\text{virt}}^{\text{fake}}(n_{\text{virt}}^{\text{global}}) \quad (5.1)$$

where:

$\epsilon_{\text{virt}}^{\text{best}}(n_{\text{virt}}^{\text{global}})$  is the primary vertex reconstruction efficiency, determined as the ratio of the number of good reconstructed events (best primary vertex with  $n_{\text{sel}} \geq 2$  matched to the true-level primary vertex) to the number of input MC events,

$\delta_{\text{virt}}^{\text{fake}}(n_{\text{virt}}^{\text{global}})$  is the fake vertex rate, determined as the ratio of the number of good reconstructed events (best primary vertex with  $n_{\text{sel}} \geq 2$  not matched to the true-level primary vertex) to the number of input MC events. Due to the contribution of pile-up, it is possible that the best vertex originates from fake tracks instead of true-level particles.

519 The vertex-finding efficiency as a function of  $n_{\text{virt}}^{\text{global}}$ , shown in Fig. 5.1 (left), is larger than 75% for  
 520 all  $n_{\text{virt}}^{\text{global}}$ . However, for  $n_{\text{virt}}^{\text{global}} > 8$ , there are more fake than true-level primary vertices. When  
 521 there are exactly two global tracks used in the vertex reconstruction,  $n_{\text{virt}}^{\text{global}} = 2$ , the vertex-  
 522 finding efficiency depends on the longitudinal distance between these tracks  $|\Delta z_0|$ . Therefore,  
 523 the vertex-finding efficiency for such events  $\epsilon_{\text{virt}}(|\Delta z_0|)$  is given by:

$$\epsilon_{\text{virt}}(|\Delta z_0|) = \epsilon_{\text{virt}}^{\text{best}}(|\Delta z_0|) + \delta_{\text{virt}}^{\text{fake}}(|\Delta z_0|) \quad (5.2)$$

524 where:  $\epsilon_{\text{virt}}^{\text{best}}(|\Delta z_0|)$  is the primary vertex reconstruction efficiency,  $\delta_{\text{virt}}^{\text{fake}}(|\Delta z_0|)$  is the fake vertex  
 525 rate.

526 Figure 5.1 (right) shows the vertex-finding efficiency for events with  $n_{\text{virt}}^{\text{global}} = 2$ . This efficiency  
 527 is smaller than 20% for tracks with  $|\Delta z_0| > 2$  cm, hence the analysis was limited to events with  
 528  $|\Delta z_0| < 2$  cm, when  $n_{\text{virt}}^{\text{global}} = 2$ . The rate of fake vertices is negligibly low (open points overlap  
 529 with full points).

530 Events are rejected if more vertices are reconstructed in addition to the best one. Rejected  
 531 events can be classified as:

- 532 a) two or more additional vertices,
- 533 b) additional secondary vertex from interactions with the detector dead-material,
- 534 c) additional fake vertex,
- 535 d) additional primary vertex (vertex splitting or background vertex reconstructed as best ver-  
 536 tex),
- 537 e) additional secondary vertex from the decay.

538 The fraction of such events,  $f_{\text{virt}}^{\text{veto}}(n_{\text{virt}}^{\text{global}})$ , is given by:

$$f_{\text{virt}}^{\text{veto}}(n_{\text{virt}}^{\text{global}}) = \frac{\text{number of events with more than one reconstructed TOF vertex}}{\text{number of events with at least one reconstructed TOF vertex}} \quad (5.3)$$

$$= f_a + f_b + f_c + f_d + f_e$$

539 where  $f_a$  to  $f_e$  are the fractions of events with additional vertices, with labels corresponding to  
 540 the items in the listing above.

541 As before, the fraction was calculated as a function of  $|\Delta z_0|$  for events with  $n_{\text{virt}}^{\text{global}} = 2$ .  
 542 Figure 5.2 shows the fraction of multi-vertex events with respect to the  $n_{\text{virt}}^{\text{global}}$ . There is a large  
 543 fraction of events ( $> 90\%$ ) with additional background vertices for  $n_{\text{virt}}^{\text{global}} \geq 9$ , what would result  
 544 in large correction factor. Hence, the analysis was limited to events with  $n_{\text{sel}}^{\text{global}} \leq 8$  ( $n_{\text{sel}}^{\text{global}} \leq$

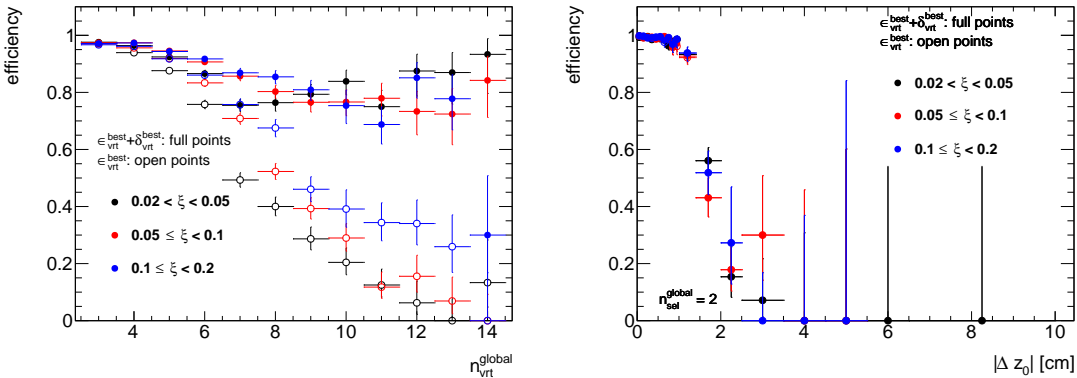


Figure 5.1: Vertex-finding efficiency in three ranges of  $\xi$  as a function of (left)  $n_{\text{virt}}^{\text{global}}$  and (right)  
 with respect to the  $|\Delta z_0|$  between reconstructed tracks in events with  $n_{\text{virt}}^{\text{global}} = 2$ .

545  $n_{\text{vrt}}^{\text{global}}$ ). The total fraction of multi-vertex events,  $f_a + f_b + f_c + f_d + f_e$ , as a function of  $n_{\text{vrt}}^{\text{global}}$   
546 and  $|\Delta z_0|$ , shown in Fig. 5.3, demonstrates that  $f_{\text{veto}}^{\text{veto}}(|\Delta z_0|)$  is very small (< 2%) for events with  
547  $n_{\text{vrt}}^{\text{global}} = 2$ .

548 Although, the analysis was limited to  $n_{\text{sel}}^{\text{global}} \leq 8$  ( $n_{\text{sel}}^{\text{global}} \leq n_{\text{vrt}}^{\text{global}}$ ), a fraction of events with  
549 additional background vertices was still relatively large. Since most of these additional vertices  
550 are fake (and as accidental not correlated with true-level primary distributions), it was checked  
551 whether the charged-particle multiplicity distributions are different for events with and without  
552 reconstructed fake vertices. These distributions, as shown in Fig 5.4, are in good agreement, thus,  
553 above studies of vertex reconstruction were repeated using MC events that do not contain recon-  
554 structed fake vertices. It means that events with additional fake vertex were rejected (similarly to  
555 the analysis of real data) and no correction is needed for such losses since it only affects overall  
556 normalization (not the shapes of distributions under study). The vertex-finding efficiency, which  
557 was calculated from such events, is shown in Fig. 5.5. It is greater than 95% for events with  
558  $2 \leq n_{\text{vrt}}^{\text{global}} \leq 8$ . In addition, the corresponding fraction of multi-vertex events, shown in Figs. 5.6

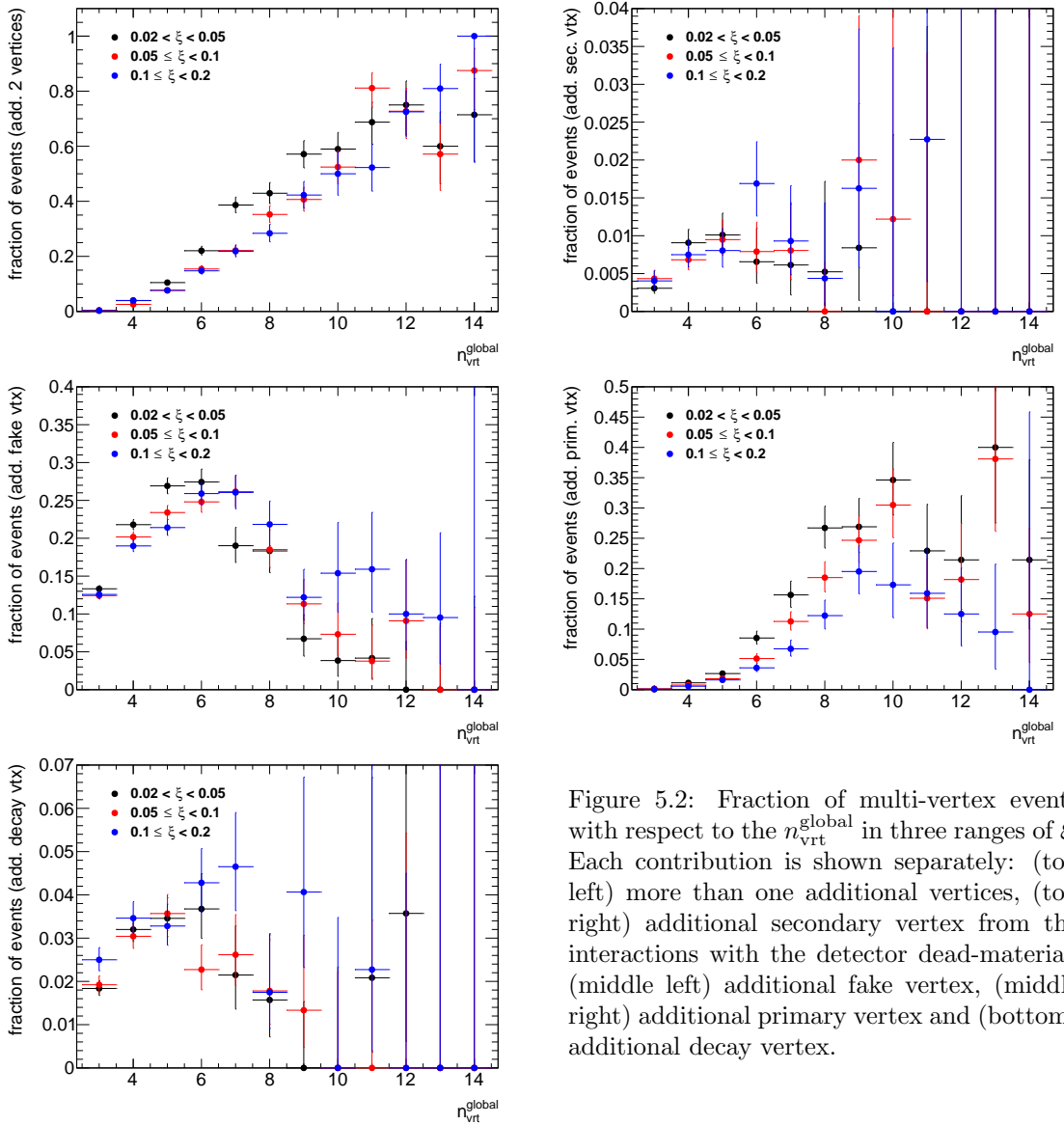


Figure 5.2: Fraction of multi-vertex events with respect to the  $n_{\text{vrt}}^{\text{global}}$  in three ranges of  $\xi$ . Each contribution is shown separately: (top left) more than one additional vertices, (top right) additional secondary vertex from the interactions with the detector dead-material, (middle left) additional fake vertex, (middle right) additional primary vertex and (bottom) additional decay vertex.

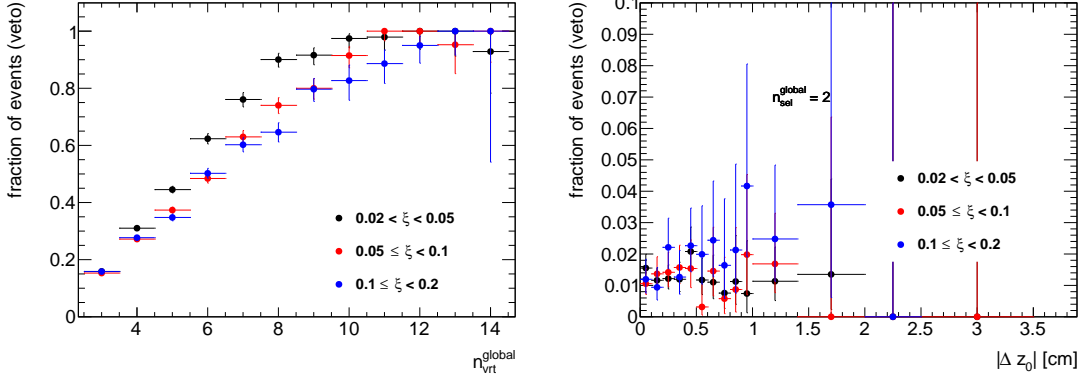


Figure 5.3: Total fraction of multi-vertex events as a function of (left)  $n_{\text{vrt}}^{\text{global}}$  for events with  $n_{\text{vrt}}^{\text{global}} > 2$  and (right)  $|\Delta z_0|$  for events with  $n_{\text{vrt}}^{\text{global}} = 2$  in three ranges of  $\xi$ .

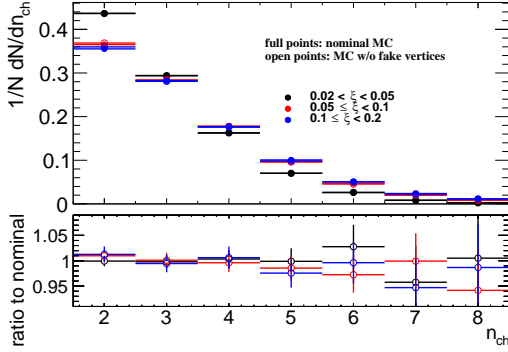


Figure 5.4: Normalized charged-particle multiplicity distributions in three ranges of  $\xi$  calculated from PYTHIA 8 SD embedding MC for (full points) all generated events and (open points) events without reconstructed fake vertices.

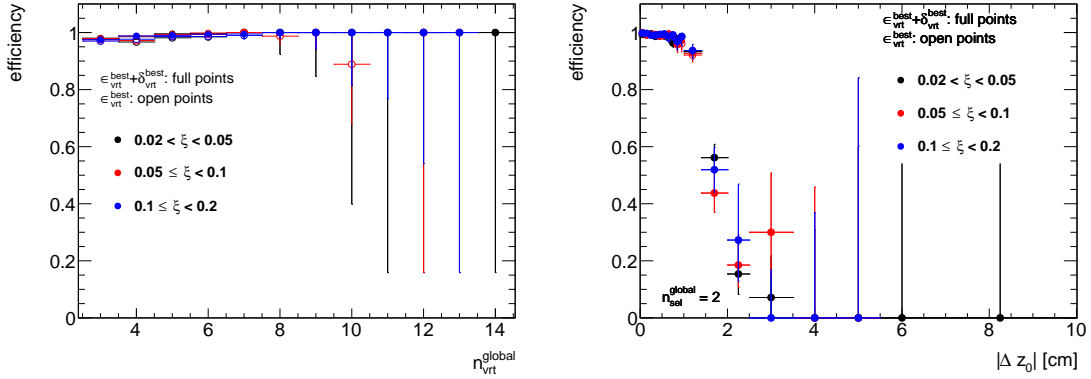


Figure 5.5: Vertex-finding efficiency in three ranges of  $\xi$  as a function of (left)  $n_{\text{vrt}}^{\text{global}}$  and (right) with respect to the  $|\Delta z_0|$  between reconstructed tracks in events with  $n_{\text{vrt}}^{\text{global}} = 2$ . Only events that do not contain additional fake vertices were used.

and 5.7, is smaller than 20%. Since fake vertices were rejected from this study, the  $f_c$  term from Eq. (5.3) is equal to 0. The correction factors calculated from MC events that do not contain reconstructed fake vertices were used in the analysis instead of the one obtained from the full MC sample.

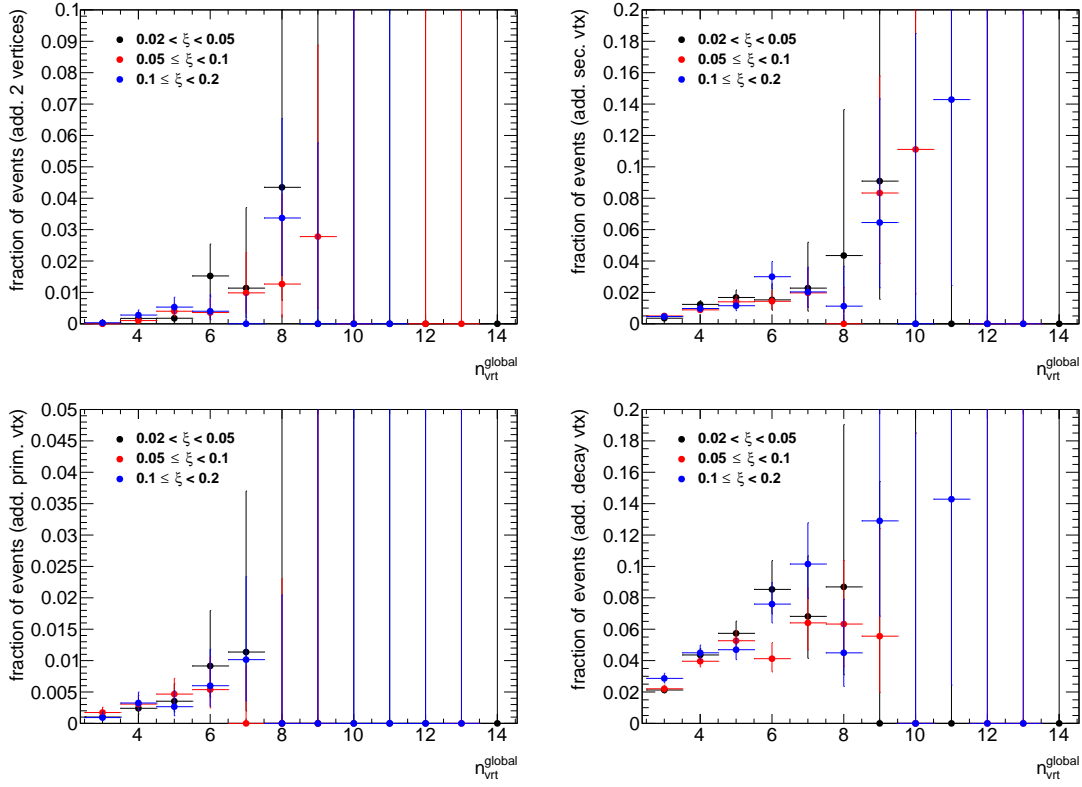


Figure 5.6: Fraction of multi-vertex events with respect to the  $n_{\text{vrt}}^{\text{global}}$  in three ranges of  $\xi$ . Each contribution is shown separately: (top left) more than one additional vertices, (top right) additional secondary vertex from the interactions with the detector dead-material, (bottom left) additional primary vertex and (bottom right) additional decay vertex. Only events that do not contain additional fake vertices were used.

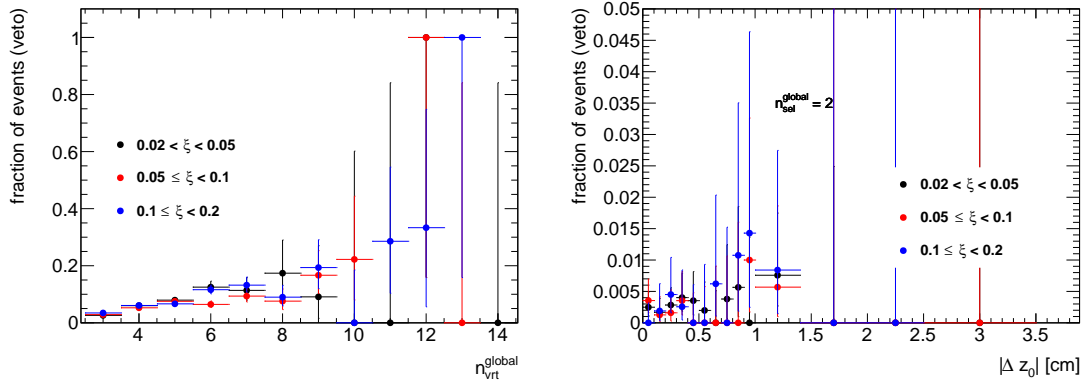


Figure 5.7: Total fraction of multi-vertex events as a function of (left)  $n_{\text{vrt}}^{\text{global}}$  for events with  $n_{\text{vrt}}^{\text{global}} > 2$  and (right)  $|\Delta z_0|$  for events with  $n_{\text{vrt}}^{\text{global}} = 2$  in three ranges of  $\xi$ . Only events that do not contain additional fake vertices were used.

## 5.2 Correction to BBC-Small

The SDT trigger conditions imposed a signal in RPs and a veto on any signal in the same-side small BBC tiles, whereas a signal in the opposite-side BBC-small was required by the offline event selection. These requirements were imposed in order to accept only events with rapidity gap and reduce DD, ND and accidental backgrounds. A joined BBC-small efficiency,  $\epsilon_{BBC}$ , was obtained as a function of each measured quantity using PYTHIA 8 4C (SaS) SD embedded into Zerobias data, EPOS SD+SD' and HERWIG SD MC. The efficiency was calculated for events within fiducial region as follows:

$$\epsilon_{BBC} = \frac{\text{number of MC events satisfying the BBC-small selection criteria}}{\text{number of MC events}} \quad (5.4)$$

Figures 5.8 to 5.10 show the fraction of generated true-level MC events, within the fiducial region of the measurement, in which the selection criteria on BBC-small signal and veto are fulfilled. The efficiency weakly depends on the measured variables ( $n_{ch}$ ,  $p_T$  and  $\bar{\eta}$ ). In addition, veto, signal and joined BBC-small efficiencies are presented separately as a function of  $\xi$  in Fig. 5.11. The  $\epsilon_{BBC}$  strongly depends on  $\xi$  and varies from about 90% for events with  $\xi$  within 0.02 – 0.05 to about 60% for events with  $0.1 < \xi < 0.2$ . However, measurements of corrected  $\xi$  distributions are out of the scope of this analysis.

Data is corrected for BBC-small efficiency using PYTHIA 8 4C (SaS). The uncertainty related to this correction is estimated by using HERWIG and EPOS SD+SD' samples, where the hadronization models are different from that used in PYTHIA 8. Figure 5.12 shows the PYTHIA 8 prediction on BBC efficiency divided by the HERWIG prediction in three ranges of  $\xi$ . The deviations between these two models are of the order of 4% at  $0.02 < \xi < 0.05$ , 2% at  $0.05 < \xi < 0.1$  and about 10% at  $0.1 < \xi < 0.2$ . The differences between PYTHIA 8 and EPOS SD+SD' predictions are shown in Fig. 5.13. Most of them are of the order of 3%, except  $n_{ch} \leq 3$  for which the difference varies up to 6%. The maximum difference between PYTHIA 8 and HERWIG/EPOS hadronization models is used as systematic uncertainty.

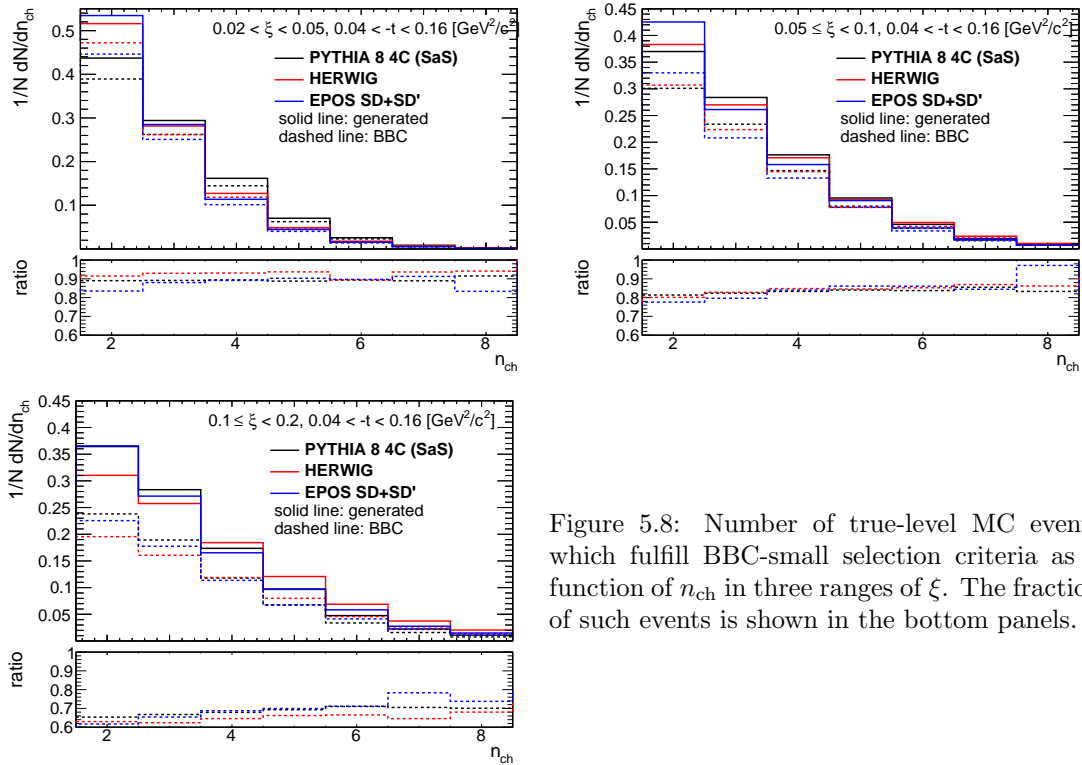


Figure 5.8: Number of true-level MC events which fulfill BBC-small selection criteria as a function of  $n_{ch}$  in three ranges of  $\xi$ . The fraction of such events is shown in the bottom panels.

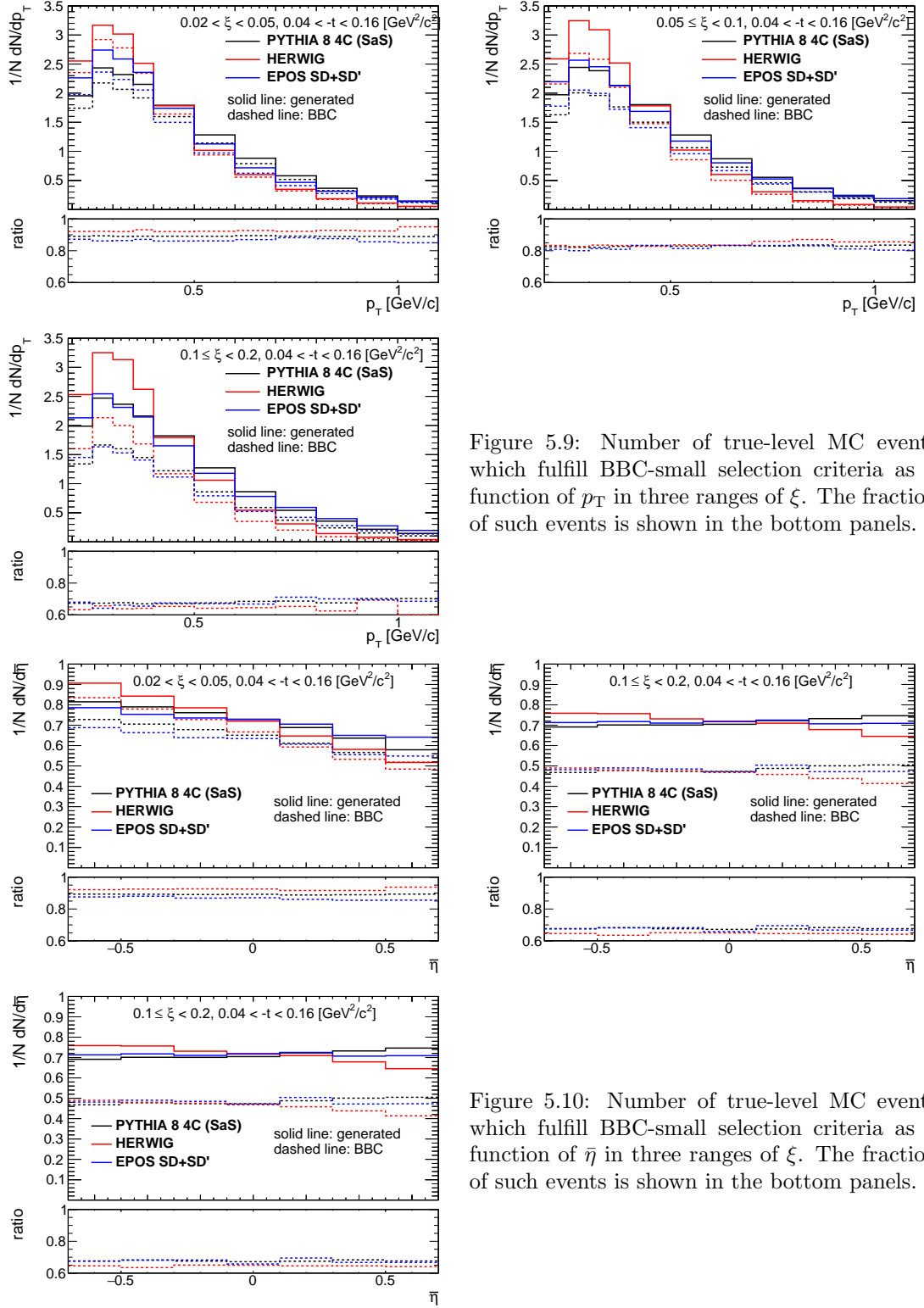


Figure 5.9: Number of true-level MC events which fulfill BBC-small selection criteria as a function of  $p_T$  in three ranges of  $\xi$ . The fraction of such events is shown in the bottom panels.

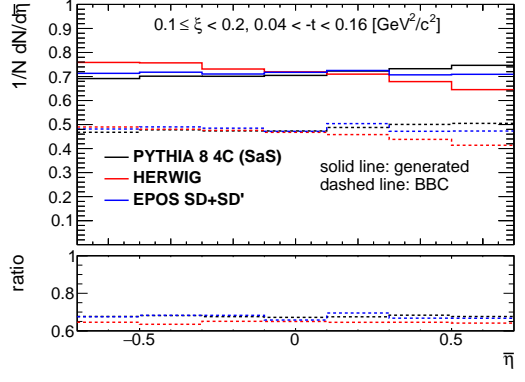


Figure 5.10: Number of true-level MC events which fulfill BBC-small selection criteria as a function of  $\bar{\eta}$  in three ranges of  $\xi$ . The fraction of such events is shown in the bottom panels.

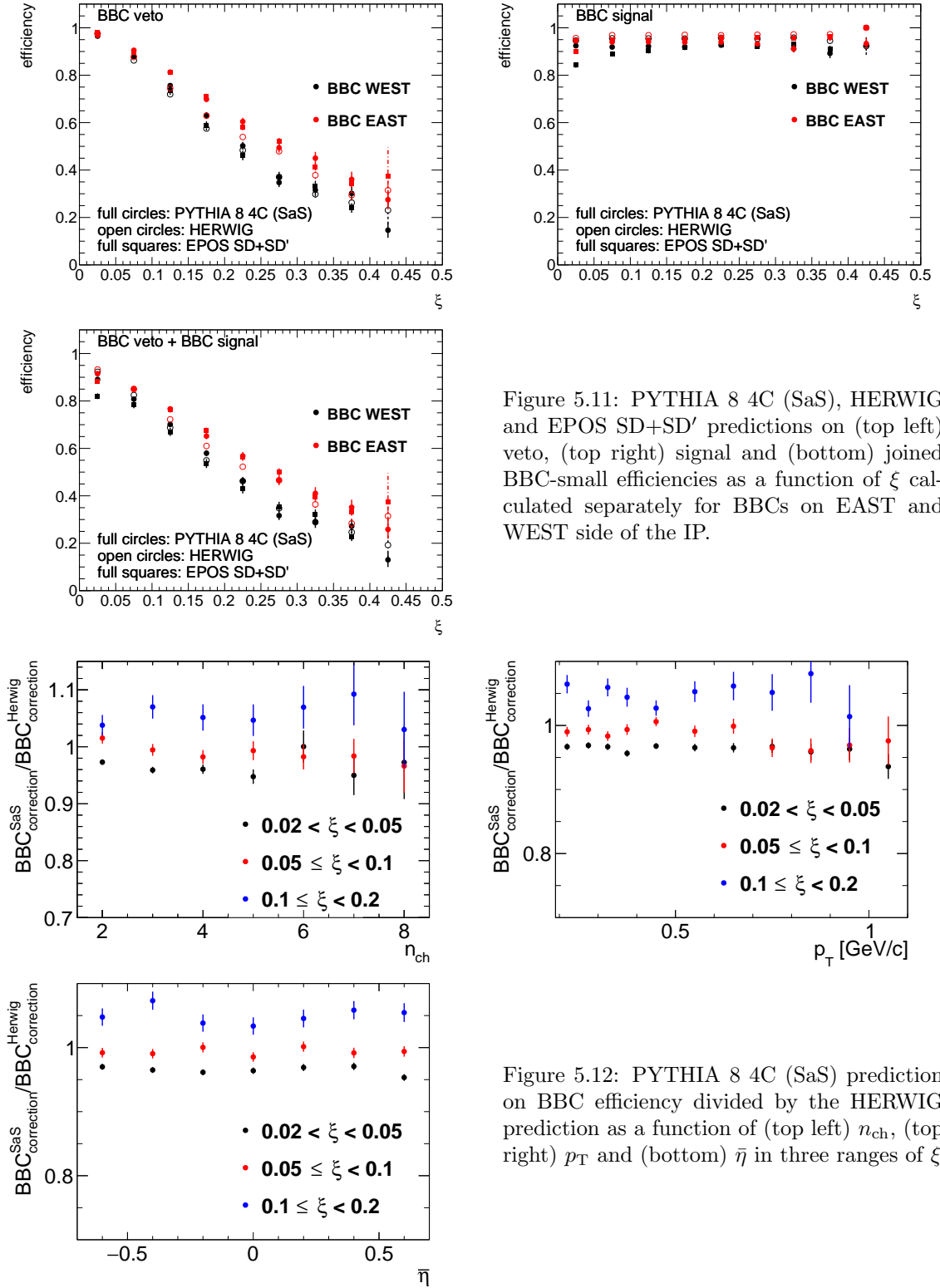


Figure 5.11: PYTHIA 8 4C (SaS), HERWIG and EPOS SD+SD' predictions on (top left) veto, (top right) signal and (bottom) joined BBC-small efficiencies as a function of  $\xi$  calculated separately for BBCs on EAST and WEST side of the IP.

Figure 5.12: PYTHIA 8 4C (SaS) prediction on BBC efficiency divided by the HERWIG prediction as a function of (top left)  $n_{ch}$ , (top right)  $p_T$  and (bottom)  $\bar{\eta}$  in three ranges of  $\xi$

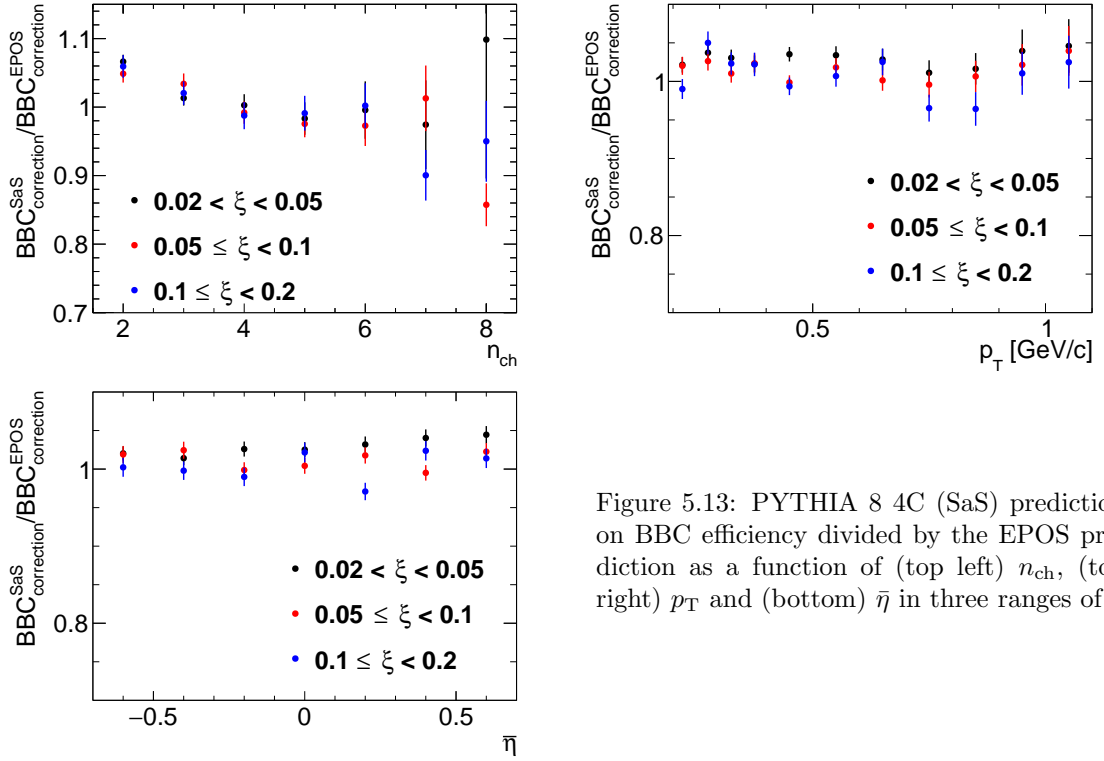


Figure 5.13: PYTHIA 8 4C (SaS) prediction on BBC efficiency divided by the EPOS prediction as a function of (top left)  $n_{\text{ch}}$ , (top right)  $p_{\text{T}}$  and (bottom)  $\bar{\eta}$  in three ranges of  $\xi$

# 6. Migrations into and out of the Fiducial Region

In this section the corrections due to the migrations of tracks and forward-scattered protons into and out of the fiducial region are described.

## 6.1 Migrations of Tracks into and out of the Fiducial Region

The procedure, described in this section, accounts for migrations of tracks into and out of the fiducial region, which originate from TPC resolution effects. The correction factor for such tracks,  $f_{\text{okr}}(p_T, \eta)$  is defined as follows:

$$f_{\text{okr}}(p_T, \eta) = \frac{1 - f_{\text{okr}}^-(p_T, \eta)}{1 - f_{\text{okr}}^+(p_T, \eta)} \quad (6.1)$$

where  $f_{\text{okr}}^-(p_T, \eta)$  is the fraction of reconstructed tracks for which the corresponding primary particle is outside of the kinematic range of the measurement and  $f_{\text{okr}}^+(p_T, \eta)$  is the fraction of primary particles for which the corresponding reconstructed track is outside of the kinematic range of the measurement.

The resulting residual migrations, shown in Fig. 6.1, were estimated using PYTHIA 8 SD embedding MC. The main effect was observed at  $|\eta| \sim 0.7$ , where about 2 – 6% reconstructed tracks were associated to primary particle outside the fiducial region. However, above contributions to the correction factor,  $f_{\text{okr}}(p_T, \eta)$ , cancel each other and the resulting factor is about 2% at  $|\eta| \sim 0.7$ .

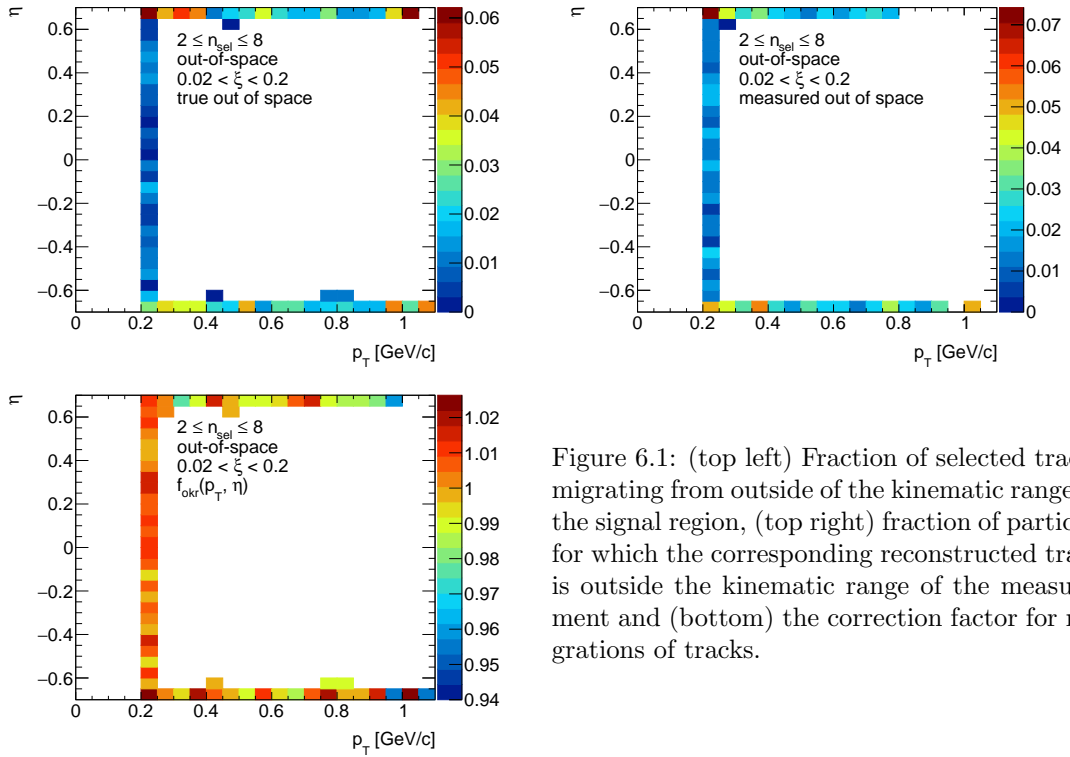


Figure 6.1: (top left) Fraction of selected tracks migrating from outside of the kinematic range to the signal region, (top right) fraction of particles for which the corresponding reconstructed track is outside of the kinematic range of the measurement and (bottom) the correction factor for migrations of tracks.

## 6.2 Migrations in $\xi$

The analysis was performed in three ranges of  $\xi$ . Thus, there are migrations into and out of these  $\xi$  regions. They mainly originate from the resolution of  $\xi$  reconstructed from RP tracks. Figure 6.2 shows the resolution of  $\xi$  as a function of the true-level  $\xi$  (denoted as  $\xi_{\text{true}}$ ) with fitted zeroth order polynomial. The resolution of  $\xi$  is fairly constant and equals to about 0.3%.

The corrections due to migrations into and out of  $\xi$  regions was defined as:

$$f_\xi = \frac{1 - f_\xi^-}{1 - f_\xi^+} \quad (6.2)$$

where  $f_\xi^-$  is the fraction of events for which the corresponding true-level,  $\xi_{\text{true}}$ , is outside of the  $\xi$  region and  $f_\xi^+$  is the fraction of events for which the corresponding reconstructed,  $\xi_{\text{reco}}$ , is outside of the  $\xi$  region.

The  $f_\xi$  was calculated for each measured variable separately. Figures 6.3 to 6.5 show the fraction of events  $f_\xi^-$  and  $f_\xi^+$  as a function of  $n_{\text{ch}}$ ,  $p_{\text{T}}$  and  $\bar{\eta}$ . The lower panel in each figure shows the corresponding correction factor  $f_\xi$ . The largest differences between migrations into and out of the  $\xi$  regions were observed at  $0.02 < \xi < 0.05$ , where they are of the order of 2 – 4%. In the other  $\xi$  regions, the difference between  $f_\xi^-$  and  $f_\xi^+$  is smaller than 1%.

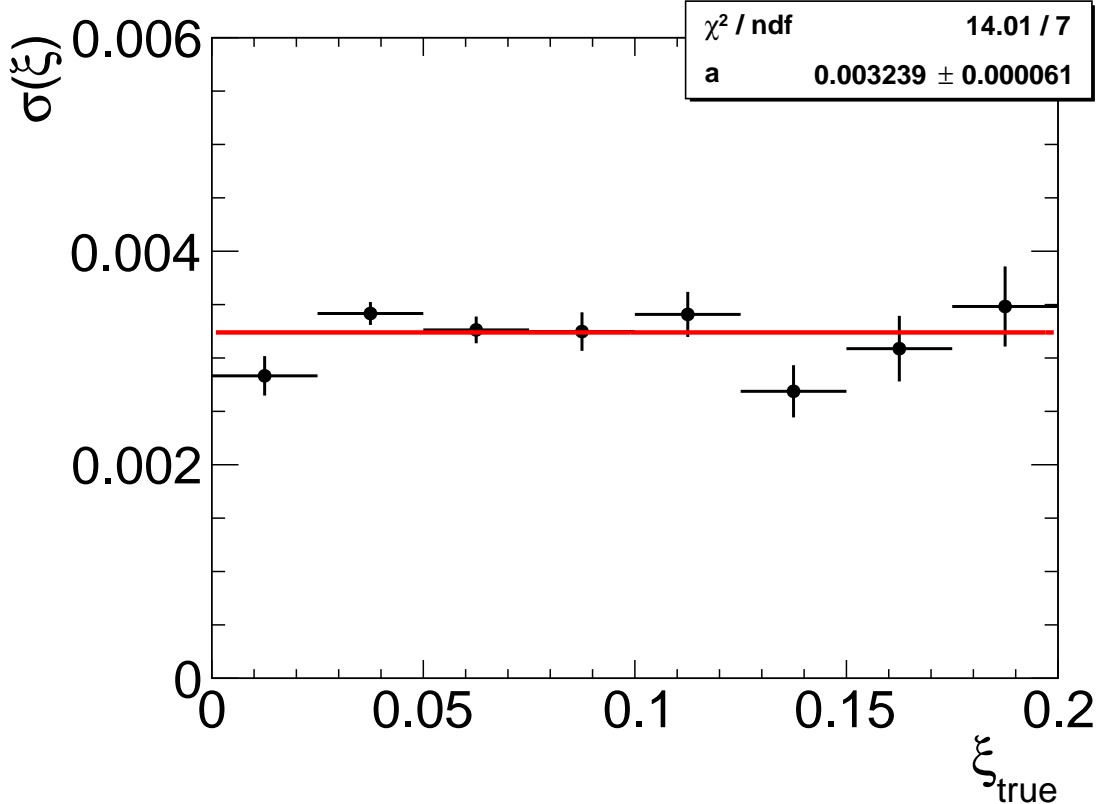


Figure 6.2: The resolution of  $\xi$  as a function of  $\xi_{\text{true}}$ . The zeroth order polynomial, shown as red line, was fitted.

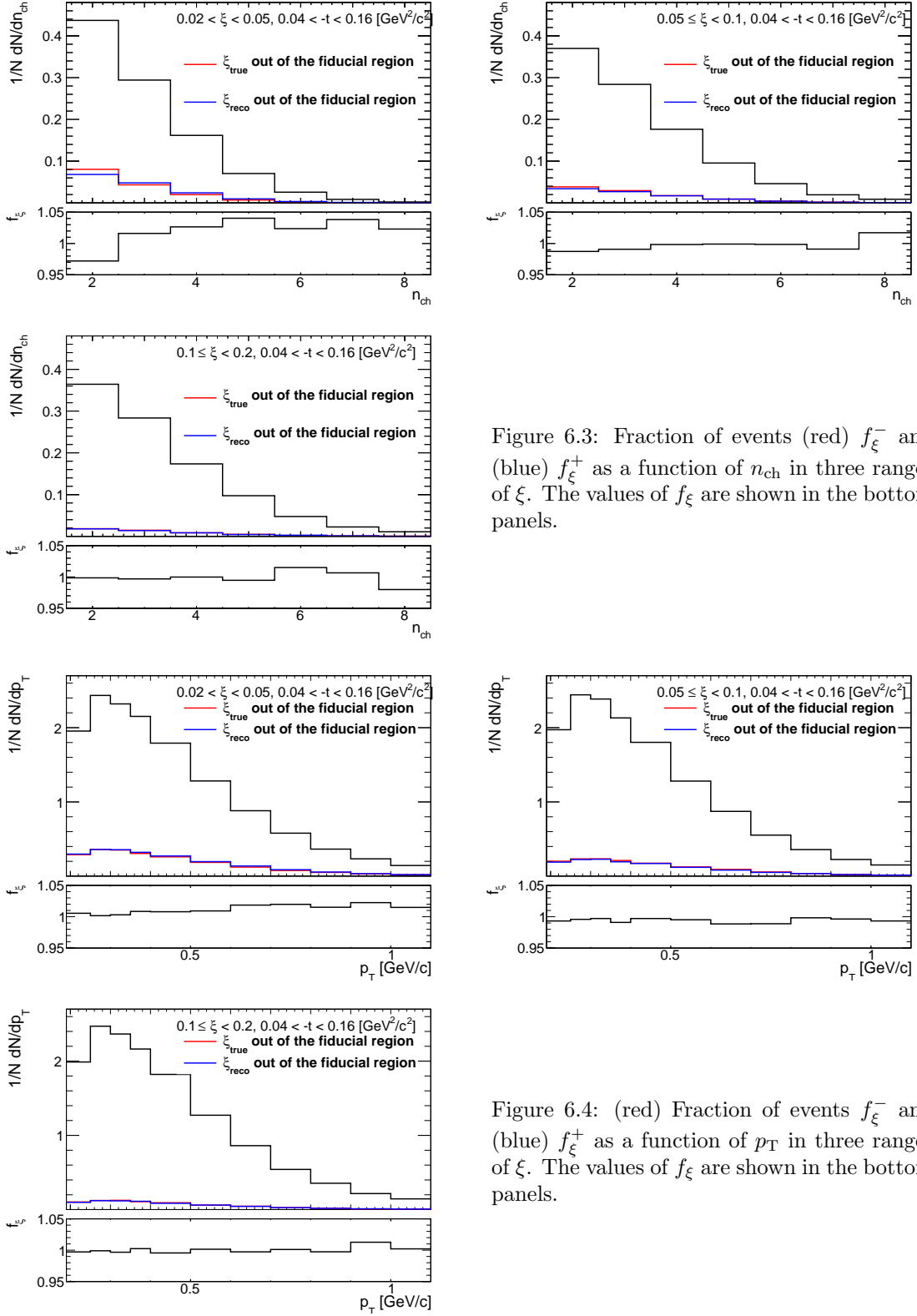


Figure 6.3: Fraction of events (red)  $f_\xi^-$  and (blue)  $f_\xi^+$  as a function of  $n_{ch}$  in three ranges of  $\xi$ . The values of  $f_\xi$  are shown in the bottom panels.

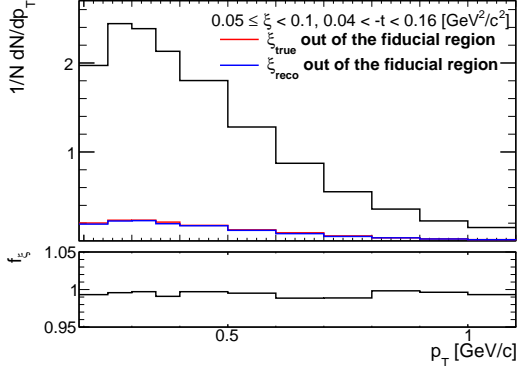


Figure 6.4: (red) Fraction of events  $f_\xi^-$  and (blue)  $f_\xi^+$  as a function of  $p_T$  in three ranges of  $\xi$ . The values of  $f_\xi$  are shown in the bottom panels.

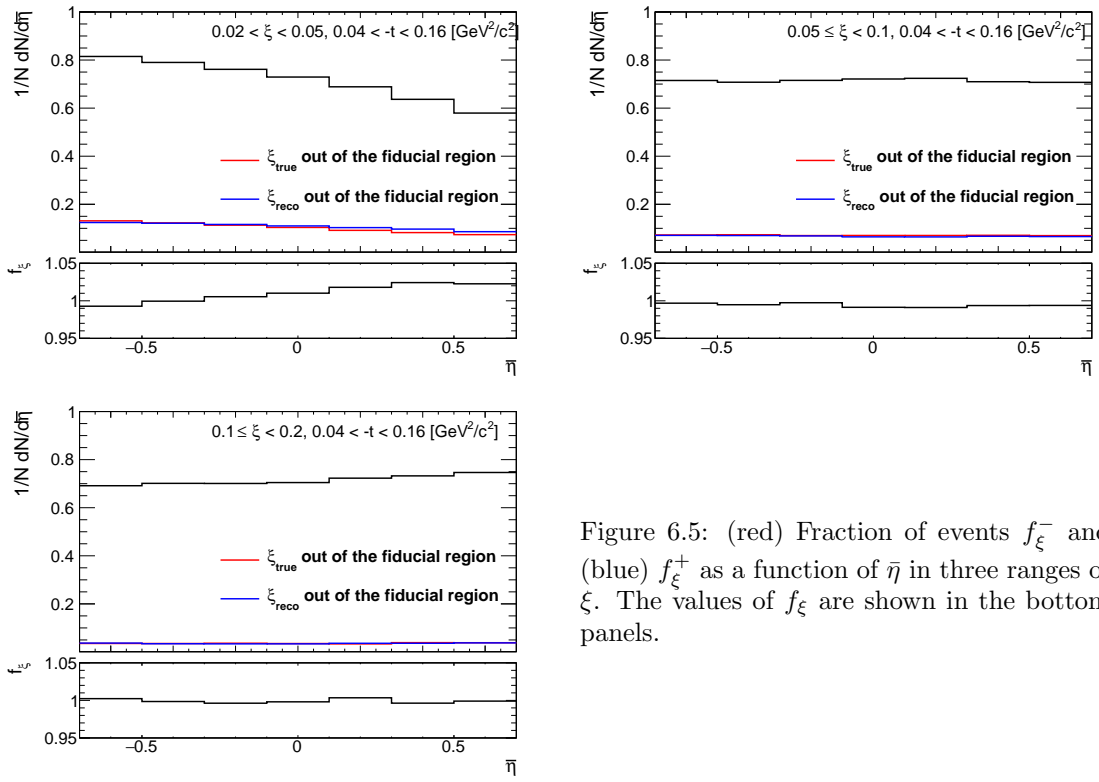


Figure 6.5: (red) Fraction of events  $f_\xi^-$  and (blue)  $f_\xi^+$  as a function of  $\bar{\eta}$  in three ranges of  $\xi$ . The values of  $f_\xi$  are shown in the bottom panels.

# 618 7. Event Corrections and 619 Unfolding Procedure

620 After subtraction of accidental, DD, CD and ND backgrounds (as described in Sec. 4 and 4.2),  
621 the data was corrected for detector inefficiencies to obtain the distributions of charged particles  
622 and particle to antiparticle (pion, kaon, proton and their antiparticle) multiplicity ratios. These  
623 corrections include:

- 624 • event-by-event weights due to vertex reconstruction efficiency:

$$w_{\text{ev}}^{\text{vrt}}(n_{\text{vrt}}^{\text{global}}, |\Delta z_0|) = \frac{1}{\epsilon_{\text{vrt}}(n_{\text{vrt}}^{\text{global}}, |\Delta z_0|)} \cdot \frac{1}{1 - f_{\text{veto}}(n_{\text{vrt}}^{\text{global}}, |\Delta z_0|)} \quad (7.1)$$

625 where the  $|\Delta z_0|$  dependence is only applicable for events with  $n_{\text{vrt}}^{\text{global}} = 2$  as described in  
626 Sec. 5.1.

- 627 • track-by-track weights due to track reconstruction efficiency, track backgrounds, migrations  
628 of tracks into and out of the fiducial region:

$$w_{\text{trk}}(p_T, \eta, V_z) = \frac{1 - f_{\text{bkg}}(p_T, \eta) - f_{\text{fake}}(p_T, \eta)}{\epsilon_{\text{TPC}}(p_T, \eta, V_z) \epsilon_{\text{TOF}}(p_T, \eta, V_z)} f_{\text{okr}}(p_T, \eta) \quad (7.2)$$

629 where:  $\epsilon_{\text{TPC}}(p_T, \eta, V_z)$  is TPC track reconstruction efficiency [1],  $\epsilon_{\text{TOF}}(p_T, \eta, V_z)$  is TOF  
630 matching efficiency [1],  $f_{\text{okr}}(p_T, \eta)$  is a factor accounting for migrations of tracks into and  
631 out of the fiducial region,  $f_{\text{bkg}}(p_T, \eta)$  is a fraction of background tracks, and  $f_{\text{fake}}(p_T, \eta)$   
632 is a fraction of fake tracks. These corrections were not applied for  $n_{\text{ch}}$  measurements since  
633 they were taken into account in the unfolding procedure.

- 634 • event-by-event (for  $n_{\text{ch}}$  distribution ) or track-by-track (for  $p_T, \bar{\eta}$  distributions) weights,  $f_\xi$ ,  
635 due to migrations of events between three  $\xi$  regions.

636 Additionally, the obtained distributions were corrected for BBC-small efficiency,  $\epsilon_{\text{BBC}}$ , using  
637 the following weight, which was calculated for each true-level quantity  $(n_{\text{ch}}, p_T, \bar{\eta})$  in three ranges  
638 of  $\xi$  separately:

$$w_{\text{BBC}} = \frac{1}{\epsilon_{\text{BBC}}} \quad (7.3)$$

639 In the following sections, the correction procedure for each of the measured distributions is  
640 presented separately.

## 641 7.1 Correction to $dN/dn_{\text{sel}}$

642 In order to express the multiplicity distribution in terms of the number of charged particles,  $n_{\text{ch}}$ ,  
643 instead of the number of selected tracks,  $n_{\text{sel}}$ , the following procedure based on the Bayesian unfolding  
644 [14, 15] was used. First, the  $n_{\text{sel}}$  distribution was corrected for vertex reconstruction effects  
645 by applying event-by-event weights,  $w_{\text{ev}}^{\text{vrt}}(n_{\text{vrt}}^{\text{global}}, |\Delta z_0|)$ . The number of events in which  $n_{\text{ch}}$  are  
646 produced,  $N_{\text{ev}}(n_{\text{ch}})$ , can be associated with the number of events in which  $n_{\text{sel}}$  are reconstructed,  
647  $N_{\text{ev}}(n_{\text{sel}})$ . Since there are several possible  $n_{\text{sel}}$  observed in  $n_{\text{ch}}$  event,  $N_{\text{ev}}(n_{\text{ch}})$  is given by:

$$\begin{aligned} N_{\text{ev}}(n_{\text{ch}}) &= \sum_{n_{\text{sel}}=0}^8 P(n_{\text{ch}}|n_{\text{sel}}) \cdot N_{\text{ev}}(n_{\text{sel}}) \\ &= \frac{1}{\epsilon_m(n_{\text{ch}})\epsilon_r(n_{\text{ch}})} \sum_{n_{\text{sel}}=2}^8 P(n_{\text{ch}}|n_{\text{sel}}) \cdot N_{\text{ev}}(n_{\text{sel}}) \end{aligned} \quad (7.4)$$

648 where:

649      $P(n_{\text{ch}}|n_{\text{sel}})$  is the conditional probability of having  $n_{\text{ch}}$  charged particles in an event in which  
 650      $n_{\text{sel}}$  tracks were found,

651      $\epsilon_m(n_{\text{ch}})$  is a factor, which recovers events that are lost due to TPC track reconstruction and TOF  
 652     matching inefficiencies, i.e. those with  $n_{\text{ch}} \geq 2$  but  $n_{\text{sel}} < 2$ ,

653      $\epsilon_r(n_{\text{ch}})$  is a factor, which recovers events which are lost due to fake tracks, i.e. those with  $n_{\text{ch}} \leq 8$   
 654     but  $n_{\text{sel}} > 8$ . It was checked that this effect is negligible (smaller than 1%) and can be  
 655     omitted.

656     Figure 7.1 shows  $\epsilon_m(n_{\text{ch}})$  in three ranges of  $\xi$ . It was derived from PYTHIA 8 embedding MC  
 657     and varies from about 25% for  $n_{\text{ch}} = 2$  to 95% for  $n_{\text{ch}} = 8$ . Since there are additional data-driven  
 658     corrections to TPC and TOF efficiencies, MC simulations were modified by randomly removing  
 659     or adding tracks. This was done in accordance with differences in the efficiencies between data  
 660     and MC. Figure 7.2 shows  $\epsilon_m(n_{\text{ch}})$  calculated in three ranges of  $\xi$  using no-pile-up PYTHIA 8 and  
 661     EPOS SD+SD'. The differences between these two models, which are up to 12% for  $n_{\text{ch}} = 2$  and  
 662      $0.02 < \xi < 0.05$ , were symmetrized and taken as a systematic uncertainty.

663     The probability  $P(n_{\text{ch}}|n_{\text{sel}})$  can be derived using Bayes' theorem, which can be stated mathematically  
 664     in terms of charged particle and charged track multiplicities as:

$$P(n_{\text{sel}}|n_{\text{ch}}) \cdot P(n_{\text{ch}}) = P(n_{\text{ch}}|n_{\text{sel}}) \cdot P(n_{\text{sel}}) \quad (7.5)$$

665     where:  $P(n_{\text{sel}})$  and  $P(n_{\text{ch}})$  are probabilities of observing  $n_{\text{sel}}$  and  $n_{\text{ch}}$  respectively,  $P(n_{\text{ch}}|n_{\text{sel}})$  and  
 666      $P(n_{\text{sel}}|n_{\text{ch}})$  are conditional probabilities.

667     In order to improve the estimate of  $P(n_{\text{ch}}|n_{\text{sel}})$ , the unfolding is done iteratively:

- 668         • In the first iteration, it is assumed that:

$$P(n_{\text{ch}}|n_{\text{sel}}) = P = P^{\text{MC}}(n_{\text{sel}}|n_{\text{ch}}) \frac{P^{\text{MC}}(n_{\text{ch}})}{P^{\text{MC}}(n_{\text{sel}})} \quad (7.6)$$

$$N_{\text{ev}}(n_{\text{ch}}) = \frac{1}{\epsilon_m(n_{\text{ch}})} \sum_{n_{\text{sel}}=2}^8 N_{\text{ev}}(n_{\text{sel}}) \cdot P \quad (7.7)$$

671     where  $P^{\text{MC}}(n_{\text{sel}}|n_{\text{ch}})$ ,  $P^{\text{MC}}(n_{\text{ch}})$  and  $P^{\text{MC}}(n_{\text{sel}})$  are obtained from MC.  $P^{\text{MC}}(n_{\text{sel}}|n_{\text{ch}})$  is  
 672     the same for each iteration.

- 673         • In the  $(i + 1)$ th iteration we have:

$$P^{i+1} = P^{\text{MC}}(n_{\text{sel}}|n_{\text{ch}}) \frac{N_{\text{ev}}^i(n_{\text{ch}})}{N_{\text{ev}}(n_{\text{sel}})} \quad (7.8)$$

$$N_{\text{ev}}^{i+1}(n_{\text{ch}}) = \frac{1}{\epsilon_m(n_{\text{ch}})} \sum_{n_{\text{sel}}=2}^8 N_{\text{ev}}(n_{\text{sel}}) \cdot P^{i+1} \quad (7.9)$$

675     where  $N_{\text{ev}}^i(n_{\text{ch}})$  is calculated in the previous iteration, and  $N_{\text{ev}}(n_{\text{sel}})$  is taken from data.

676     The unfolding matrices  $P(n_{\text{ch}}|n_{\text{sel}})$  for each  $\xi$  region, shown in Fig. 7.3, were obtained from  
 677     PYTHIA 8 embedding MC and used in all iterations of the above procedure. Similarly to  $\epsilon_m(n_{\text{ch}})$ ,  
 678     the matrices were modified by randomly removing or adding tracks in order to take into account  
 679     additional data-driven corrections to TPC and TOF efficiencies. In order to increase statistical  
 680     precision of the unfolding matrices, all simulated events were used, i.e. also those with additional  
 681     fake vertices (with  $n_{\text{sel}}$  defined as a number of primary tracks associated with the best vertex).  
 682     The systematic uncertainty related to limited statistics in PYTHIA 8 was estimated by performing  
 683     50 pseudo-experiments, in which the unfolding matrices were smeared according to their statistical

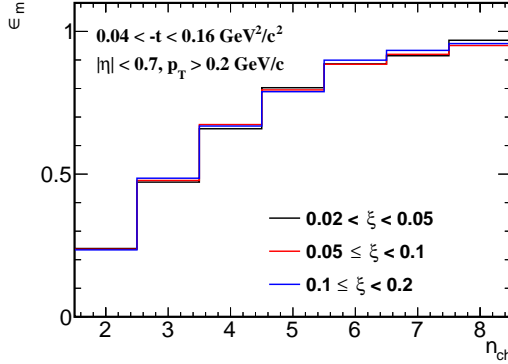


Figure 7.1:  $\epsilon_m(n_{ch})$  calculated separately in three ranges of  $\xi$  using PYTHIA 8 embedding MC.

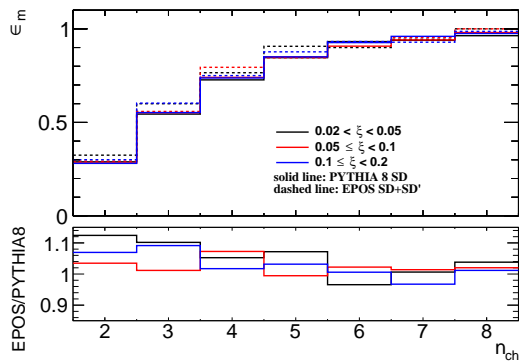


Figure 7.2: Comparison of  $\epsilon_m(n_{ch})$  calculated separately in three ranges of  $\xi$  using PYTHIA 8 SD and EPOS SD+SD' no-pile-up MCs. The ratios of EPOS to PYTHIA 8 predictions are shown in the bottom panel.

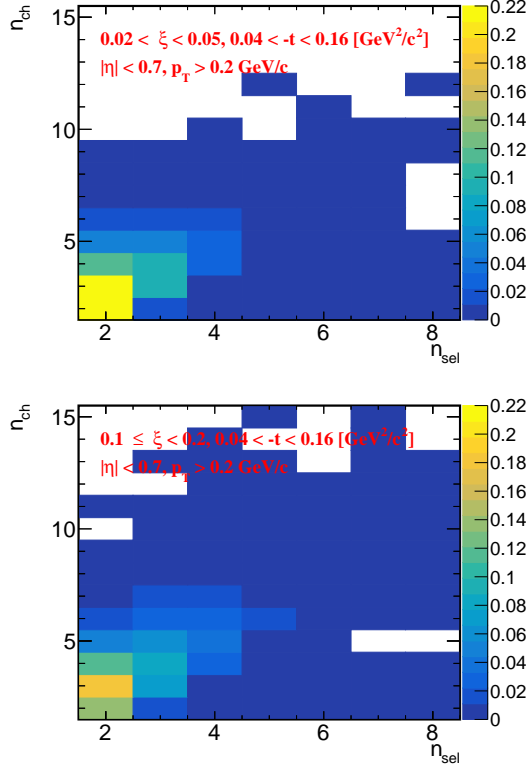


Figure 7.3: The unfolding matrices calculated from PYTHIA 8 embedding MC for three ranges of  $\xi$  separately.

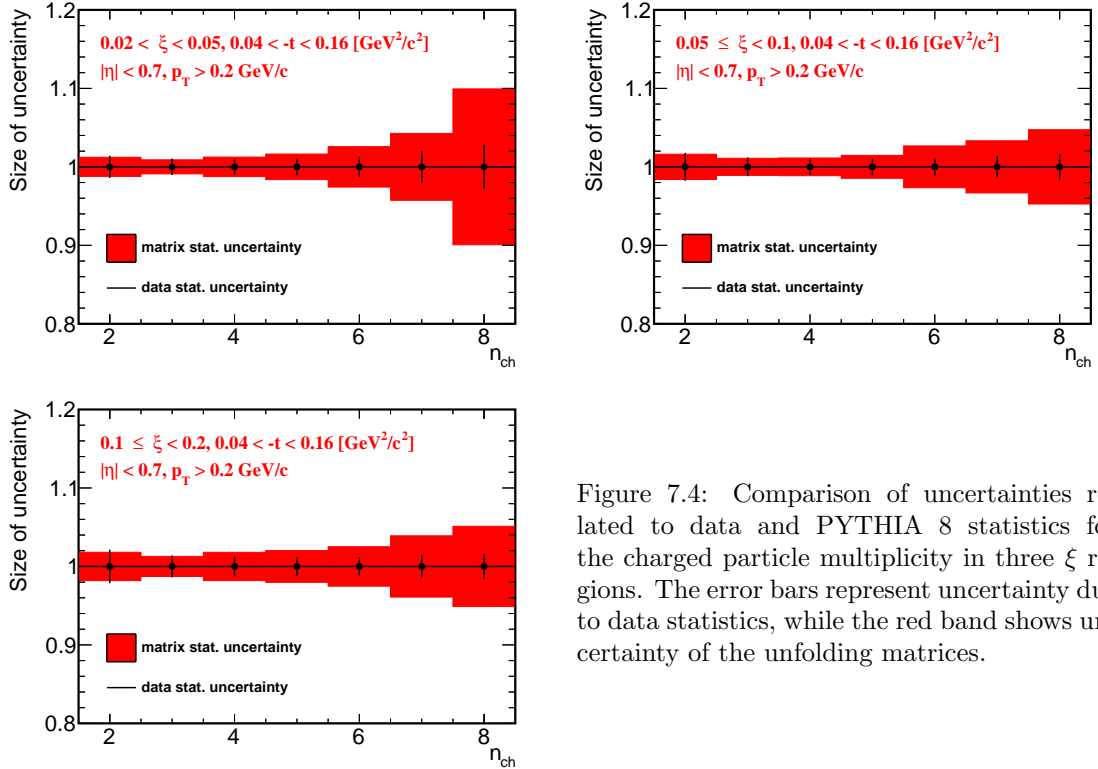


Figure 7.4: Comparison of uncertainties related to data and PYTHIA 8 statistics for the charged particle multiplicity in three  $\xi$  regions. The error bars represent uncertainty due to data statistics, while the red band shows uncertainty of the unfolding matrices.

uncertainties. It affects mainly large charged-particle multiplicities, where it is about 8 – 10% (as shown in Fig. 7.4), and is smaller or at the same level as other components contributing to the total systematic uncertainty.

The distribution  $dN/dn_{\text{ch}}$  obtained after the unfolding procedure was corrected for BBC-small efficiency, through  $w_{\text{BBC}}(n_{\text{ch}})$  weights, and migrations of events between  $\xi$  ranges, through  $f_{\xi}(n_{\text{ch}})$  weights. Since the unfolding matrices contain track reconstruction efficiencies, non-primary track backgrounds, migrations of tracks into and out of the fiducial region, the weight  $w_{\text{trk}}(p_{\text{T}}, \eta, V_z)$  was not used.

Finally, the  $dN/dn_{\text{ch}}$  distribution was normalized to the total number of events,  $N_{\text{ev}} = N$ , which was calculated as the integral of the unfolded distribution.

## 7.2 Correction to Transverse Momentum and Pseudorapidity Distributions

First the accidental and non-SD backgrounds were subtracted from the  $p_{\text{T}}$  and  $\bar{\eta}$  distributions. Next, each event was corrected for vertex reconstruction efficiency by applying  $w_{\text{ev}}^{\text{vrt}}(n_{\text{vrt}}^{\text{global}}, |\Delta z_0|)$  weights. Then, the tracks were corrected for the track reconstruction efficiency, non-primary track background contribution, track and  $\xi$  migrations, BBC-small efficiency (the product of  $w_{\text{trk}}(p_{\text{T}}, \eta, V_z)$ ,  $f_{\xi}$  and  $w_{\text{BBC}}$  weights was applied,  $f_{\xi}$  and  $w_{\text{BBC}}$  were calculated as a function of true-level  $p_{\text{T}}$  and  $\bar{\eta}$  separately).

In order to obtain charged-particle densities, the  $p_{\text{T}}$  and  $\bar{\eta}$  distributions were normalized to unity and scaled by the average charged particle multiplicity in an event  $\langle n_{\text{ch}} \rangle$ . The latter was calculated from the corrected charged particle multiplicity distribution  $dN/dn_{\text{ch}}$  (Sec. 7.1). The above procedure was done to correct the data also for events that are lost due to  $n_{\text{sel}} < 2$  but  $n_{\text{ch}} \geq 2$  since such correction was not included in any event-by-event and track-by-track weights. There was an assumption that  $p_{\text{T}}$  and  $\eta$  distributions are the same for lost and measured events, but it

708 was validated by the closure tests (Sec. 7.3). The mean  $p_T$  and  $\bar{\eta}$  in an event,  $\langle p_T \rangle$  and  $\langle \bar{\eta} \rangle$ , were  
709 obtained from the measured distributions.

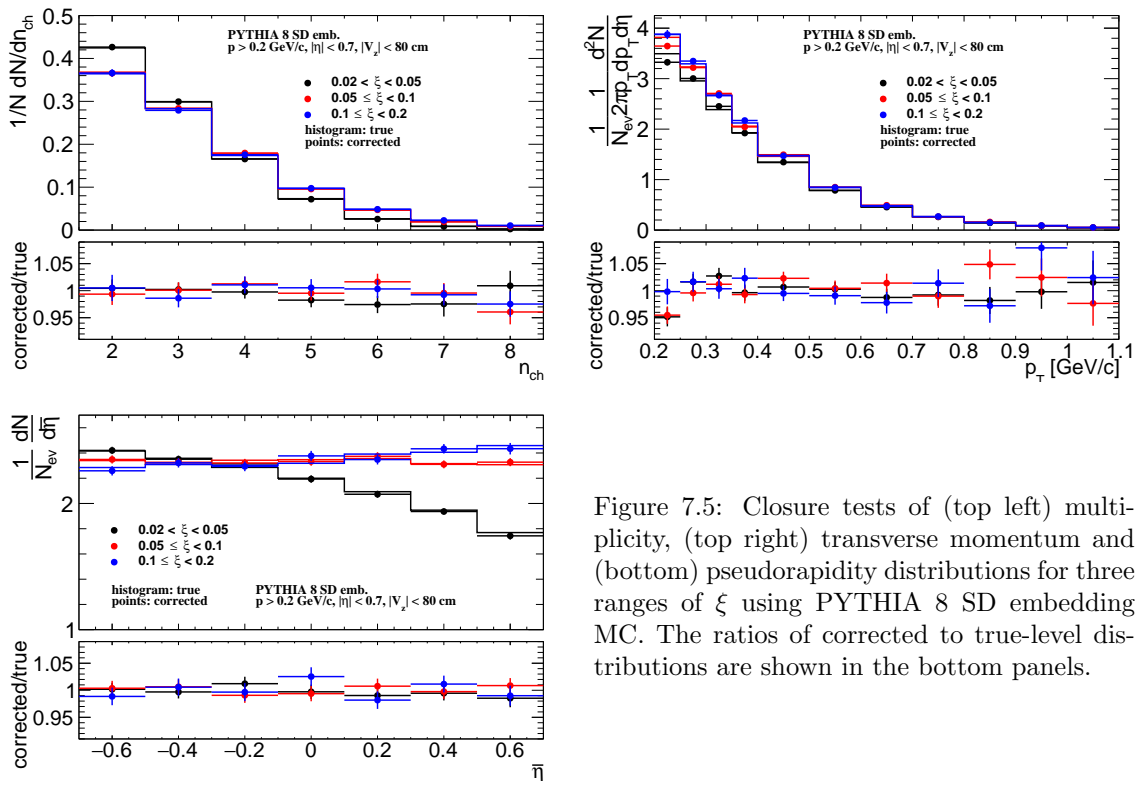
### 710 7.3 Closure Tests

711 In order to validate the correction procedures, closure tests were performed, i.e. full correction  
712 procedure was applied to the MC detector-level distributions and the results were directly com-  
713 pared to the true-level distributions. Figure 7.5 shows closure tests of multiplicity, transverse  
714 momentum and pseudorapidity distributions for three ranges of  $\xi$ , separately. PYTHIA 8 SD  
715 embedding MC was used as an input. In order to compare corrected and true-level distributions,  
716 the statistical uncertainties of the true-level distributions were assumed to be 0. The difference  
717 between true-level and corrected distributions was taken as a systematic uncertainties.

### 718 7.4 EAST-WEST asymmetry

719 Another kind of consistency check can be performed by comparing the results obtained by tag-  
720 ging forward-scattered protons in different detectors. Therefore, each distribution was measured  
721 separately for events in which forward-scattered proton is on one and the other side of the IP  
722 (east-west). Figure 7.6 shows the tests of multiplicity, transverse momentum and pseudorapidity  
723 distributions for three ranges of  $\xi$ , separately. Both statistical uncertainty components, due to  
724 input data and due to unfolding matrix, are added in quadrature for  $n_{ch}$  distributions. The largest  
725 difference is observed for charged-particle multiplicity distributions, where it varies up to 20% for  
726  $n_{ch} = 8$  and  $0.02 < \xi < 0.1$ . For the rest multiplicities and  $\xi$  ranges, the differences are smaller  
727 (< 10%). In case of  $p_T$  and  $\bar{\eta}$  distributions, a level of these disagreements is below 5%.

728 The deviations between the distributions for events with forward-scattered proton on east and  
729 west side of the IP were fitted with a constant (Fig. 7.6). The quality of the fit shows that the  
730 disagreements are compatible with statistical fluctuations ( $\chi^2/ndf$  close to 1) for multiplicity and  
731 transverse momentum distributions. For pseudorapidity, the  $\chi^2/ndf$  is significantly larger than 1.



750 Figure 7.5: Closure tests of (top left) multi-  
751 plicity, (top right) transverse momentum and  
752 (bottom) pseudorapidity distributions for three  
753 ranges of  $\xi$  using PYTHIA 8 SD embedding  
754 MC. The ratios of corrected to true-level dis-  
755 tributions are shown in the bottom panels.

732 Therefore, half of the differences between east and west distributions were used to be systematic  
 733 uncertainty for  $\bar{\eta}$  distributions.

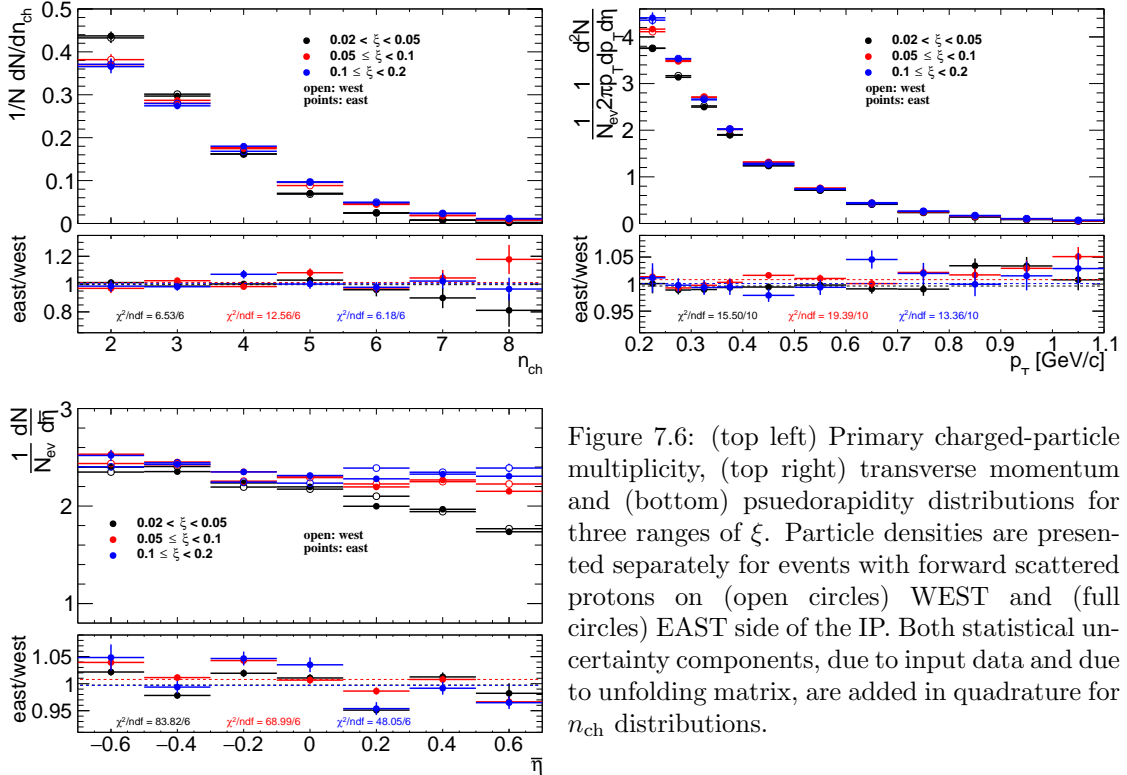


Figure 7.6: (top left) Primary charged-particle multiplicity, (top right) transverse momentum and (bottom) psuedorapidity distributions for three ranges of  $\xi$ . Particle densities are presented separately for events with forward scattered protons on (open circles) WEST and (full circles) EAST side of the IP. Both statistical uncertainty components, due to input data and due to unfolding matrix, are added in quadrature for  $n_{ch}$  distributions.

## 7.5 Particle Identification

734 Specific ionization energy loss, the  $dE/dx$ , is a function of the magnitude of a particle momentum.  
 735 In this section the particle identification with help of  $dE/dx$  is described. Due to a low particle  
 736 multiplicity and lack of signal in VPDs on the outgoing proton side (presence of the rapidity  
 737 gap) in SD events, the time of collision is not defined precisely enough, therefore, the particle  
 738 identification by the TOF is not possible and the analysis was limited to identification only by  
 739  $dE/dx$ .  
 740

741 The ionization energy loss of charged particles in material is given by the Bethe-Bloch formula  
 742 and for the STAR TPC by the more precise Bichsel formula [16]. The particle type can be  
 743 determined by comparison of particle's  $dE/dx$  with the Bethe-Bloch (Bichsel) expectations. Figure  
 744 7.7 shows the  $dE/dx$  versus rigidity  $q \times p$  for particles in  $|\eta| < 0.7$ . Particles are well separated at  
 745 low  $|q \times p|$ , whereas at higher  $|q \times p|$  the  $dE/dx$  of different particle species starts to overlap:  $e^\pm$   
 746 and  $K^\pm$  merge at  $\sim 0.4$  GeV/c,  $K^\pm$  and  $\pi^\pm$  merge at  $\sim 0.65$  GeV/c, and  $p(\bar{p})$  and  $\pi^\pm$  merge at  
 747  $\sim 1$  GeV/c. Since the  $dE/dx$  distribution for a given particle type is not Gaussian, the following  
 748 variable for each particle type was defined:

$$n\sigma_{dE/dx}^i = \ln \left( \frac{dE/dx}{(dE/dx)_i^{\text{BB}}} \right) / \sigma \quad (7.10)$$

749 where  $(dE/dx)_i^{\text{BB}}$  is the Bethe-Bloch (Bichsel) expectation of  $dE/dx$  for the given particle type  
 750  $i$  ( $i = \pi, K, p$ ),  $\sigma$  - the relative  $dE/dx$  resolution. The expected value of  $n\sigma_{dE/dx}^i$  for the particle  
 751 under consideration is 0 and the width equals to 1. The sample  $n\sigma_{dE/dx}^i$  distribution for  $\pi^\pm$ ,  $K^\pm$   
 752 and  $p(\bar{p})$  in one  $\xi$  range,  $0.02 < \xi < 0.05$ , is shown in Fig. 7.8.

753 Figure 7.9 shows the  $n\sigma_{dE/dx}^{\pi^\pm}$ ,  $n\sigma_{dE/dx}^{K^\pm}$  and  $n\sigma_{dE/dx}^{p(\bar{p})}$  distributions for  $0.6 < p_T < 0.65$  GeV/c in  
 754 the  $\xi$  range,  $0.02 < \xi < 0.05$ , each corrected for the energy loss (mass of  $i$ -particle was assumed) [1]  
 755 and vertexing (other  $p_T$  bins are shown in Appendix B). To extract the particle yield for a given  
 756 particle type, a multi-Gaussian fit is applied to the  $n\sigma_{dE/dx}^i$  distribution in each  $p_T$  bin and  $\xi$  range.  
 757 The parameters of the multi-Gaussian fit are the centroids  $\mu_{i^-/i^+}$ , widths  $\sigma_{i^-/i^+}$ , sums and ratios of  
 758 yields  $C_{i^-/i^+}$ ,  $r_{i^-/i^+}$  for negative  $i^-$  and positive  $i^+$  particles ( $\pi^\pm$ ,  $e^\pm$ ,  $K^\pm$ ,  $p$  and  $\bar{p}$ ). The positive  
 759 and negative particle  $n\sigma_{dE/dx}^i$ -distributions are fitted simultaneously, where the centroids and  
 760 widths are kept the same for particle and antiparticle. In some  $p_T$  regions, the fit does not  
 761 converge, because different particle species are not well separated there. Therefore, multiple steps  
 762 of the fitting procedure are performed to reduce the number of free parameters in the final fit  
 763 and ensure its stability. Almost all centroids and widths are constrained by a function with free  
 764 parameters  $p_k$ , where  $k \in \mathbb{N}$ . The function is chosen to describe the data as best as possible. Since  
 765  $dE/dx$  is a function of the particle's momentum and its shape should be independent of the process  
 766 under study, the values of  $p_k$  are obtained only for events with  $0.02 < \xi < 0.05$  and kept the same  
 767 for other  $\xi$  ranges. The electron parameters are limited based on the difference between data and  
 768 MC. Their contributions are fitted only in the first analysed  $p_T$  range, separately for each particle  
 769 species and  $\xi$  range. For higher  $p_T$  ranges, they are estimated from PYTHIA 8 embedding MC,  
 770 and scaled according to the ratio of PYTHIA 8 predictions and contributions fitted in the first  $p_T$   
 771 bin. The procedure slightly differs for different particle types. In each step, the multi-Gaussian fit  
 772 is performed first, then the widths and centroids are fitted in  $p_T$  ranges in which the fit applied to  
 773  $n\sigma_{dE/dx}^i$  converges. Later, the widths and centroids are extrapolated to other  $p_T$  ranges, in which  
 774 particle species are not well separated:

775 1.  $\pi^\pm$ :

776 • Step 1 (Fig. 7.10):

- 777 – Analyze data with  $0.2 < p_T < 0.65$  GeV/c
- 778 – Fit  $\mu_{\pi^-/\pi^+}$  and  $\sigma_{\pi^-/\pi^+}$  as a function of  $p_T$  with a polynomial  $p_0 p_T^3 + p_1 p_T^2 + p_2 p_T + p_3$
- 779 – Fit  $r_{e^-/e^+}$  as a function of  $p_T$  with a polynomial  $p_0 p_T^2 + p_1 p_T + p_2$
- 780 – Fit  $C_{e^-/e^+}$ ,  $\mu_{K^-/K^+}$  as a functions of  $p_T$  with  $p_0 \exp(p_1 p_T) + p_2$
- 781 – Fit  $\mu_{e^-/e^+}$  as a function of  $p_T$  with  $p_0 \exp[-(p_1 p_T)^{p_2}]$
- 782 – Fit  $\sigma_{K^-/K^+}$  as a function of  $p_T$ , for  $0.3 < p_T < 0.5$  GeV/c, with constant  $p_0$

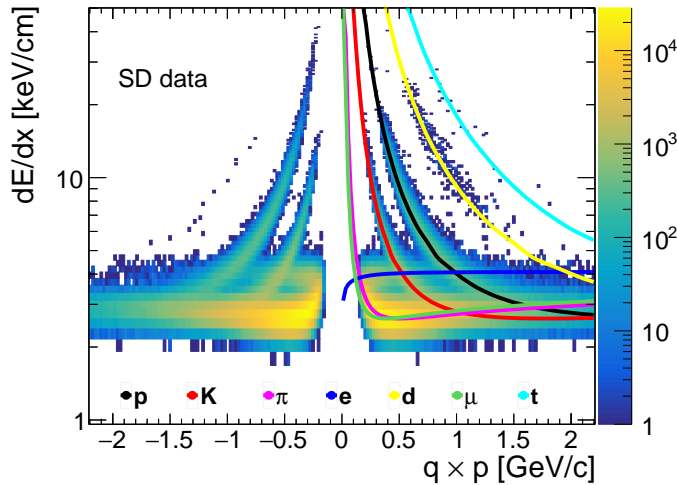


Figure 7.7: Specific ionization energy loss  $dE/dx$  as a function of rigidity  $q \times p$  for particles in  $|\eta| < 0.7$ . The Bichsel predictions for each particle species are also shown.

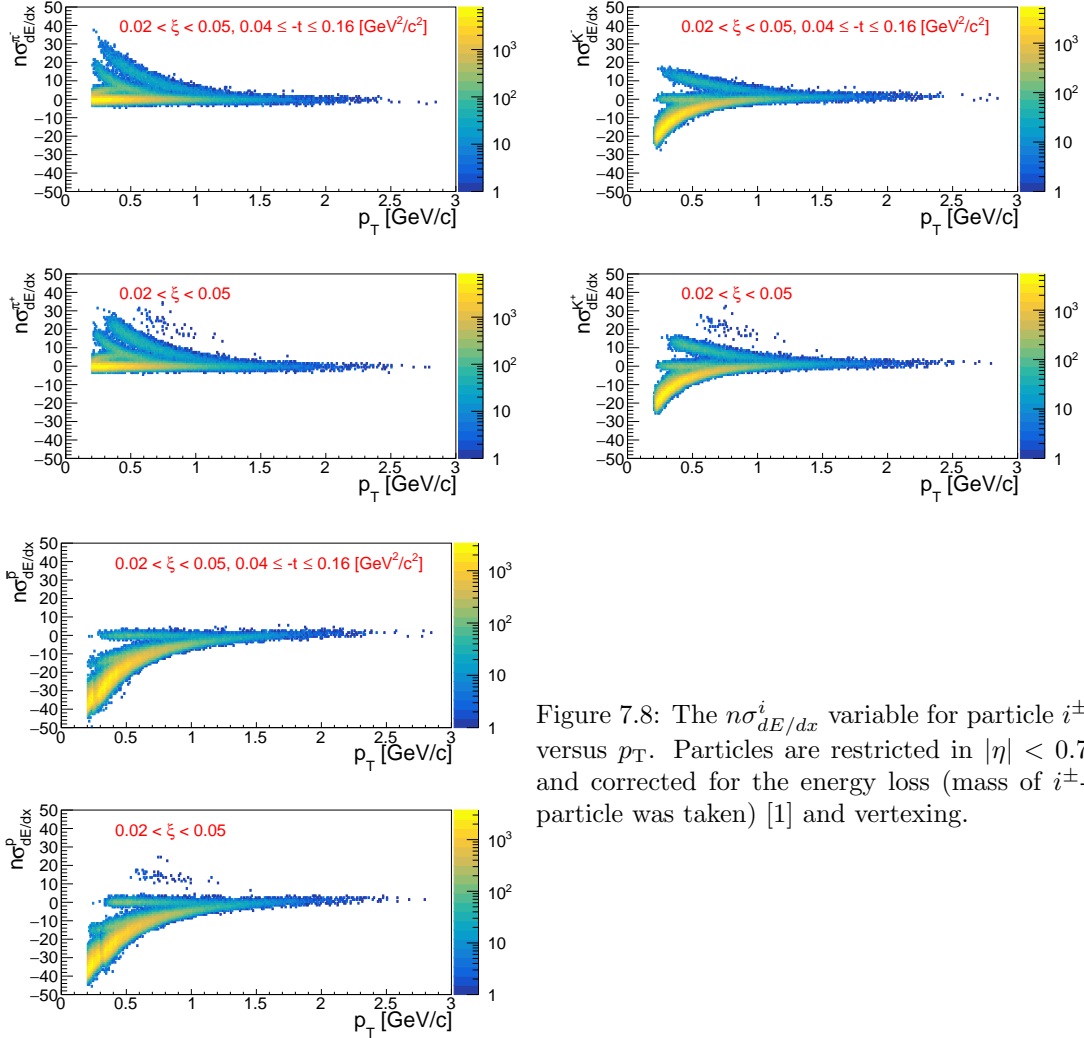


Figure 7.8: The  $n\sigma_{dE/dx}^i$  variable for particle  $i^\pm$  versus  $p_T$ . Particles are restricted in  $|\eta| < 0.7$  and corrected for the energy loss (mass of  $i^\pm$ -particle was taken) [1] and vertexing.

- 783           – Fit  $\mu_{\bar{p}/p}$  and  $\sigma_{\bar{p}/p}$  as a function of  $p_T$  with  $p_0 \exp(p_1 p_T)$
- 784     • Step 2:
- 785           –  $\sigma_{e^-/e^+}$  fixed to 1.2 and 0.8 for  $0.2 < p_T < 0.4$  and  $0.4 < p_T < 0.7$ , respectively
- 786           – Fit  $\sigma_{K^-/K^+}$  as a function of  $p_T$ , for  $0.3 < p_T < 0.7$  GeV/c, with constant  $p_0$  and fix it to the value of  $p_0$
- 787           – The rest parameters from Step 1 are fixed to the values calculated from functions obtained in Step 1:  $\mu_{\pi^-/\pi^+}$ ,  $\sigma_{\pi^-/\pi^+}$ ,  $r_{e^-/e^+}$ ,  $C_{e^-/e^+}$ ,  $\mu_{e^-/e^+}$ ,  $\mu_{K^-/K^+}$ ,  $\mu_{\bar{p}/p}$ ,  $\sigma_{\bar{p}/p}$

790     2.  $K^\pm$ :

- 791     • Step 1 (Fig. 7.11):
- 792           – Analyze data with  $0.2 < p_T < 0.6$  GeV/c
- 793           – Fit  $\mu_{\pi^-/\pi^+}$  as a function of  $p_T$  with  $-\exp(p_0 + p_1 p_T)$
- 794           – Fit  $\sigma_{\pi^-/\pi^+}$ ,  $C_{e^-/e^+}$ ,  $\sigma_{e^-/e^+}$ ,  $\sigma_{K^-/K^+}$  as a function of  $p_T$  with  $\exp(p_0 + p_1 p_T)$
- 795           – Fit  $r_{e^-/e^+}$  as a function of  $p_T$  with constant  $p_0$
- 796           – Fit  $\mu_{e^-/e^+}$  as a function of  $p_T$  with a polynomial  $p_0 p_T^3 + p_1 p_T^2 + p_2 p_T + p_3$

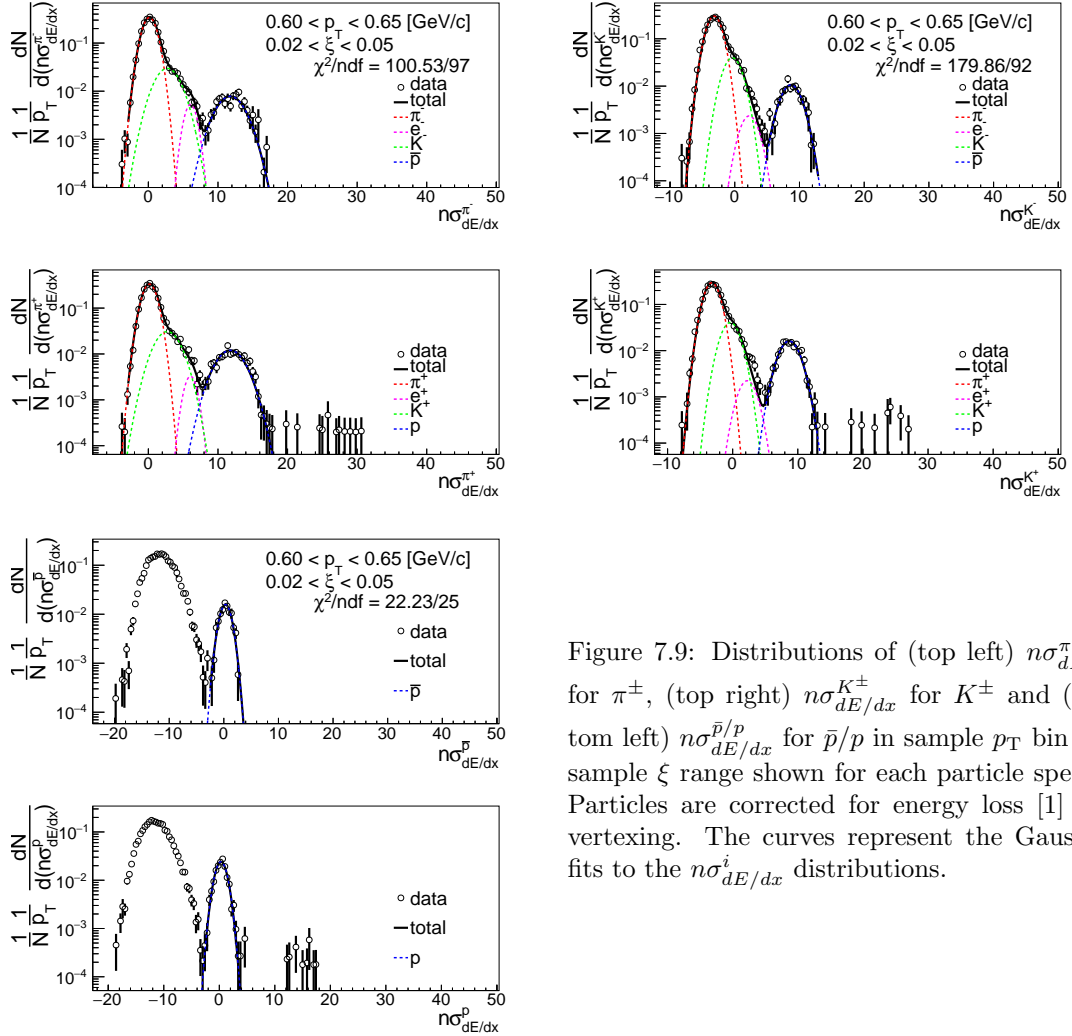


Figure 7.9: Distributions of (top left)  $n\sigma_{dE/dx}^{\pi^\pm}$  for  $\pi^\pm$ , (top right)  $n\sigma_{dE/dx}^{K^\pm}$  for  $K^\pm$  and (bottom left)  $n\sigma_{dE/dx}^{\bar{p}/p}$  for  $\bar{p}/p$  in sample  $p_T$  bin and sample  $\xi$  range shown for each particle species. Particles are corrected for energy loss [1] and vertexing. The curves represent the Gaussian fits to the  $n\sigma_{dE/dx}^i$  distributions.

- 798           – Fit  $\mu_{K^-/K^+}$  as a function of  $p_T$  with a polynomial  $p_0 + p_1 p_T^2$
- 799           • Step 2:
- 800           – All parameters from Step 1 except  $\sigma_{e^-/e^+}$  are fixed to the values calculated from
- 801           functions obtained in Step 1
- 802           – Fit  $\sigma_{e^-/e^+}$  as a function of  $p_T$ , for  $0.45 < p_T < 0.65 \text{ GeV/c}$ , with constant  $p_0$
- 803           • Step 3:
- 804           –  $\sigma_{e^-/e^+}$  fixed to the values calculated from functions obtained in Steps 1 and 2 for
- 805            $0.3 < p_T < 0.45$  and  $0.45 < p_T < 0.65$ , respectively.
- 806           – The rest parameters from Step 1 are fixed to the values calculated from functions
- 807           obtained in Step 1:  $\mu_{\pi^-/\pi^+}$ ,  $\sigma_{\pi^-/\pi^+}$ ,  $r_{e^-/e^+}$ ,  $C_{e^-/e^+}$ ,  $\mu_{e^-/e^+}$ ,  $\mu_{K^-/K^+}$ ,  $\sigma_{K^-/K^+}$

### 808       3. $\bar{p}, p$ :

- 809           • Step 1 (Fig. 7.12):
- 810           – Analyze data with  $0.4 < p_T < 0.9 \text{ GeV/c}$
- 811           – Fit  $\mu_{\pi^-/\pi^+}$ ,  $\mu_{K^-/K^+}$  as a function of  $p_T$  with a polynomial  $p_0 p_T + p_1$

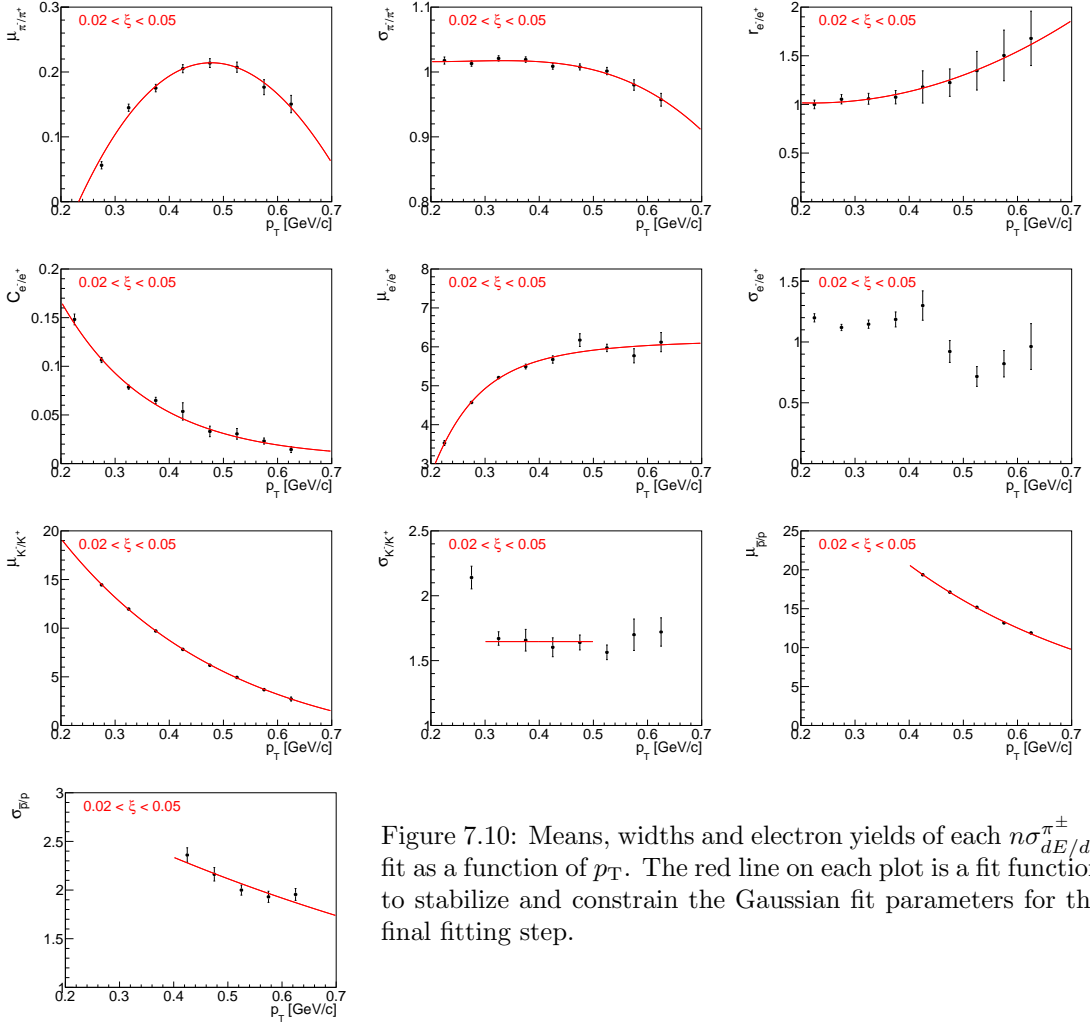


Figure 7.10: Means, widths and electron yields of each  $n\sigma_{dE/dx}^{\pi^\pm}$  fit as a function of  $p_T$ . The red line on each plot is a fit function to stabilize and constrain the Gaussian fit parameters for the final fitting step.

- 812     – Fit  $\sigma_{\pi^-/\pi^+}$  as a function of  $p_T$  with a polynomial  $p_0 p_T^2 + p_1 p_T + p_2$
- 813     – Fit  $\sigma_{K^-/K^+}$  as a function of  $p_T$  with  $\exp(p_0 + p_1 p_T)$
- 814     • Step 2:
  - 815       –  $\mu_{K^-/K^+}$  fixed to the values calculated from a function obtained in Step 1
  - 816       – All the rest parameters from Step 1 are limited to the values calculated from functions obtained in Step 1
  - 817       – Fit  $\mu_{\pi^-/\pi^+}$ ,  $\sigma_{\pi^-/\pi^+}$ ,  $\sigma_{K^-/K^+}$  as a function of  $p_T$  with a polynomial  $p_0 p_T^2 + p_1 p_T + p_2$
  - 818       – Fit  $\mu_{\bar{p}/p}$  as a function of  $p_T$ , for  $0.7 < p_T < 1.0$  GeV/c, with constant  $p_0$
- 820     • Step 3:
  - 821       –  $\mu_{K^-/K^+}$  fixed to the values calculated from a function obtained in Step 1
  - 822       –  $\mu_{\bar{p}/p}$  fixed to the values calculated from a function obtained in Step 2 for  $0.7 < p_T < 1.0$
  - 823       – The rest parameters from Step 2 are fixed to the values calculated from functions obtained in Step 2:  $\mu_{\pi^-/\pi^+}$ ,  $\sigma_{\pi^-/\pi^+}$ ,  $\sigma_{K^-/K^+}$

826     The particle yield is extracted from the fit to the corresponding  $n\sigma_{dE/dx}^i$  distribution (corrected  
827     only for the energy loss and vertexing). As shown in Fig. 7.8, the  $dE/dx$  of each particle type merge

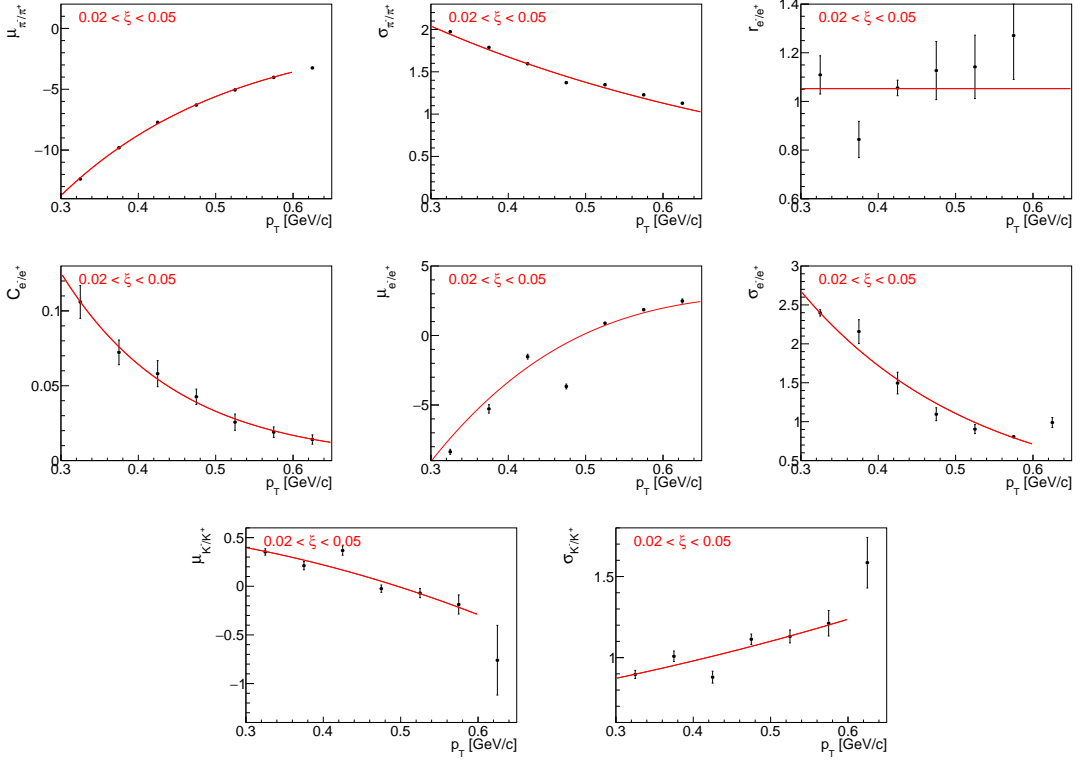


Figure 7.11: Means, widths and electron yields of each  $n\sigma_{dE/dx}^{K^\pm}$  fit as a function of  $p_T$ . The red line on each plot is a fit function to stabilize and constrain the Gaussian fit parameters for the final fitting step.

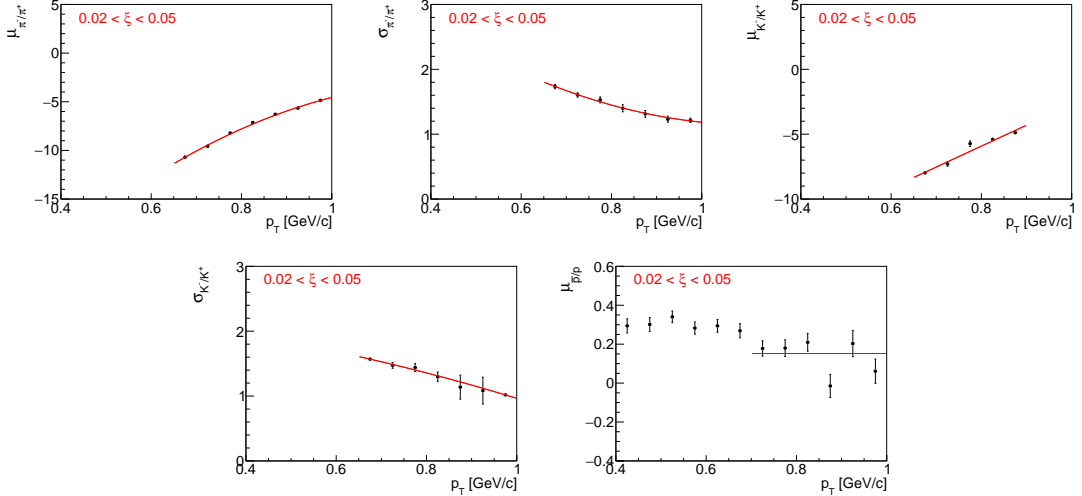


Figure 7.12: Means and widths of each  $n\sigma_{dE/dx}^{\bar{p}/p}$  fit as a function of  $p_T$ . The red line on each plot is a fit function to stabilize and constrain the Gaussian fit parameters for the final fitting step.

at large  $p_T$ . Hence, the particle identification is limited. Pions can be identified in the momentum range of  $0.2 - 0.7$  GeV/c, kaons in  $0.3 - 0.65$  GeV/c and (anti)protons in  $0.4 - 1.0$  GeV/c.

## 830 7.6 Antiparticle-to-Particle Ratios

831 The following steps were taken to correct the identified antiparticle to particle (pion, kaon, proton  
 832 and their antiparticle) multiplicity ratios as a function of  $p_T$  in three ranges of  $\xi$ :

- 833 • The raw identified particle yields were obtained through multi-Gaussian fits to the  $n\sigma_{dE/dx}^i$   
 834 distributions (Sec. 7.5), where the vertex reconstruction and energy loss corrections [1] were  
 835 applied. The latter depends on the particle type.
- 836 • The non-SD background (Sec. 4.2) is the same for particles and antiparticles, thus, it was  
 837 not subtracted. The accidental background contribution (Sec. 4) is very small, hence, any  
 838 particle-antiparticle differences have a negligible effect on the result. Therefore, it was as-  
 839 sumed that the accidental background does not depend on the particle type and for this  
 840 reason it was not subtracted.
- 841 • The particle yields were corrected for track reconstruction efficiencies [1], which depend on  
 842 the particle type and charge. These corrections are averaged over  $\eta$  and  $V_z$ . The ratio of  
 843 particle to antiparticle TPC-TOF efficiencies is shown in Fig. 7.13. It weakly depends on  $\xi$   
 844 range, therefore, only sample results for single range of  $0.02 < \xi < 0.05$  are presented.
- 845 • The background from non-primary tracks was subtracted (Sec. 4.1):
  - 846 –  $\pi^\pm$ : weak decays pions, muon contribution and background from detector dead-material  
   interactions,
  - 847 –  $p$ : background from detector dead-material interactions,
  - 848 –  $p, \bar{p}$ : reconstructed tracks which have the appropriate number of common hit points  
   with true-level particle, but the distance between them is too large (this background is  
   negligibly small for other particle types),
  - 849 – fake track contribution was assumed to be the same for each particle type, hence, it  
   was not subtracted.
- 850 • Since track and  $\xi$  migrations, and BBC-small efficiency, do not depend on the particle type  
 851 and charge, these corrections are not applied.
- 852 • Finally, each antiparticle  $p_T$  distribution was divided by the corresponding particle  $p_T$  dis-  
 853 tribution to obtain fully corrected identified antiparticle to particle multiplicity ratios.
- 854 • Additionally, the average antiparticle to particle ratios over fiducial region of  $p_T$  in each  $\xi$   
 855 region were calculated.

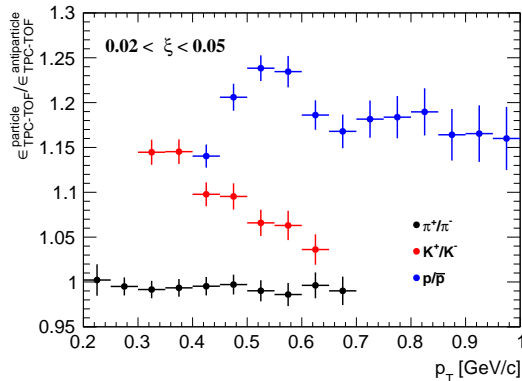


Figure 7.13: Ratio of particle to antiparticle TPC-TOF efficiencies for  $0.02 < \xi < 0.05$ .

## 8. Systematic Uncertainties

Apart from the statistical uncertainties there are also systematic uncertainties originating from inefficiencies and limitations of the measurement devices and techniques. The following sources of systematic uncertainties were considered:

- the effect of off-time pile-up on TPC track reconstruction efficiency [1],
- the uncertainty of TPC track reconstruction efficiency related to the description of dead-material in simulation [1],
- representation of data sample in embedding MC [1],
- variation in the track quality cuts [1],
- non-primary track background contribution (Sec. 4.1),
- fake track background contribution (Sec. 4.1),
- TOF system simulation accuracy [1],
- accidental background contribution (Sec. 4),
- the effect of alternative model of hadronization on BBC-small efficiency (Sec. 5.2),
- non-SD background contribution (Sec. 4.2),
- the effect of alternative model on  $\epsilon_m$  correction (Sec. 7.1),
- non-closure (Sec 7.3),
- non-closure of  $N_{\text{ev}}$ , applied only to  $p_T$  and  $\bar{\eta}$  distributions,
- difference in the distributions calculated separately for events in which forward proton is on one and the other side of the IP (east-west, Sec 7.4).

Some of the systematic uncertainties on  $1/N dN/dn_{\text{ch}}$  (related to TPC and TOF reconstruction efficiencies, fake track background contribution) are propagated by randomly removing and adding tracks in the  $n_{\text{sel}}$  distribution before unfolding procedure. For each track, a random number is generated. If this number is smaller than the absolute value of systematic uncertainty, then  $n_{\text{sel}}$  is increased or decreased, depending on the sign of systematic uncertainty.

Figures 8.1 to 8.3 show the components contributing to the total systematic uncertainty for charged particle distributions without the identification. The dominant systematic uncertainty for  $p_T$  and  $n_{\text{ch}}$  distributions is related to TOF system simulation accuracy. It affects mainly low- $p_T$  particles, where it is about 2 – 3%, and large charged particle multiplicities, where it varies up to 20% for  $n_{\text{ch}} = 8$  and  $0.02 < \xi < 0.05$ . In case of  $\bar{\eta}$  distribution, the systematic uncertainty on TOF mainly refers to charged particles produced at the edge of the fiducial region, for which it is about 2%. The largest (up to 30%) systematic uncertainty for  $\langle \bar{\eta} \rangle$ , is related to the observed difference in the distributions calculated separately with respect to the forward-scattered proton direction. The rest of the components have smaller contributions to the total systematic uncertainty. The systematic uncertainty on non-closure is on average at the level of 2% which proves the accuracy of the correction procedure.

Figures 8.4 to 8.7 show breakdown of all different systematics for the antiparticle-to-particle multiplicity ratio distributions. An additional systematic contribution for  $\bar{p}/p$  multiplicity ratio due to proton background estimation was introduced. Since most of the corrections are the same for particle and its antiparticle, nearly all systematic uncertainties cancel out in the antiparticle-to-particle ratios. The largest sources of systematics, which do not, are related to proton background estimation and dead-material effect on TPC track reconstruction efficiency. The former was found to be up to 6%, whereas the latter varies up to 2% for low- $p_T$   $\bar{p}/p$  multiplicity ratio.

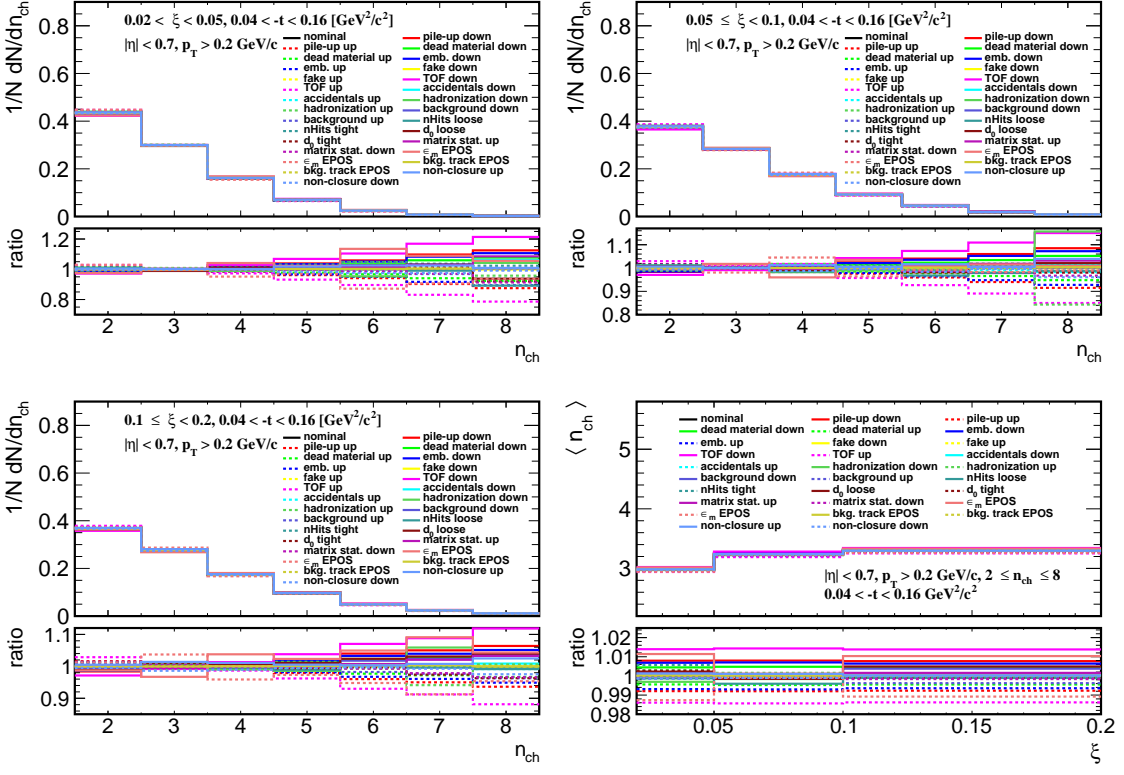


Figure 8.1: Components of the systematic uncertainties for the charged particle multiplicity in three  $\xi$  regions and for the average charged particle multiplicity.

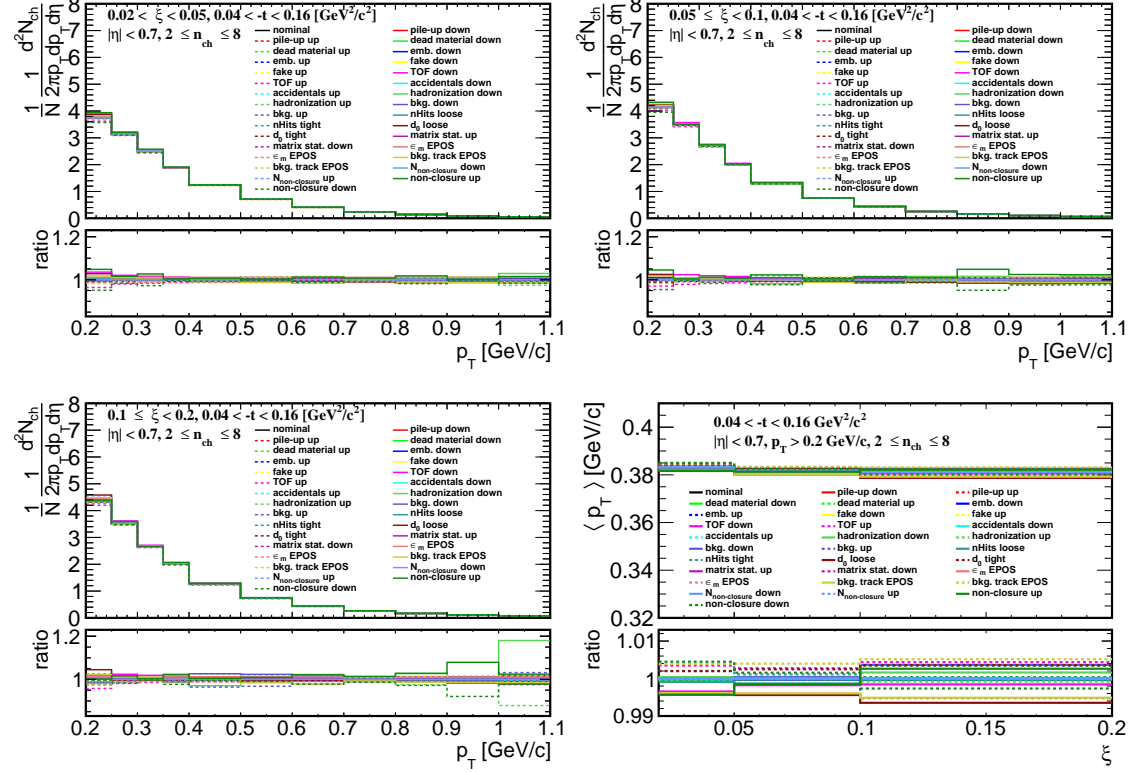


Figure 8.2: Components of the systematic uncertainties for  $p_T$  distributions in three  $\xi$  regions and for an average  $p_T$  distribution.

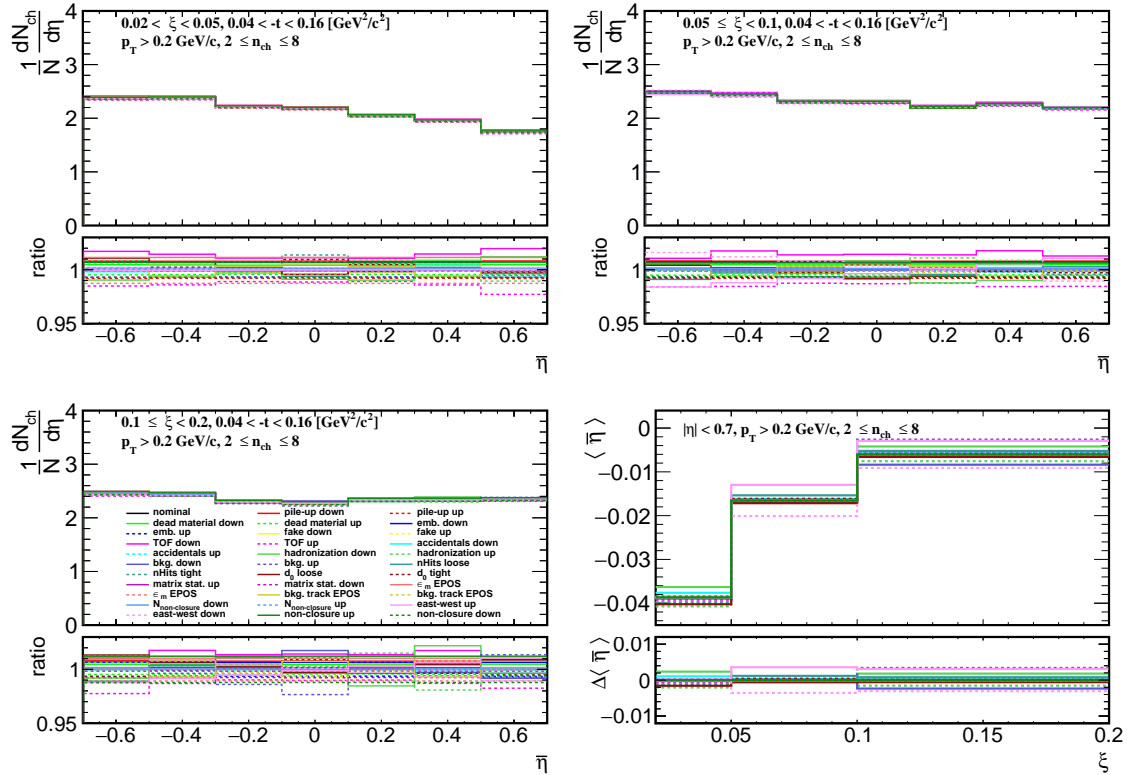


Figure 8.3: Components of the systematic uncertainties for  $\bar{\eta}$  distributions in three  $\xi$  regions and for an average  $\bar{\eta}$  distribution.

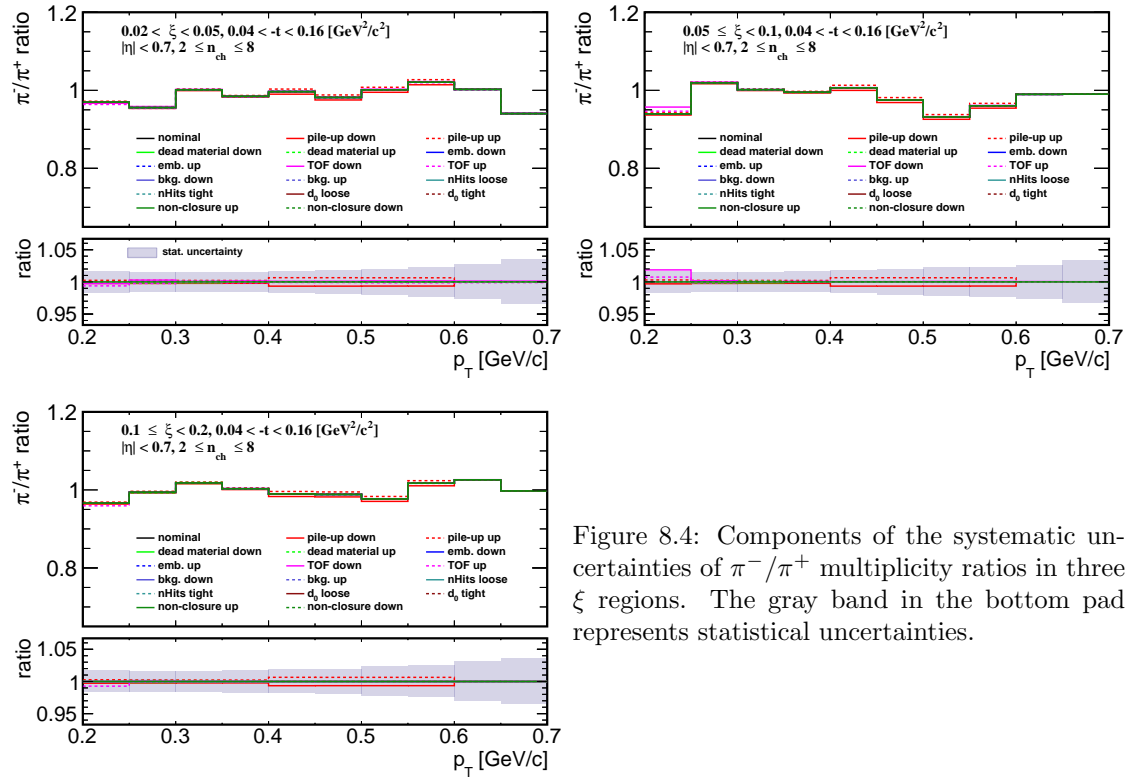


Figure 8.4: Components of the systematic uncertainties of  $\pi^-/\pi^+$  multiplicity ratios in three  $\xi$  regions. The gray band in the bottom pad represents statistical uncertainties.

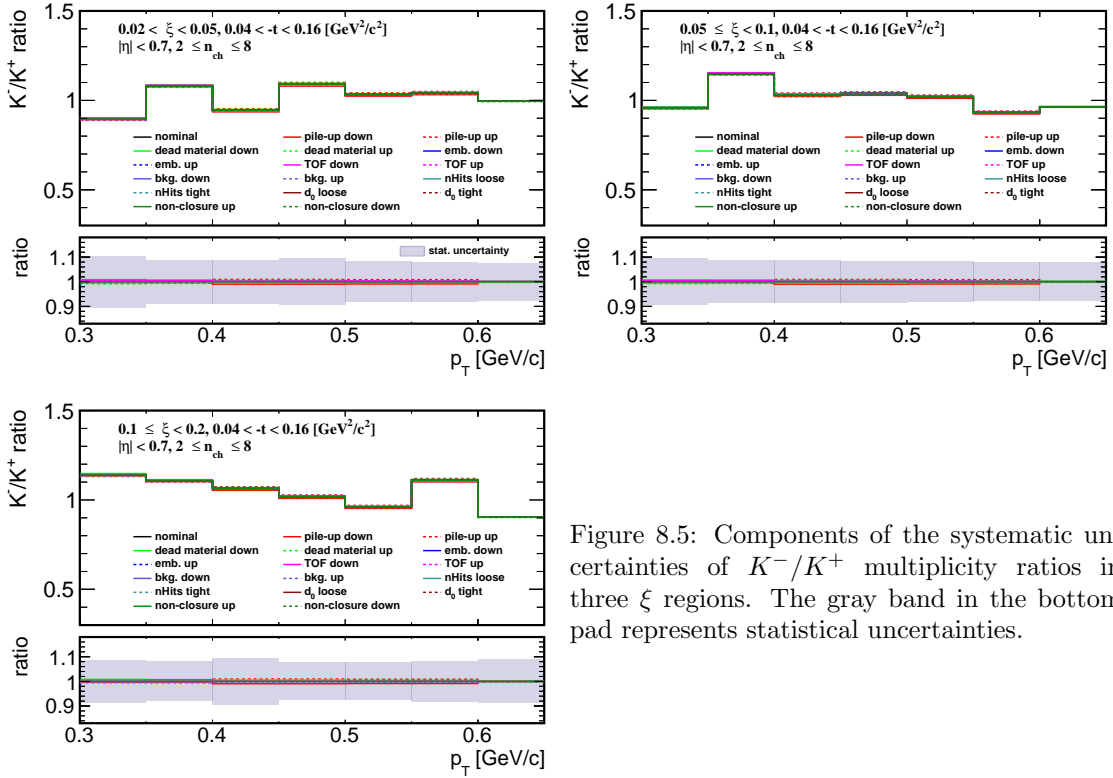


Figure 8.5: Components of the systematic uncertainties of  $K^-/K^+$  multiplicity ratios in three  $\xi$  regions. The gray band in the bottom pad represents statistical uncertainties.

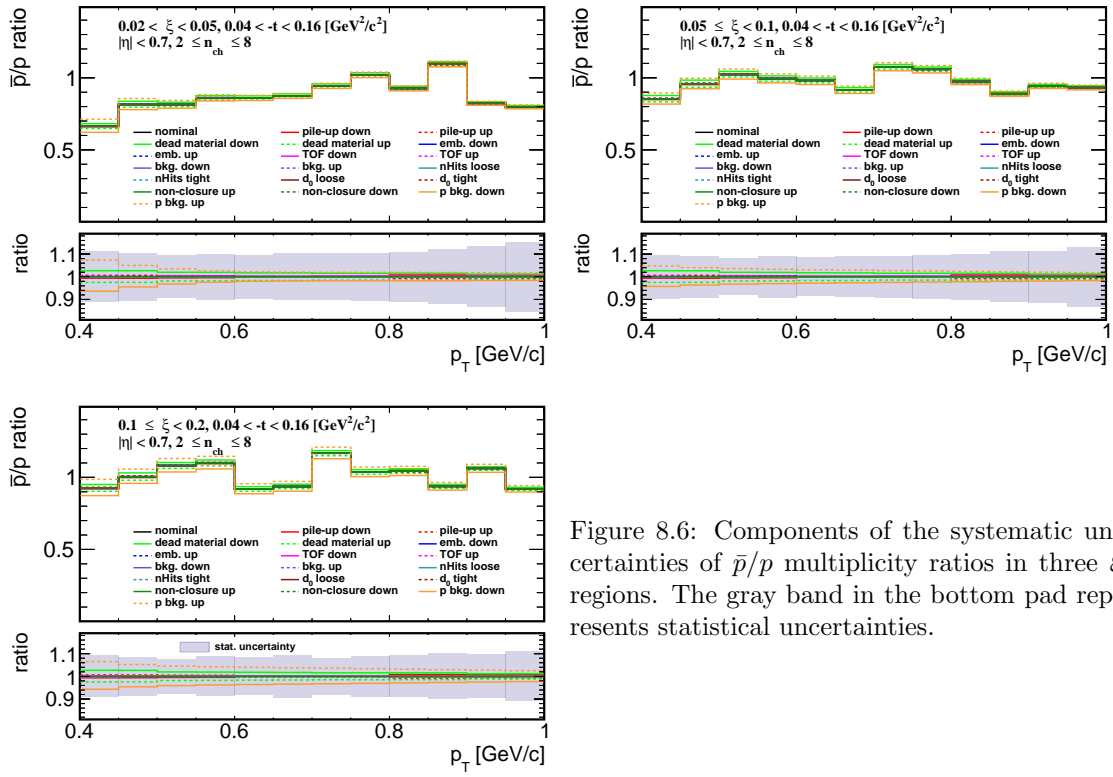


Figure 8.6: Components of the systematic uncertainties of  $\bar{p}/p$  multiplicity ratios in three  $\xi$  regions. The gray band in the bottom pad represents statistical uncertainties.

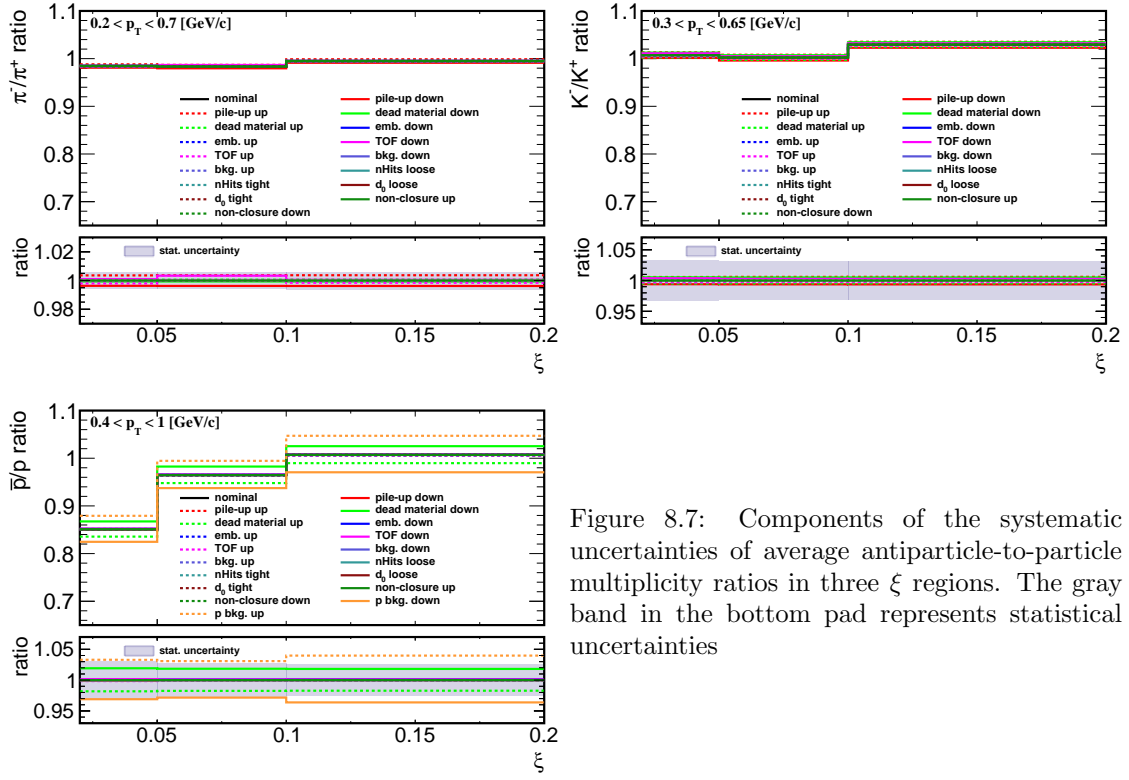


Figure 8.7: Components of the systematic uncertainties of average antiparticle-to-particle multiplicity ratios in three  $\xi$  regions. The gray band in the bottom pad represents statistical uncertainties

# 9. Results

In the following section, the final-state charged particle distributions are compared with various SD MC predictions, i.e.

- PYTHIA 8 4C (SaS),
- PYTHIA 8 A2 (MBR),
- PYTHIA 8 A2 (MBR-tuned),
- HERWIG 7,
- EPOS LHC with combined two classes of processes: diffractive (EPOS SD) and non-diffractive (EPOS SD'),
- EPOS LHC SD'.

In all figures, data are shown as solid points with error bars representing the statistical uncertainties. Gray boxes represent statistical and systematic uncertainties added in quadrature. Predictions from MC models are shown as colour histograms and markers. The lower panel in each figure shows the ratio of data to the models' predictions. All results are presented separately for three ranges of  $\xi$ :  $0.02 < \xi < 0.05$ ,  $0.05 < \xi < 0.1$ ,  $0.1 < \xi < 0.2$ .

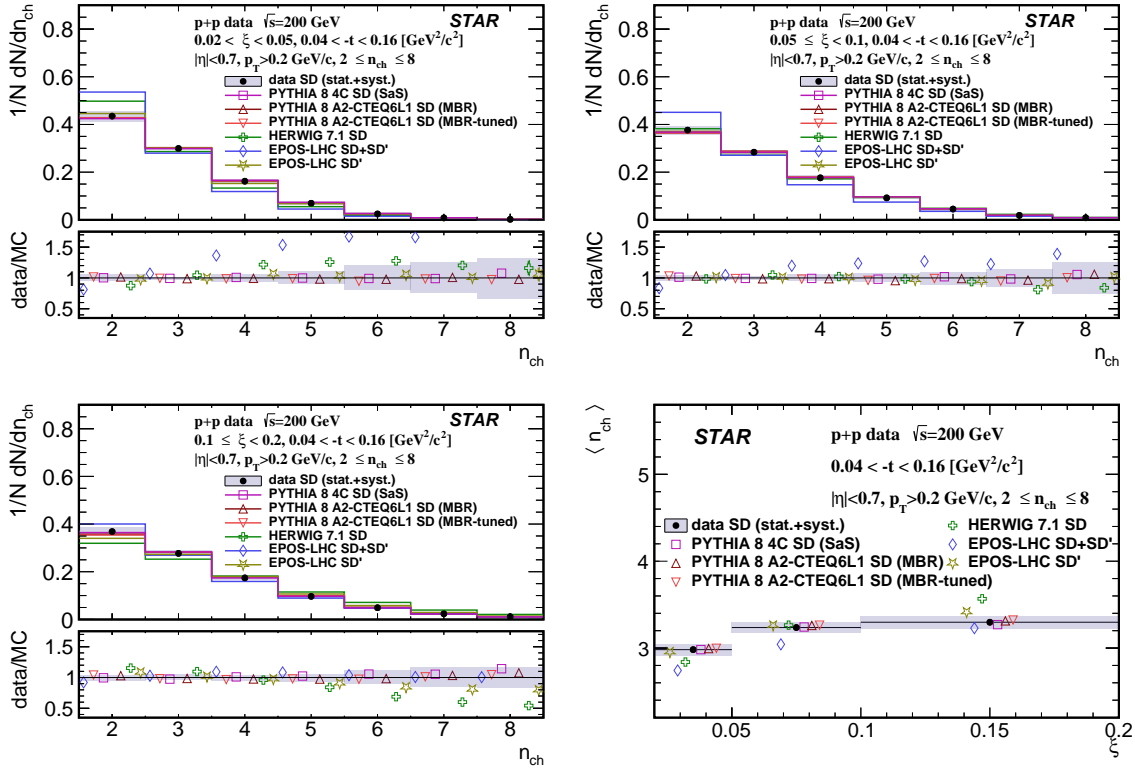


Figure 9.1: Primary charged-particle multiplicity shown separately for the three ranges of  $\xi$ : (top left)  $0.02 < \xi < 0.05$ , (top right)  $0.05 < \xi < 0.1$ , (bottom left)  $0.1 < \xi < 0.2$  and (bottom right) the mean multiplicity  $\langle n_{ch} \rangle$  as a function of  $\xi$ .

918     Figure 9.1 shows primary charged-particle multiplicity separately for the three ranges of  $\xi$  and  
 919 the mean multiplicity  $\langle n_{\text{ch}} \rangle$  as a function of  $\xi$ . Data follow the expected increase of  $\langle n_{\text{ch}} \rangle$  with  
 920  $\xi$  due to the larger diffractive masses probed by increasing  $\xi$  in SD process. The shapes of the  
 921 measured distributions are reproduced reasonably well by all models except EPOS SD+SD' and  
 922 HERWIG SD which predicts smaller  $\langle n_{\text{ch}} \rangle$  for  $0.02 < \xi < 0.1$  and  $0.02 < \xi < 0.05$ , respectively.  
 923 HERWIG SD predicts too large  $\langle n_{\text{ch}} \rangle$  for  $0.1 < \xi < 0.2$ .

924     Figure 9.2 shows primary charged-particle multiplicities as a function of  $p_T$  separately for  
 925 the three ranges of  $\xi$  and the mean transverse momentum  $\langle p_T \rangle$  as a function of  $\xi$ . Data show  
 926 that  $\langle p_T \rangle$  depends very weakly on  $\xi$ . Models describe data fairly well except HERWIG SD which  
 927 predicts much steeper dependence of particle density with  $p_T$  in all three  $\xi$  ranges.

928     Figure 9.3 shows primary charged-particle multiplicity as a function of  $\bar{\eta}$  separately for the three  
 929 ranges of  $\xi$  and the mean pseudorapidity  $\langle \bar{\eta} \rangle$  as a function of  $\xi$ . Data show expected flattening of  
 930 the  $\bar{\eta}$  distribution with increasing  $\xi$  which reflects SD event-asymmetry and fact that the gap-edge  
 931 at large  $\xi$  is outside  $|\bar{\eta}| < 0.7$  region leading to more flat distribution of particle density as a  
 932 function of  $\bar{\eta}$ . PYTHIA 8 models describe data fairly well only at  $0.02 < \xi < 0.05$  and predicts  
 933 flatter distributions for  $0.05 < \xi < 0.2$ . EPOS SD+SD' and HERWIG SD predict less and more  
 934 steep dependence of particle density with  $\bar{\eta}$  for all three  $\xi$  ranges, respectively.

935     Figure 9.4 shows the ratio of production yields of  $\pi^-/\pi^+$  as a function of  $p_T$  separately for  
 936 the three ranges of  $\xi$ . Data in all three  $\xi$  ranges are consistent with equal amounts of  $\pi^+$  and  
 937  $\pi^-$  with no significant  $p_T$  dependence. Models agree with data (except HERWIG) predicting on  
 938 average small deviation from unity by  $\sim 2\%$  what is smaller than data uncertainties. HERWIG  
 939 in first two  $\xi$  ranges predicts too large asymmetry between  $\pi^+$  and  $\pi^-$ .

940     Figure 9.5 shows the ratio of production yields of  $K^-/K^+$  as a function of  $p_T$  separately for

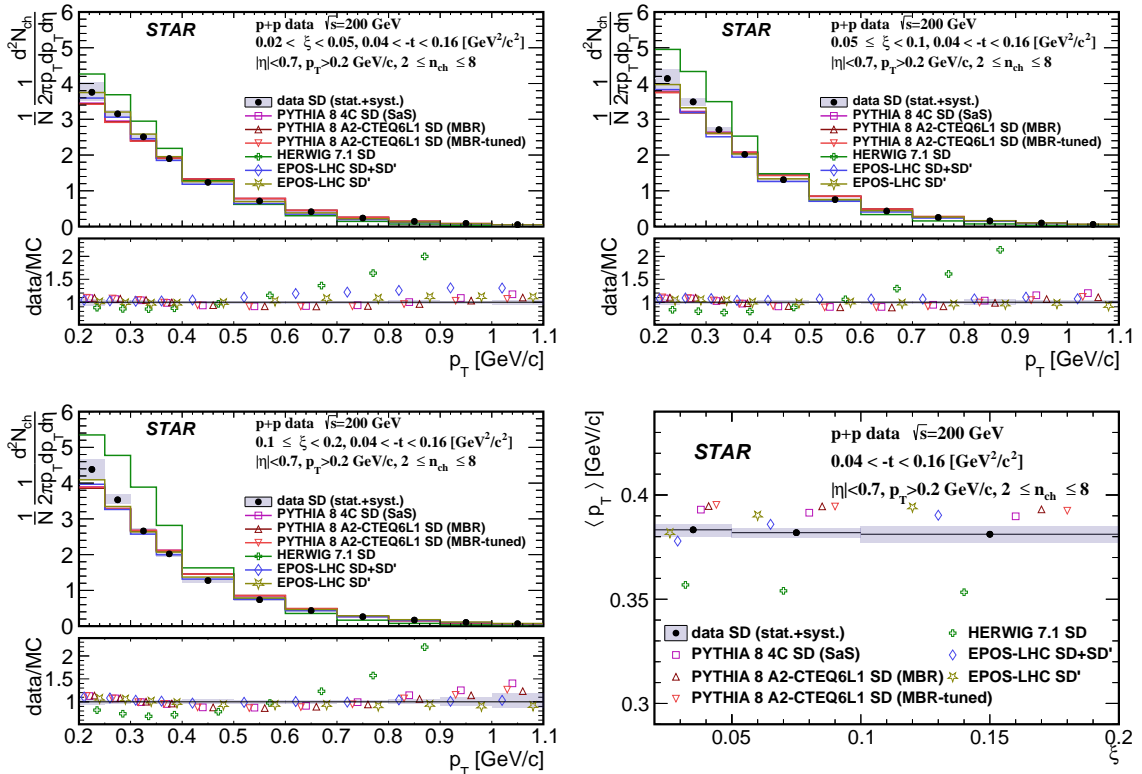


Figure 9.2: Primary charged-particle multiplicities as a function of  $p_T$  shown separately for the three ranges of  $\xi$ : (top left)  $0.02 < \xi < 0.05$ , (top right)  $0.05 < \xi < 0.1$ , (bottom left)  $0.1 < \xi < 0.2$  and (bottom right) the mean transverse momentum  $\langle p_T \rangle$  as a function of  $\xi$ .

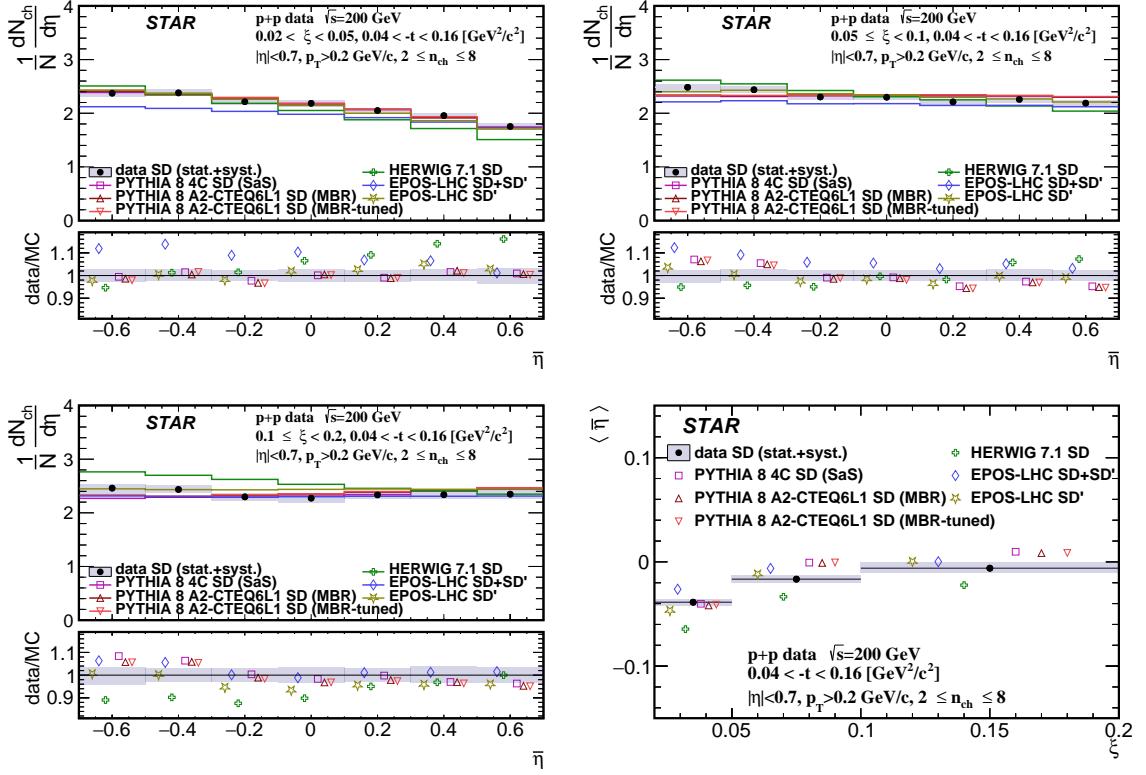


Figure 9.3: Primary charged-particle multiplicity as a function of  $\bar{\eta}$  shown separately for the three ranges of  $\xi$ : (top left)  $0.02 < \xi < 0.05$ , (top right)  $0.05 < \xi < 0.1$ , (bottom left)  $0.1 < \xi < 0.2$  and (bottom right) the mean pseudorapidity  $\langle \bar{\eta} \rangle$  as a function of  $\xi$ .

the three ranges of  $\xi$ . Data in all three  $\xi$  ranges are consistent with equal amounts of  $K^+$  and  $K^-$  with no  $p_T$  dependence. Models agree with data except HERWIG in the first  $\xi$  range predicting too large ratio of  $K^-$  to  $K^+$ .

Figure 9.6 shows the ratio of production yields of  $\bar{p}/p$  as a function of  $p_T$  separately for the three ranges of  $\xi$ . Data in the last two  $\xi$  ranges are consistent with equal amounts of  $p$  and  $\bar{p}$  with no  $p_T$  dependence. However, in the first  $\xi$  range at  $p_T < 0.7$  GeV/c data shows significant deviation from unity indicating a significant transfer of the baryon number from the forward to the central region. PYTHIA8, EPOS SD' and EPOS SD+SD' agree with data in the last two  $\xi$  ranges. In first  $\xi$  range PYTHIA8 and EPOS SD' predict small deviation from unity by  $\approx 7\%$  which is smaller than observed in data ( $\bar{p}/p = 0.85 \pm 0.04$ ), whereas EPOS SD+SD' predicts an asymmetry between  $\bar{p}$  and  $p$  of  $\sim 30\%$  which is larger than observed in data except  $p_T < 0.5$  GeV/c. HERWIG predicts much larger baryon number transfer compared to data in first two  $\xi$  ranges and shows consistency with data in last  $\xi$  range.

Figure 9.7 shows mean ratio of production yields of  $\pi^-/\pi^+$ ,  $K^-/K^+$  and  $\bar{p}/p$  as a function of  $\xi$ .

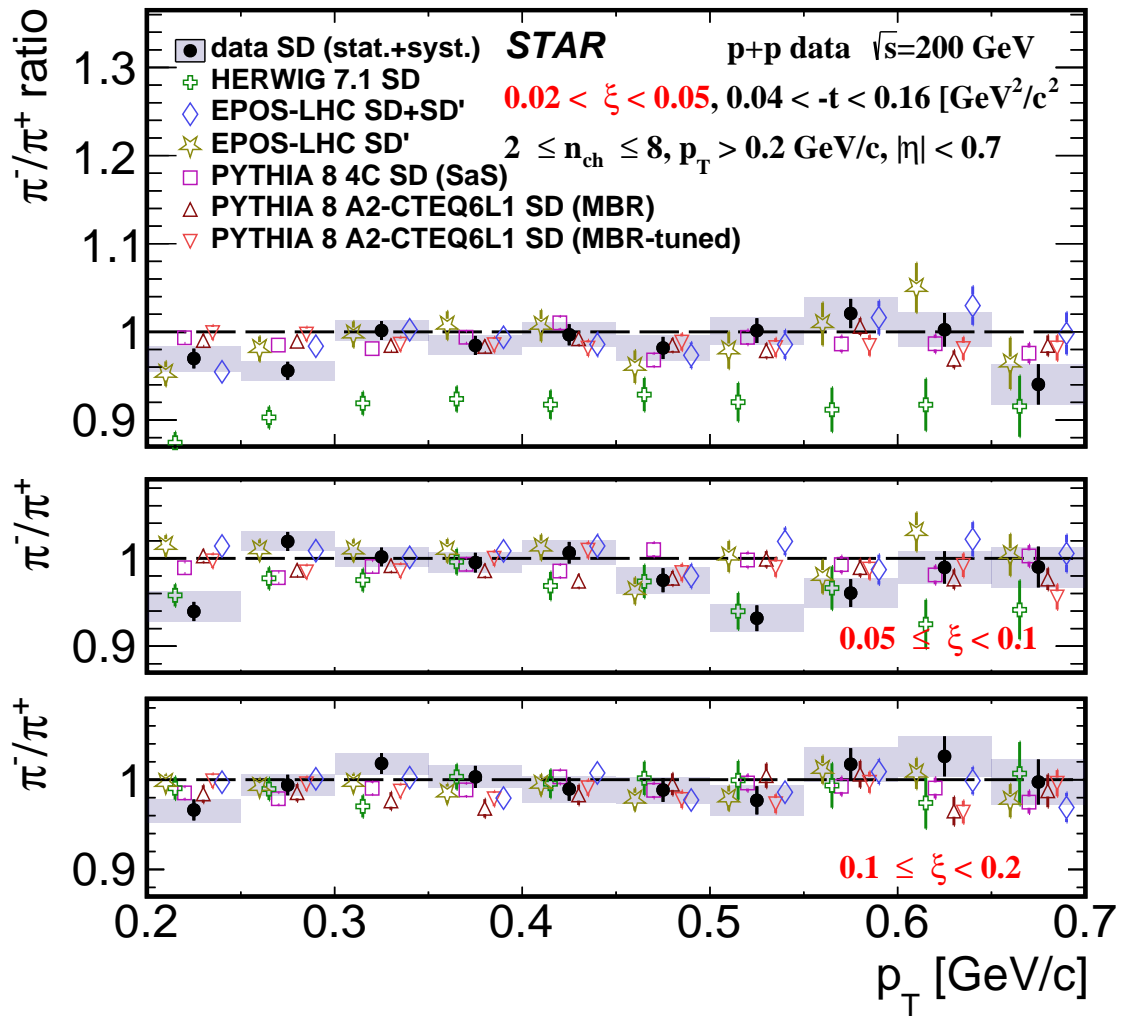


Figure 9.4: Ratio of production yields of  $\pi^-/\pi^+$  as a function of  $p_{\text{T}}$  shown separately for the three ranges of  $\xi$ : (top)  $0.02 < \xi < 0.05$ , (middle)  $0.05 < \xi < 0.1$ , (bottom)  $0.1 < \xi < 0.2$ .

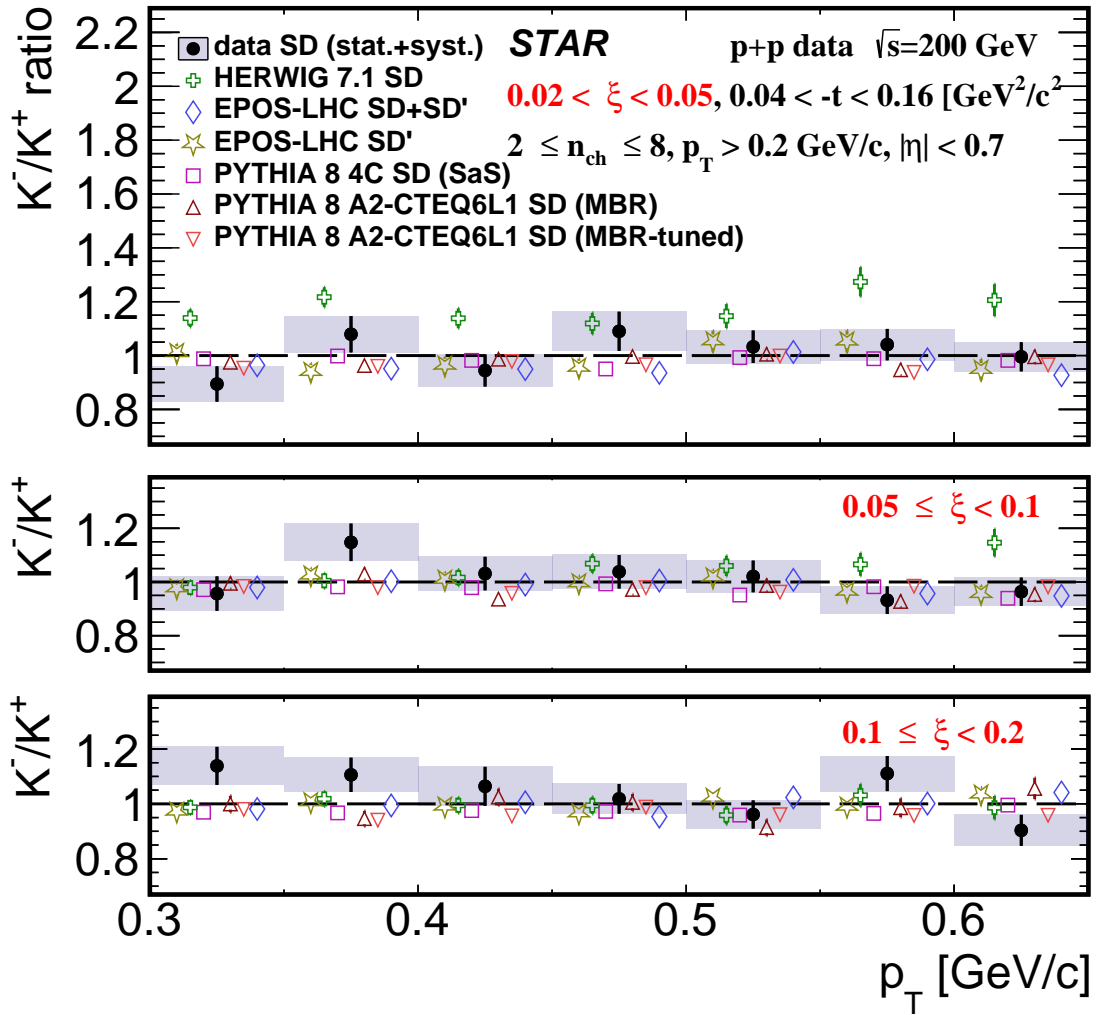


Figure 9.5: Ratio of production yields of  $K^-/K^+$  as a function of  $p_T$  shown separately for the three ranges of  $\xi$ : (top)  $0.02 < \xi < 0.05$ , (middle)  $0.05 < \xi < 0.1$ , (bottom)  $0.1 < \xi < 0.2$ .

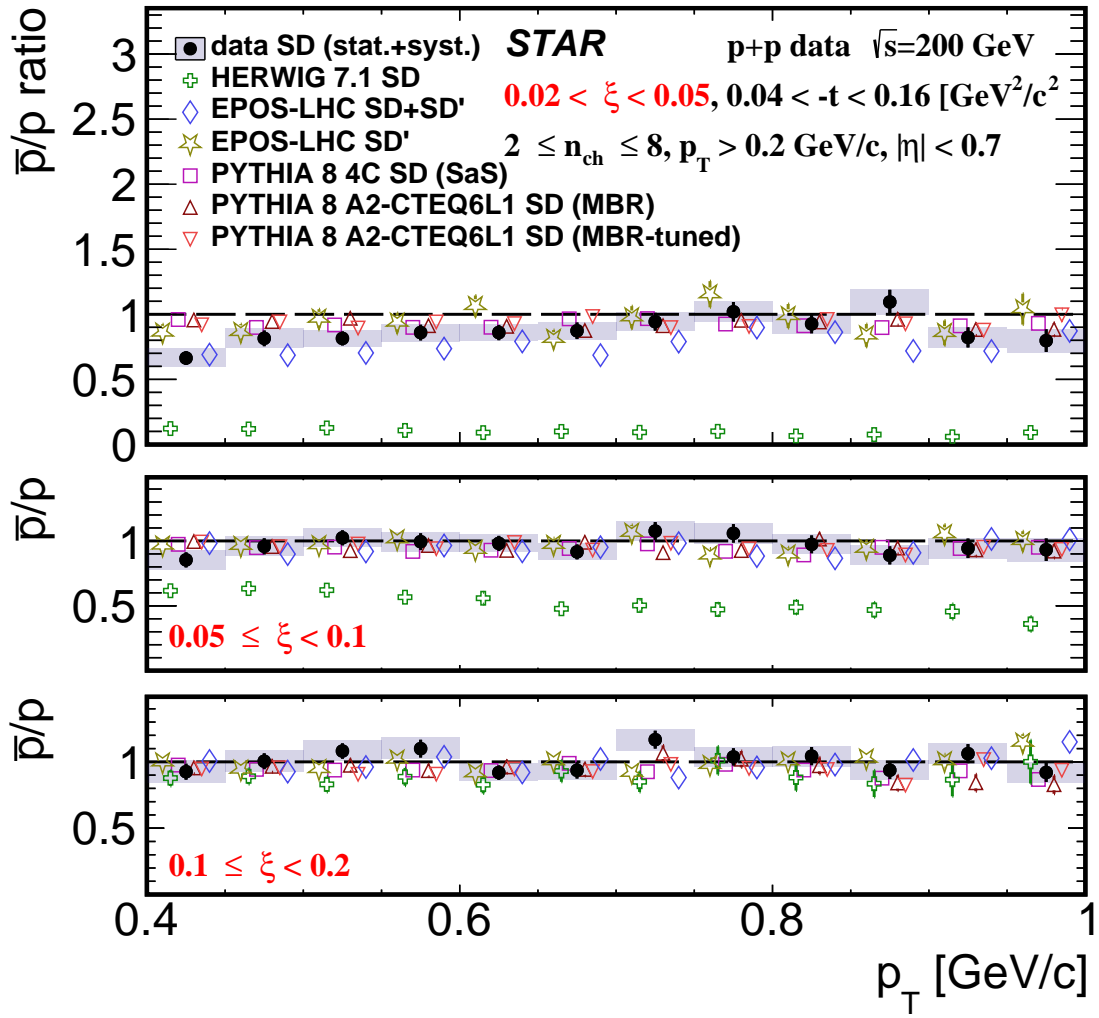


Figure 9.6: Ratio of production yields of  $\bar{p}/p$  as a function of  $p_{\text{T}}$  shown separately for the three ranges of  $\xi$ : (top)  $0.02 < \xi < 0.05$ , (middle)  $0.05 < \xi < 0.1$ , (bottom)  $0.1 < \xi < 0.2$ .

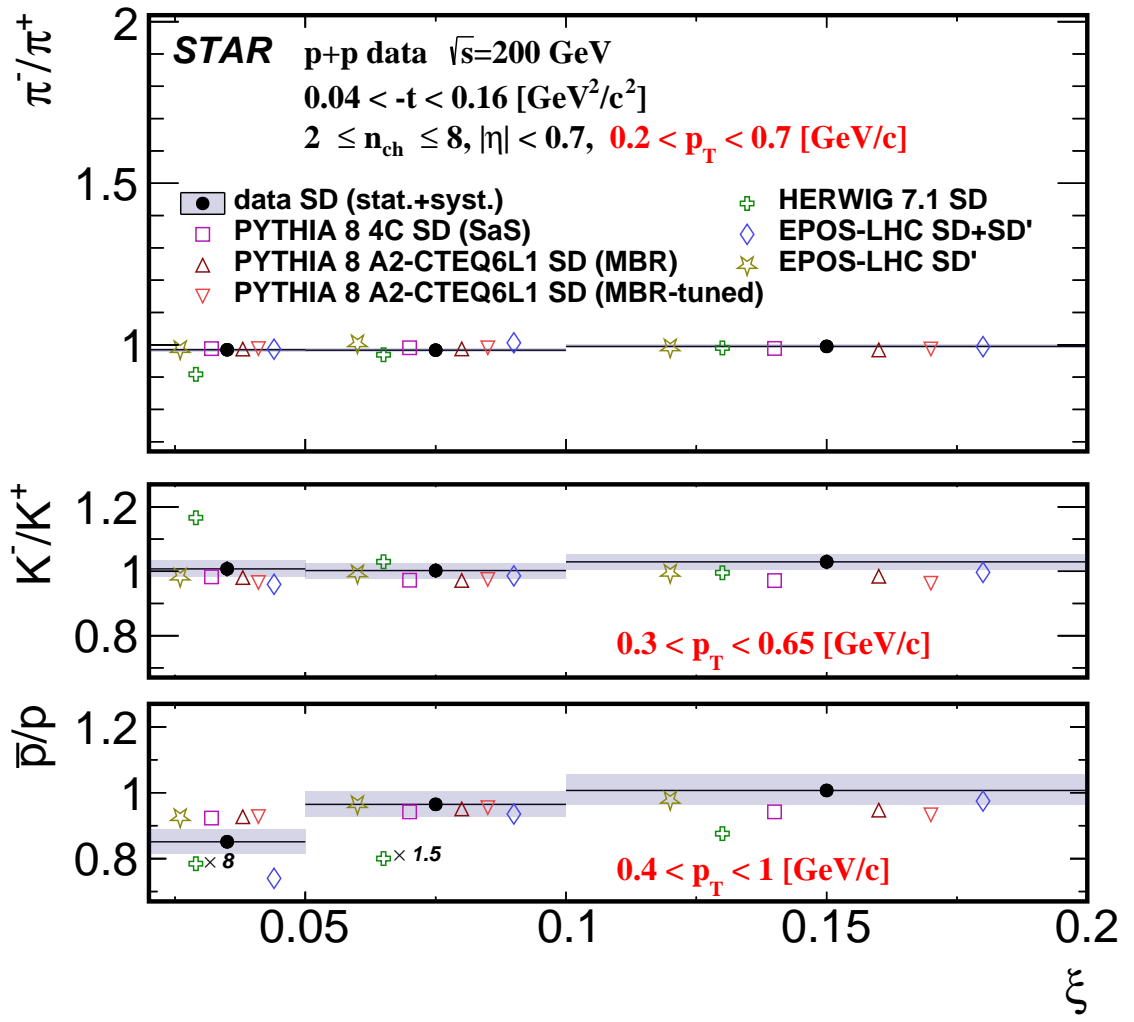


Figure 9.7: Ratio of production yields of  $\pi^-/\pi^+$ ,  $K^-/K^+$  and  $\bar{p}/p$  as a function of  $\xi$ .

## 956 9.1 Comparison of Charged-Particle Densities at Central 957 Rapidities

958 The measured charged-particle densities in pseudorapidity near  $\eta \approx 0$  are compared to other  
 959 experimental results from  $pp$  and  $p\bar{p}$  collisions (shown in Fig. 9.8). Various event selections, based  
 960 on the topology of the final state, allow to split the data samples into enhanced in non-SD (NSD)  
 961 and SD events, whose sum forms the inelastic sample. For SD events, the midrapidity region is  
 962 located at  $\bar{\eta} = \eta_m = -\ln(\sqrt{s}/M_X)$ , instead of  $\eta \approx 0$ , and the proper energy scale is given by  $M_X$   
 963 instead of  $\sqrt{s}$ . The values of  $\eta_m$  and  $\langle M_X \rangle$ , calculated for STAR data, are presented in Tab. 9.1.  
 964 For all three ranges of  $\xi$ , the value of  $\eta_m$  is outside the fiducial region of the measurement. In  
 965 the case of other experiments the pseudorapidity densities were obtained in the region of the total  
 966 number of primary charged particles  $n_{ch} \geq 1$  (instead of  $n_{ch} \geq 2$  as in these analyses). Therefore,  
 967 the results from STAR analysis were extrapolated to the above fiducial region using PYTHIA 8  
 968 A2 (MBR) SD predictions. The uncertainties due to the corrections are not estimated.

$\xi$ range	$\langle M_X \rangle$	$\eta_m$	$\eta_{edge}$
$0.02 < \xi < 0.05$	37.53 GeV	-1.67	2.02
$0.05 < \xi < 0.1$	53.52 GeV	-1.31	2.73
$0.1 < \xi < 0.2$	72.71 GeV	-1.01	3.34

Table 9.1: Values of  $\langle M_X \rangle$  and  $\eta_m = \ln(\sqrt{s}/M_X)$  for three ranges of  $\xi$  and position of gap edge  $\eta_{edge}$ .

969 The extrapolation procedure was as follows:

- 970 • the ratio of particle density at  $\bar{\eta} = \eta_m$  and  $n_{ch} \geq 1$  to that at  $\bar{\eta} = 0$  and  $n_{ch} \geq 2$  was  
 971 calculated using PYTHIA 8 predictions,
- 972 • differences in the slope of the pseudorapidity distribution in the region of  $n_{ch} \geq 2$  were  
 973 observed between data and MC. Therefore, data and MC distributions were normalized to  
 974 have the same particle density at  $\bar{\eta} \approx 0$  and their ratio was fitted with a linear function,
- 975 • the correction from step #1, multiplied by the value of the above function at  $\bar{\eta} = \eta_m$ , was  
 976 used to scale the measured particle density at  $\bar{\eta} \approx 0$ .

977 Figure 9.8 presents the charged-particle densities near  $\eta \approx 0$  as a function of  $\sqrt{s}$  in inelastic  
 978  $pp$  and  $p\bar{p}$  collisions. The SD results, calculated near  $\bar{\eta} = \eta_m$  at  $\sqrt{s}$  ( $M_X$ ), are also shown.

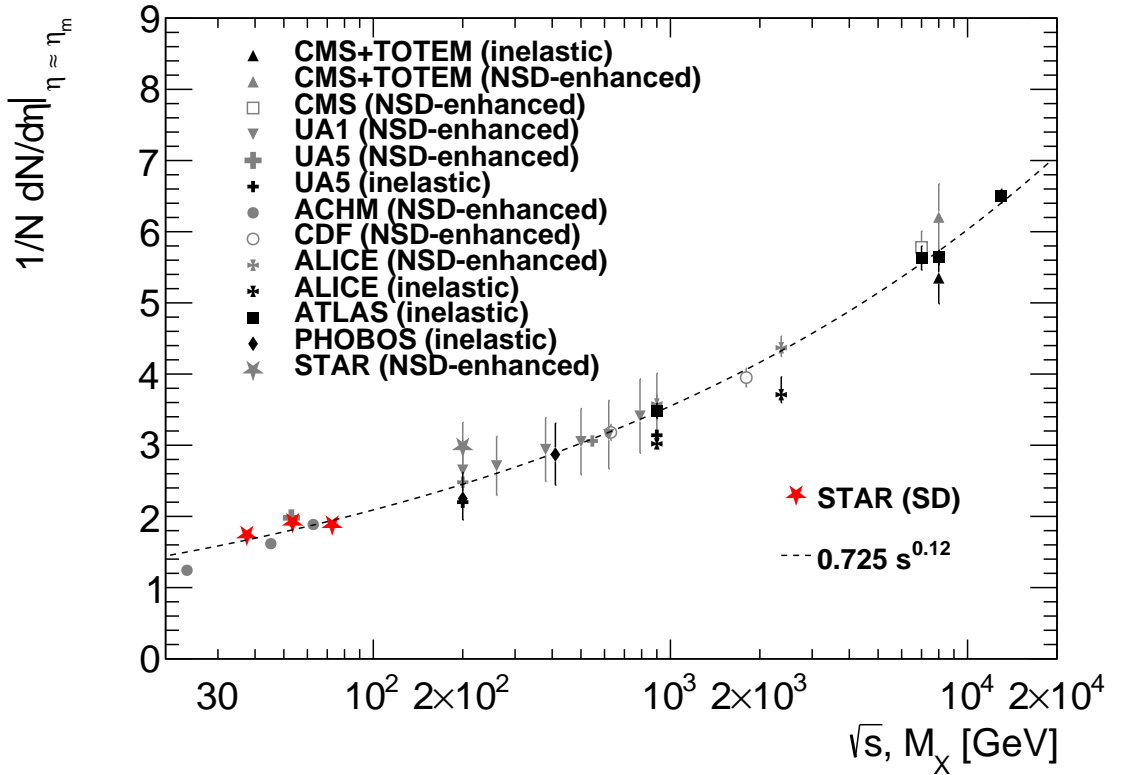


Figure 9.8: The evolution of  $1/N_{\text{ev}} dN/d\eta$  at  $\eta \approx 0$  as a function of  $\sqrt{s}$  in inelastic  $pp$  and  $p\bar{p}$  collisions [12, 17, 18, 19, 20, 21, 22, 23, 24, 25, 26, 27]. The SD results were calculated near  $\bar{\eta} \approx \eta_m$  at  $\sqrt{s}$  ( $M_X$ ). The dashed lines represent power-law fits to the NSD-enhanced [17] data. The results from this analysis are shown in red.

## 10. Kaon to Pion Ratio

## 980 11. Summary and Conclusions

981 Inclusive and identified (pion, kaon, proton and their antiparticles) charged particle production in  
982 Single Diffractive Dissociation process has been measured in proton-proton collisions at  $\sqrt{s} = 200$   
983 GeV with the STAR detector at RHIC using data corresponding to an integrated luminosity of  
984  $15 \text{ nb}^{-1}$ .

985 Significant differences are observed between the measured distributions of  $\xi$  and MC model  
986 predictions. Amongst the models considered, EPOS and PYTHIA 8 (MBR) without artificial  
987 suppression of diffractive cross sections at large  $\xi$  provide the best description of the data.

988 Charged-particle multiplicity and its dependence on the pseudorapidity and the transverse  
989 momentum are well described by PYTHIA8 and EPOS SD' models. EPOS SD+SD' and HERWIG  
990 do not describe the data.

991  $\pi^-/\pi^+$  and  $K^-/K^+$  production ratios are close to unity and consistent with most of model  
992 predictions except for HERWIG.

993  $\bar{p}/p$  production ratio shows a significant deviation from unity in the  $0.02 < \xi < 0.05$  range  
994 indicating a non-negligible transfer of the baryon number from the forward to the central region.  
995 Equal amount of protons and antiprotons are observed in the  $\xi > 0.05$  range. PYTHIA8, EPOS  
996 SD+SD' and EPOS SD' agree with data for  $\xi > 0.05$ . For  $0.02 < \xi < 0.05$  PYTHIA 8 and  
997 EPOS SD' predict small deviations from unity (0.93) which is however higher than observed  
998 in data ( $0.85 \pm 0.04$ ). EPOS SD+SD' predicts an asymmetry between  $\bar{p}$  and  $p$  of  $\sim 30\%$  at  
999  $0.02 < \xi < 0.05$ . HERWIG predicts much larger baryon number transfers compared to data for  
1000  $\xi < 0.1$  and shows consistency with data for  $\xi > 0.1$ .

# 1001 Bibliography

- 1002 [1] L. Adamczyk, L. Fulek, and R. Sikora, *Supplementary note on diffractive analyses of 2015*  
1003 *proton-proton data*, <https://drupal.star.bnl.gov/STAR/starnotes/private/psn0732>,  
1004 July, 2019.
- 1005 [2] B. Z. Kopeliovich and B. G. Zakharov, *Novel Mechanisms of Baryon Number Flow Over*  
1006 *Large Rapidity Gap*, *Z. Phys. C* **43** (1989) 241.
- 1007 [3] F. W. Bopp, *Baryon transport in dual models and the possibility of a backward peak in*  
1008 *diffraction*, in *New trends in high-energy physics: Experiment, phenomenology, theory.*  
1009 *Proceedings, International School-Conference, Crimea 2000, Yalta, Ukraine, May 27-June 4,*  
1010 *2000*. arXiv:hep-ph/0007229 [hep-ph].
- 1011 [4] M. Anderson et al., *The STAR Time Projection Chamber: A Unique tool for studying high*  
1012 *multiplicity events at RHIC*, *Nucl. Instrum. Meth. A* **499** (2003) 659–678,  
1013 arXiv:nucl-ex/0301015 [nucl-ex].
- 1014 [5] T. Sjöstrand, S. Mrenna, and P. Z. Skands, *PYTHIA 6.4 Physics and Manual*, *JHEP* **05**  
1015 (2006) 026.
- 1016 [6] R. Ciesielski and K. Goulianos, *MBR Monte Carlo Simulation in PYTHIA8*, *PoS*  
1017 *ICHEP2012* (2013) 301, arXiv:1205.1446 [hep-ph].
- 1018 [7] *Roman Pot Phase II\* - online DAQ monitoring*,  
1019 <https://online.star.bnl.gov/rp/pp200/>.
- 1020 [8] *STAR RunLog Browser*, <https://online.star.bnl.gov/RunLogRun15/>.
- 1021 [9] W. Fischer, *Run Overview of the Relativistic Heavy Ion Collider*,  
1022 <http://www.agsrhichome.bnl.gov/RHIC/Runs/>.
- 1023 [10] *STAR Luminosity Tracker*, <https://www.star.bnl.gov/protected/common/common2015/trigger2015/runningStatepp200GeV/plots.html>.
- 1025 [11] STAR Collaboration, J. Adam et al., *Results on Total and Elastic Cross Sections in*  
1026 *Proton-Proton Collisions at  $\sqrt{s} = 200$  GeV*, arXiv:2003.12136 [hep-ex].
- 1027 [12] STAR Collaboration, B. I. Abelev et al., *Systematic Measurements of Identified Particle*  
1028 *Spectra in pp, d<sup>+</sup> Au and Au+Au Collisions from STAR*, *Phys. Rev. C* **79** (2009) 034909,  
1029 arXiv:0808.2041 [nucl-ex].
- 1030 [13] CDF Collaboration, D. Acosta et al., *Inclusive double pomeron exchange at the Fermilab*  
1031 *Tevatron  $\bar{p}p$  collider*, *Phys. Rev. Lett.* **93** (2004) 141601, arXiv:hep-ex/0311023 [hep-ex].
- 1032 [14] ATLAS Collaboration, G. Aad et al., *Charged-particle distributions in  $\sqrt{s} = 13$  TeV pp*  
1033 *interactions measured with the ATLAS detector at the LHC*, *Phys. Lett. B* **758** (2016)  
1034 67–88, arXiv:1602.01633 [hep-ex].

- 1035 [15] G. D'Agostini, *A Multidimensional unfolding method based on Bayes' theorem*, Nucl.  
 1036 Instrum. Meth. **A362** (1995) 487–498.
- 1037 [16] H. Bichsel, *A method to improve tracking and particle identification in TPCs and silicon  
 1038 detectors*, Nucl. Instrum. Meth. **A562** (2006) 154–197.
- 1039 [17] CMS, TOTEM Collaboration, S. Chatrchyan et al., *Measurement of pseudorapidity  
 1040 distributions of charged particles in proton-proton collisions at  $\sqrt{s} = 8$  TeV by the CMS and  
 1041 TOTEM experiments*, Eur. Phys. J. **C74** (2014) 3053.
- 1042 [18] UA1 Collaboration, C. Albajar et al., *A Study of the General Characteristics of  $p\bar{p}$   
 1043 Collisions at  $\sqrt{s} = 0.2$ -TeV to 0.9-TeV*, Nucl. Phys. **B335** (1990) 261–287.
- 1044 [19] UA5 Collaboration, G. J. Alner et al., *Scaling of Pseudorapidity Distributions at c.m.  
 1045 Energies Up to 0.9-TeV*, Z. Phys. **C33** (1986) 1–6.
- 1046 [20] ACHM Collaboration, W. Thome et al., *Charged Particle Multiplicity Distributions in  $p\bar{p}$   
 1047 Collisions at ISR Energies*, Nucl. Phys. **B129** (1977) 365.
- 1048 [21] CDF Collaboration, F. Abe et al., *Pseudorapidity distributions of charged particles produced  
 1049 in  $\bar{p}p$  interactions at  $\sqrt{s} = 630$  GeV and 1800 GeV*, Phys. Rev. **D41** (1990) 2330.
- 1050 [22] ALICE Collaboration, K. Aamodt et al., *Charged-particle multiplicity measurement in  
 1051 proton-proton collisions at  $\sqrt{s} = 0.9$  and 2.36 TeV with ALICE at LHC*, Eur. Phys. J. **C68**  
 1052 (2010) 89–108.
- 1053 [23] ATLAS Collaboration, M. Aaboud et al., *Charged-particle distributions at low transverse  
 1054 momentum in  $\sqrt{s} = 13$  TeV  $pp$  interactions measured with the ATLAS detector at the LHC*,  
 1055 Eur. Phys. J. **C76** (2016) 502, [arXiv:1606.01133 \[hep-ex\]](https://arxiv.org/abs/1606.01133).
- 1056 [24] ATLAS Collaboration, G. Aad et al., *Charged-particle distributions in  $pp$  interactions at  
 1057  $\sqrt{s} = 8$  TeV measured with the ATLAS detector*, Eur. Phys. J. **C76** (2016) 403.
- 1058 [25] ATLAS Collaboration, G. Aad et al., *Charged-particle multiplicities in  $pp$  interactions  
 1059 measured with the ATLAS detector at the LHC*, New J. Phys. **13** (2011) 053033.
- 1060 [26] PHOBOS Collaboration, B. Alver et al., *Phobos results on charged particle multiplicity and  
 1061 pseudorapidity distributions in  $Au+Au$ ,  $Cu+Cu$ ,  $d+Au$ , and  $p+p$  collisions at  
 1062 ultra-relativistic energies*, Phys. Rev. **C83** (2011) 024913.
- 1063 [27] CMS Collaboration, V. Khachatryan et al., *Transverse-momentum and pseudorapidity  
 1064 distributions of charged hadrons in  $pp$  collisions at  $\sqrt{s} = 7$  TeV*, Phys. Rev. Lett. **105**  
 1065 (2010) 022002, [arXiv:1005.3299 \[hep-ex\]](https://arxiv.org/abs/1005.3299).

# Appendices

<sup>1067</sup> **A. Proton and Antiproton DCA  
Distributions**

<sup>1068</sup>

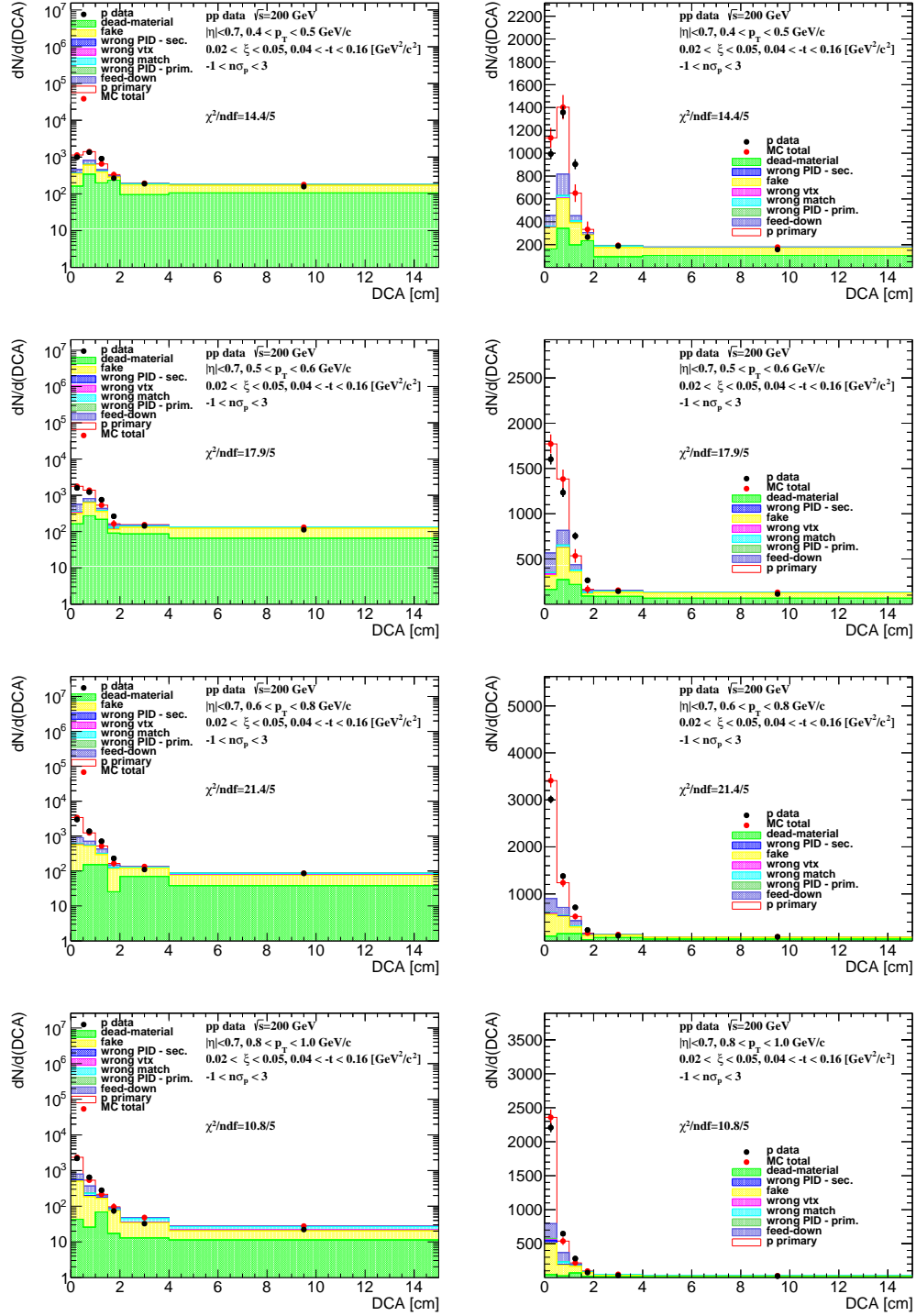


Figure A.1: Distributions of DCA for protons in SD interactions with  $0.02 < \xi < 0.05$  and loose selection.

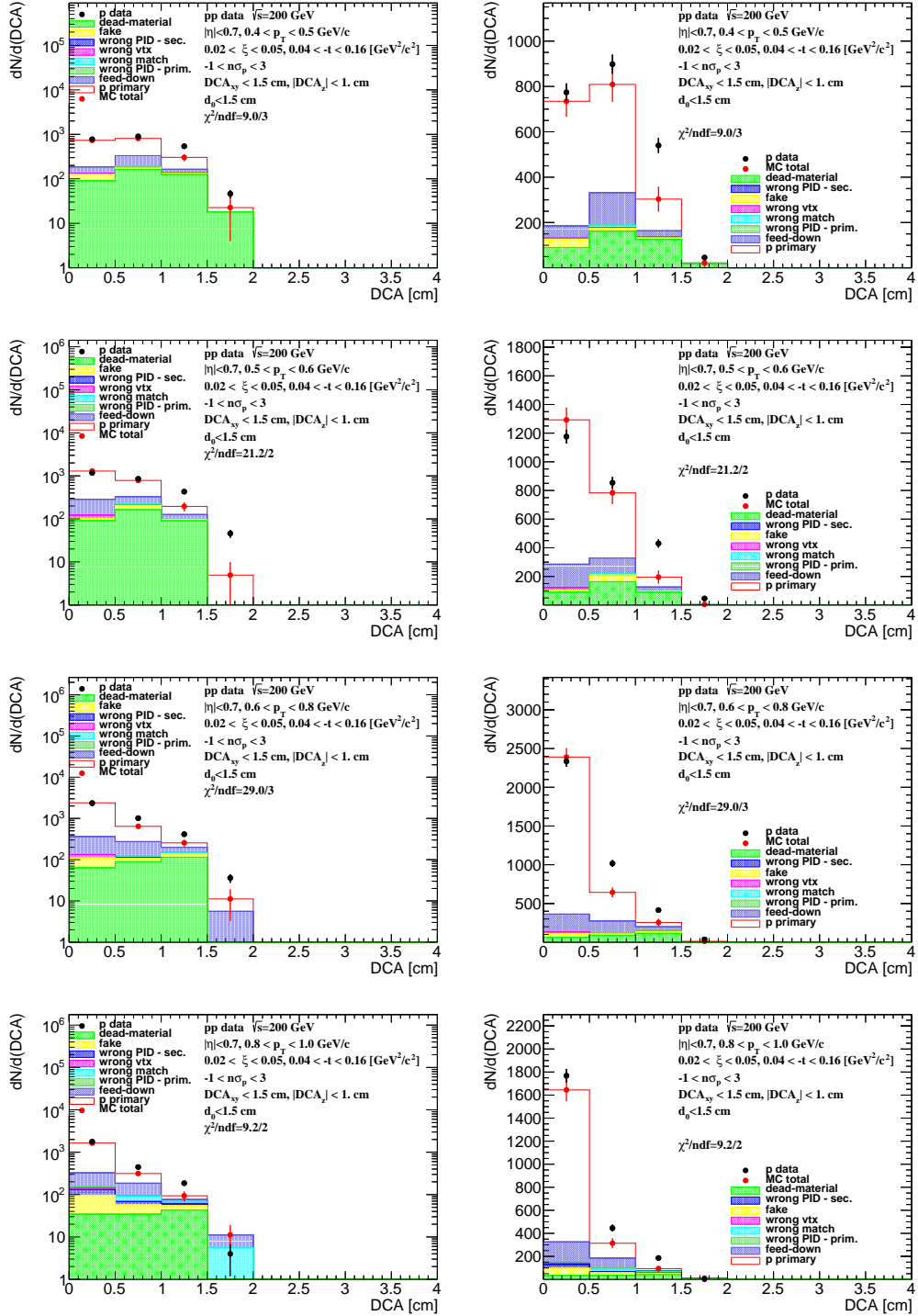


Figure A.2: Distributions of DCA for protons in SD interactions with  $0.02 < \xi < 0.05$  and normal selection.

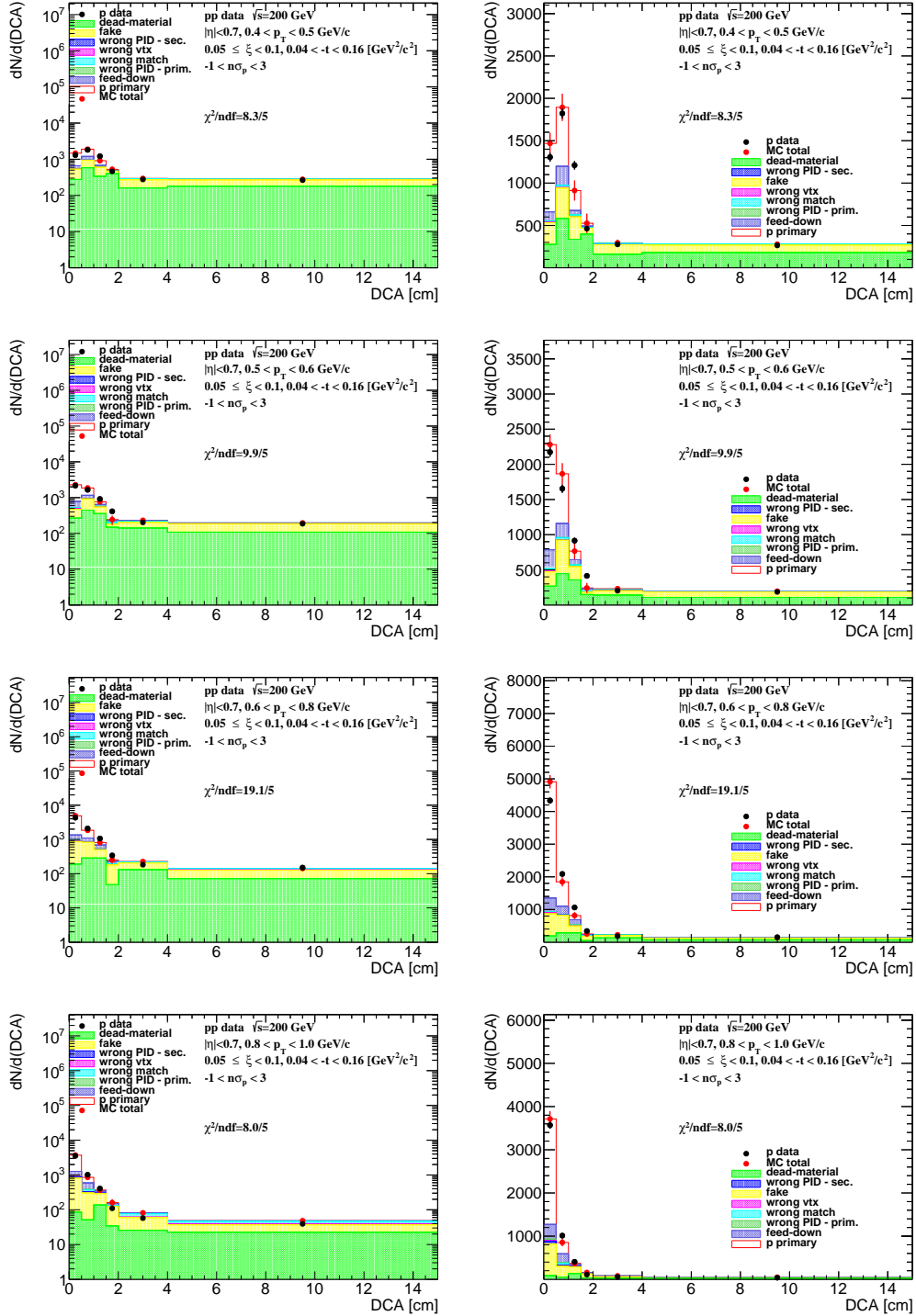


Figure A.3: Distributions of DCA for protons in SD interactions with  $0.05 < \xi < 0.1$  and loose selection.

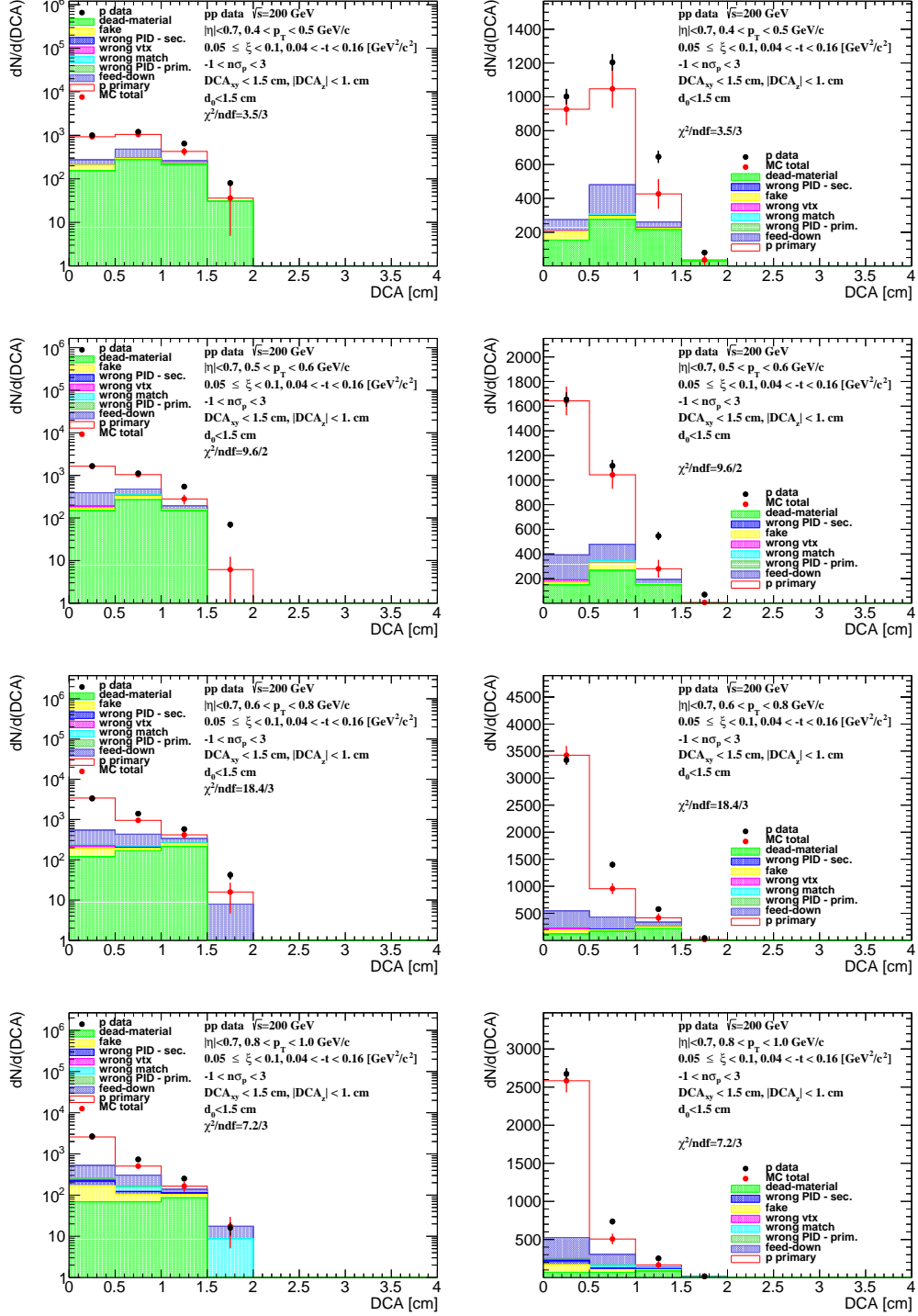


Figure A.4: Distributions of DCA for protons in SD interactions with  $0.05 < \xi < 0.1$  and normal selection.

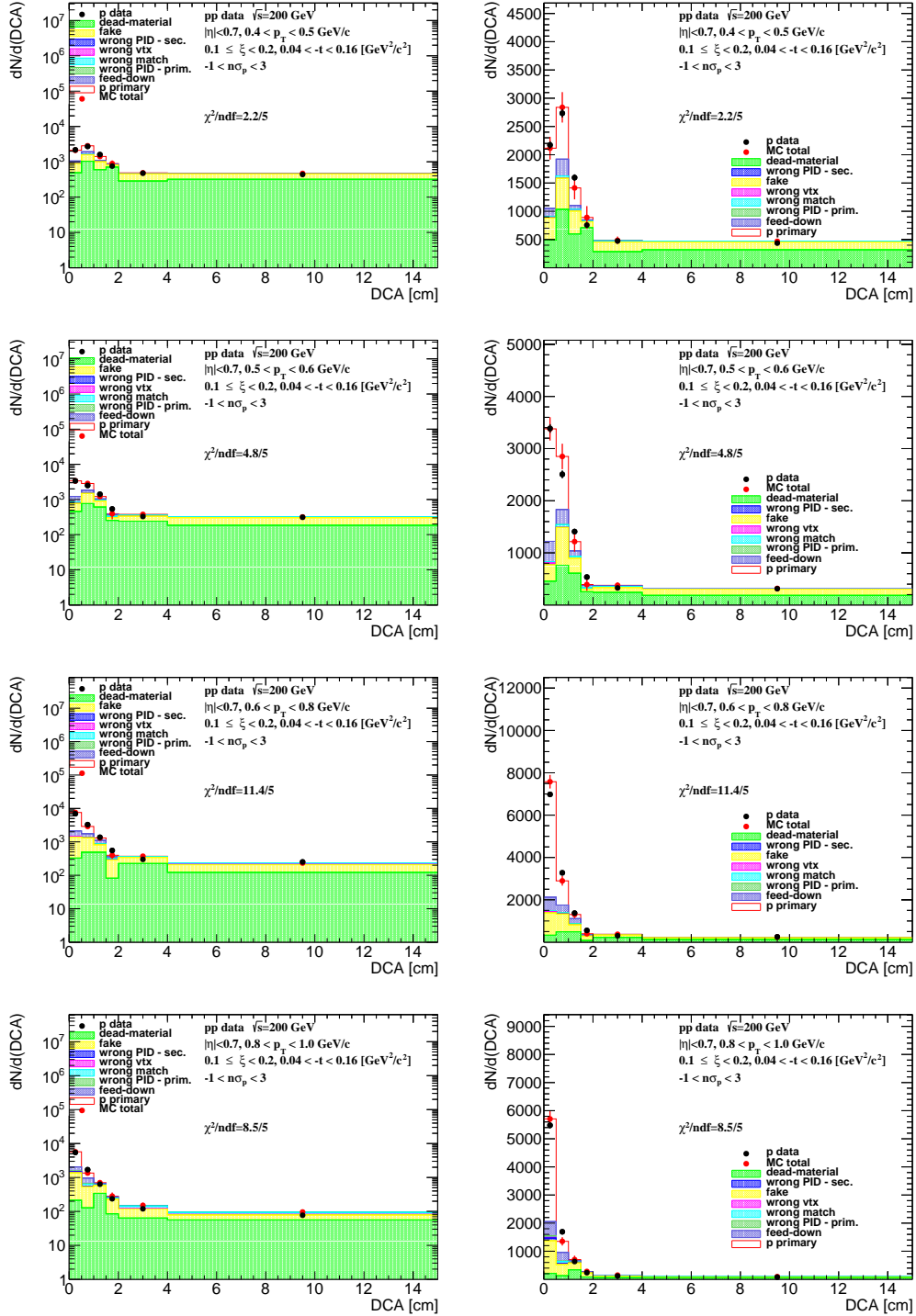


Figure A.5: Distributions of DCA for protons in SD interactions with  $0.1 < \xi < 0.2$  and loose selection.

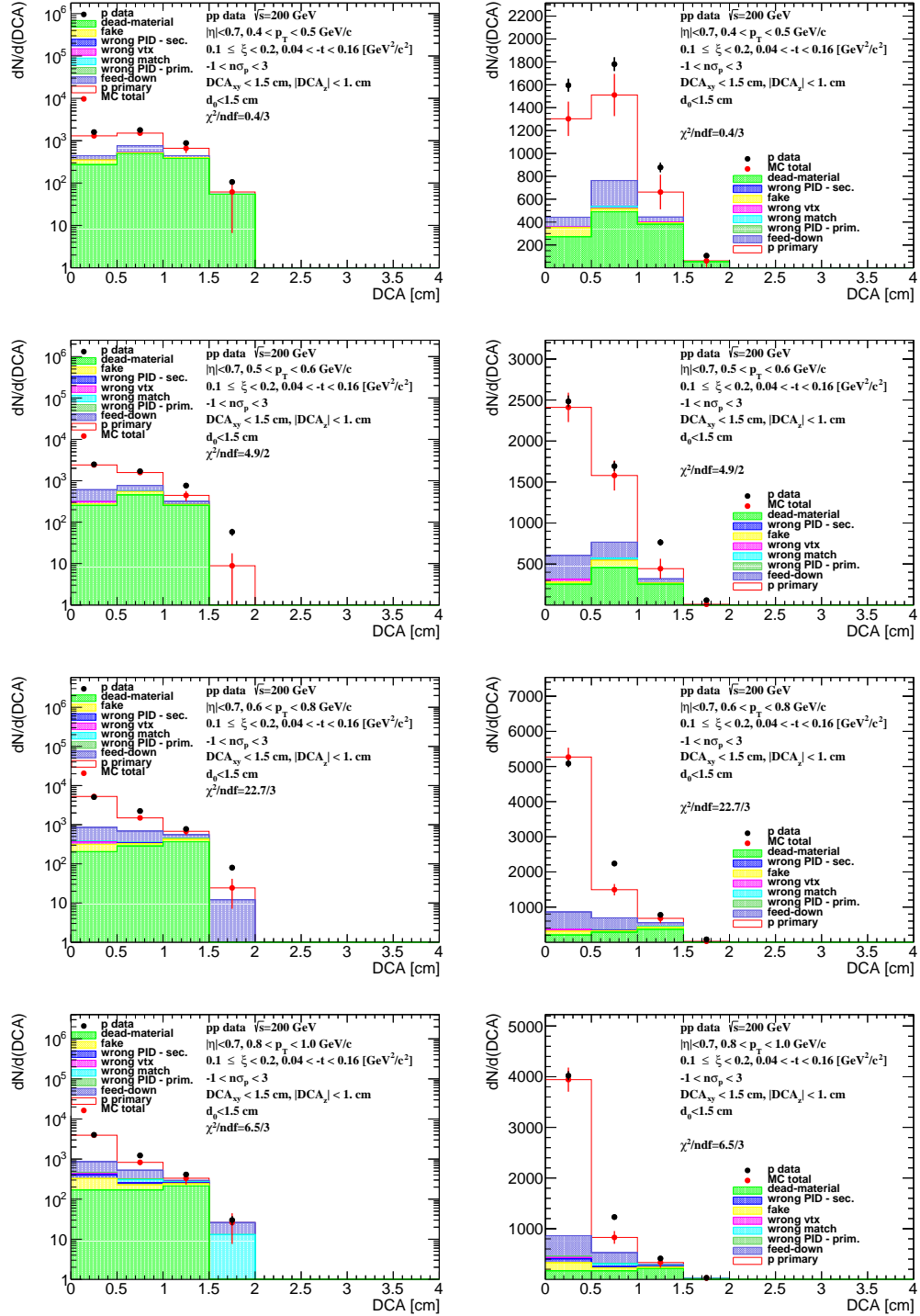


Figure A.6: Distributions of DCA for protons in SD interactions with  $0.1 < \xi < 0.2$  and normal selection.

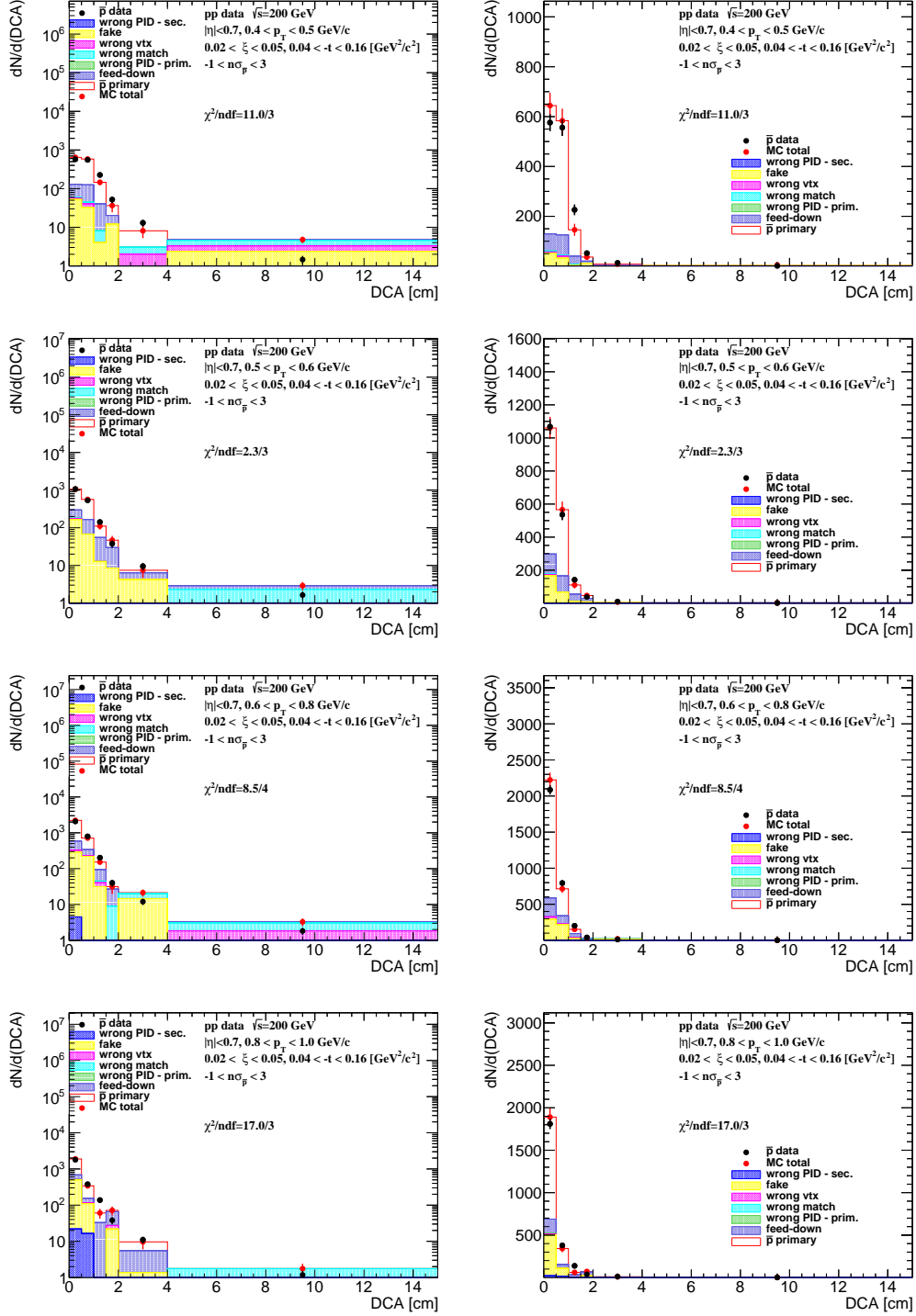


Figure A.7: Distributions of DCA for antiprotons in SD interactions with  $0.02 < \xi < 0.05$  and loose selection.

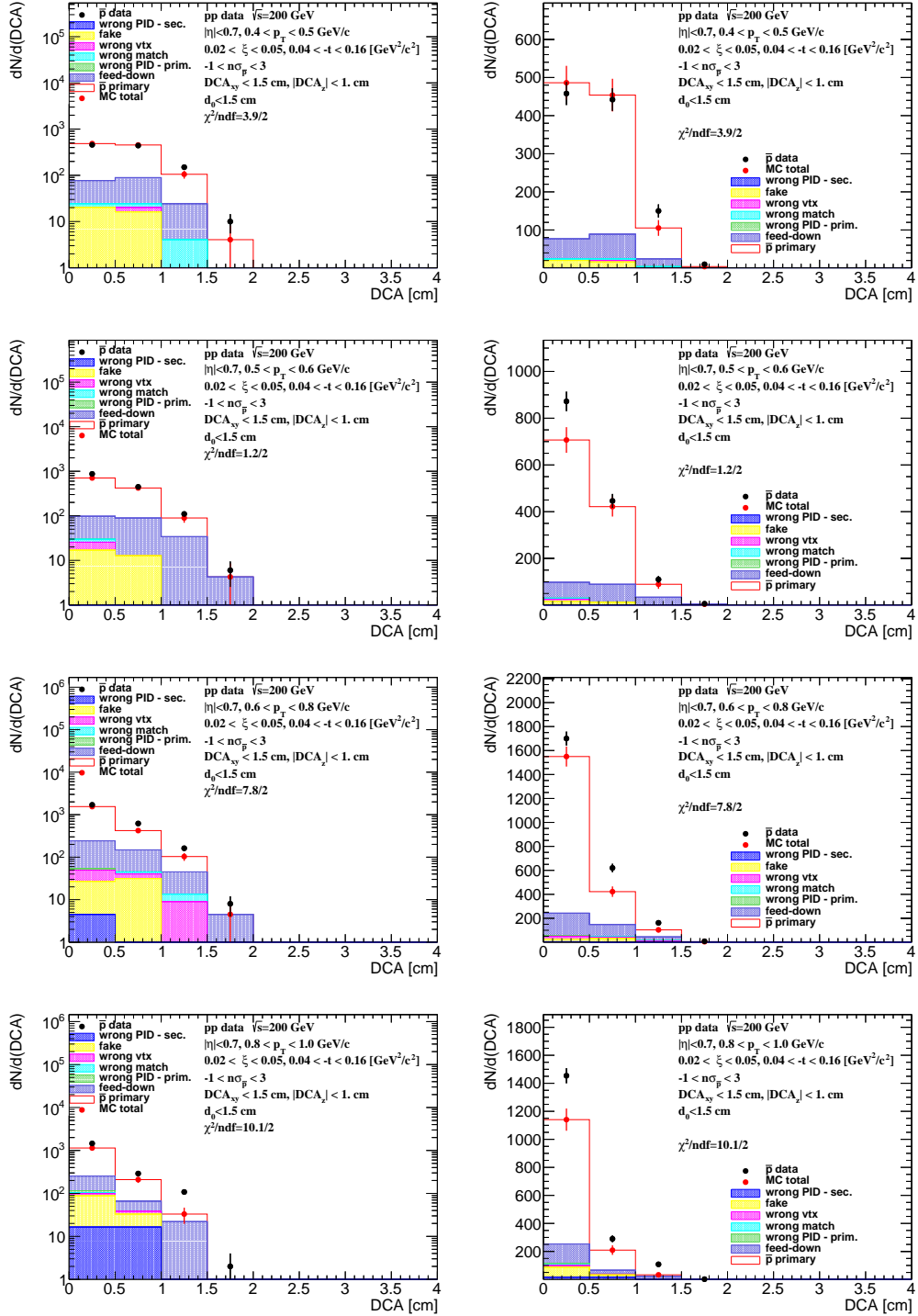


Figure A.8: Distributions of DCA for antiprotons in SD interactions with  $0.02 < \xi < 0.05$  and normal selection.

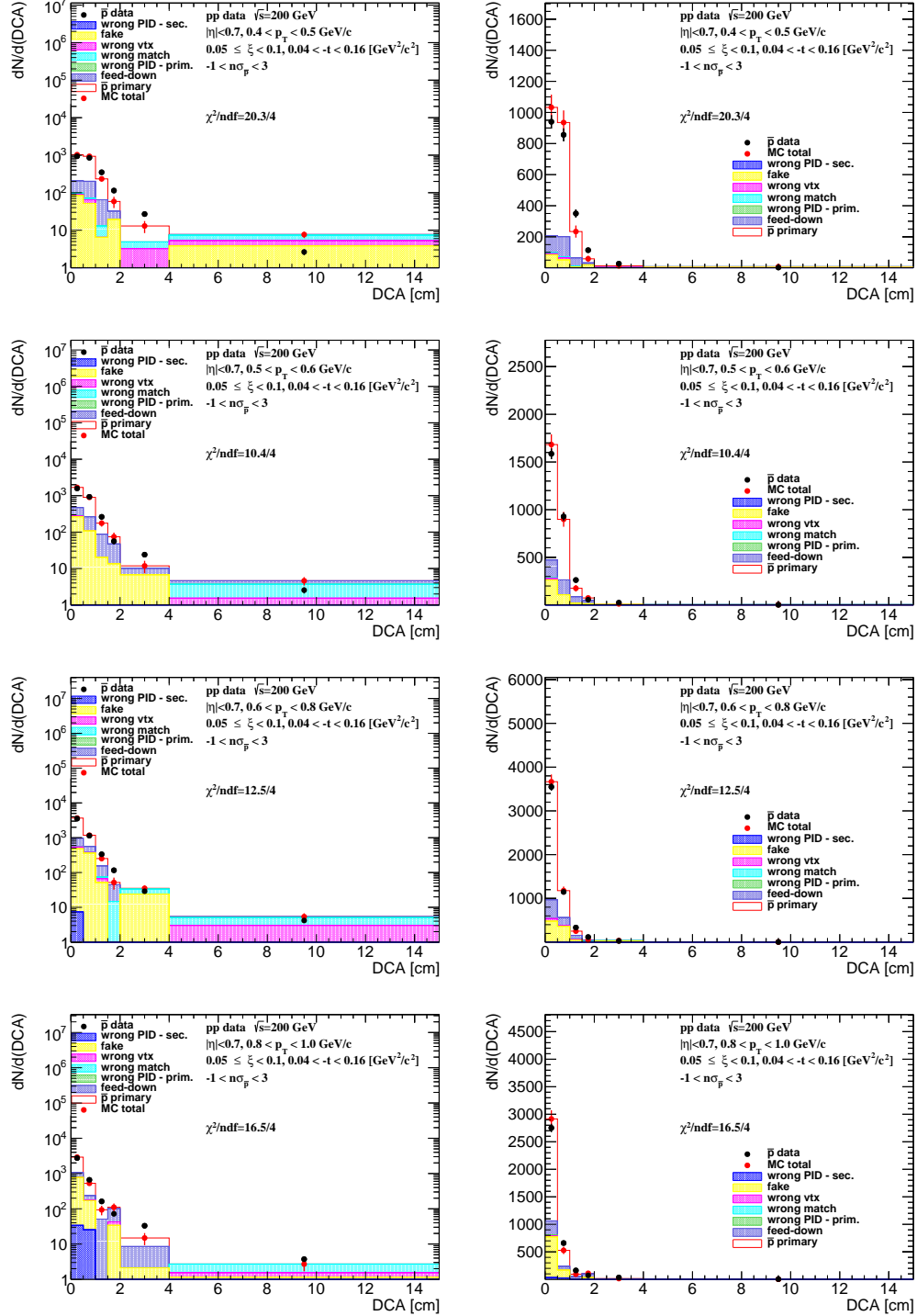


Figure A.9: Distributions of DCA for antiprotons in SD interactions with  $0.05 < \xi < 0.1$  and loose selection.

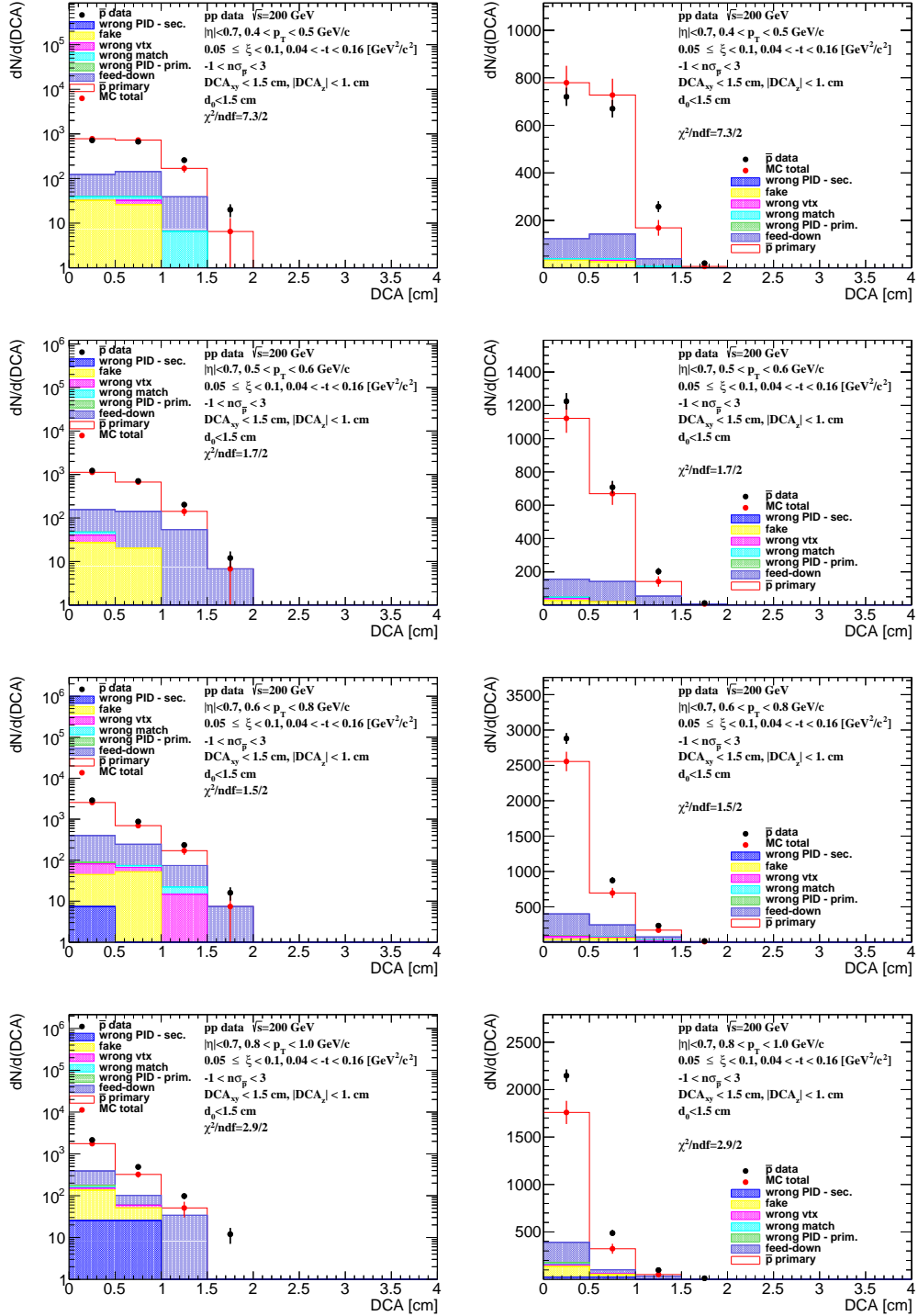


Figure A.10: Distributions of DCA for antiprotons in SD interactions with  $0.05 < \xi < 0.1$  and normal selection.

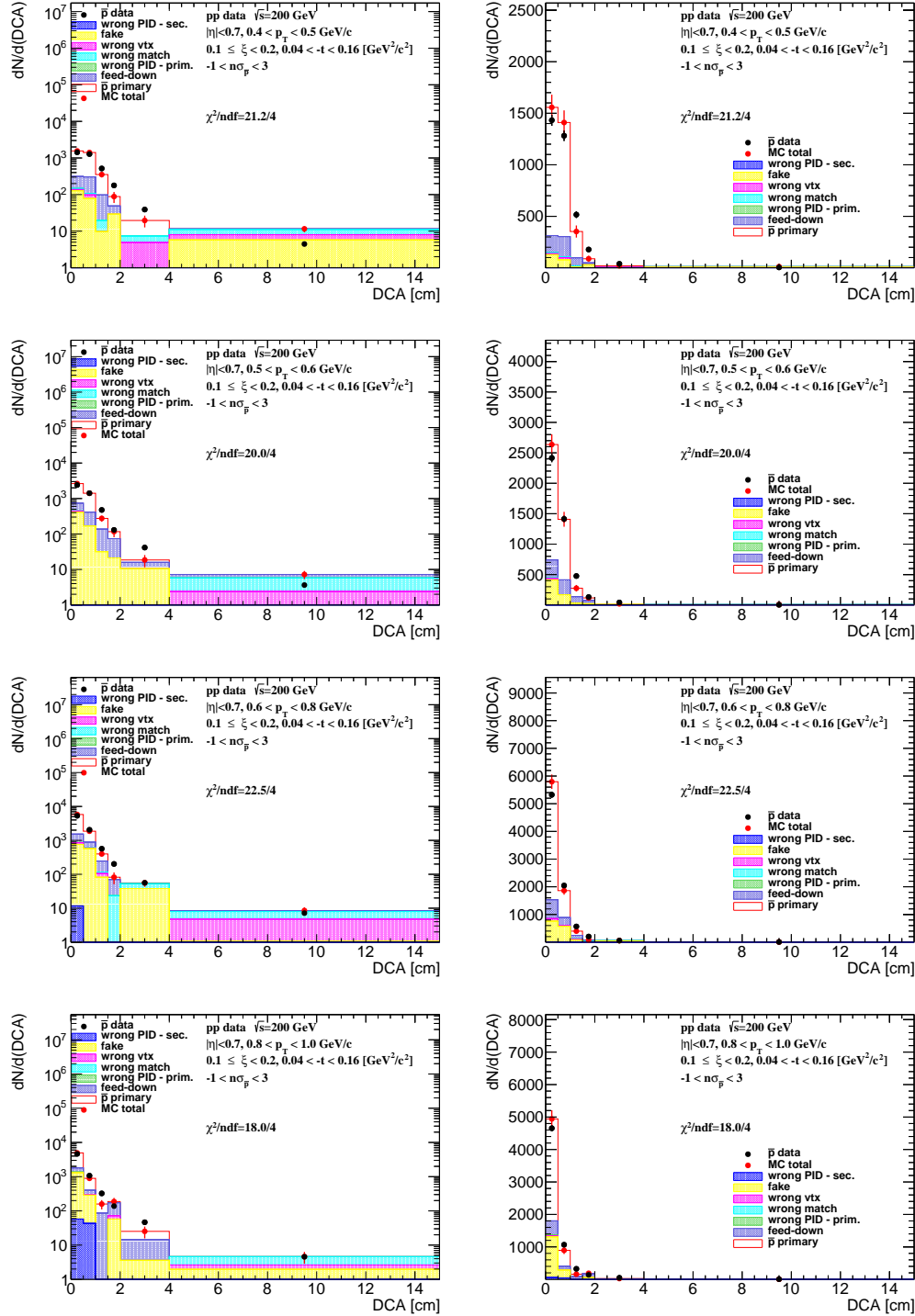


Figure A.11: Distributions of DCA for antiprotons in SD interactions with  $0.1 < \xi < 0.2$  and loose selection.

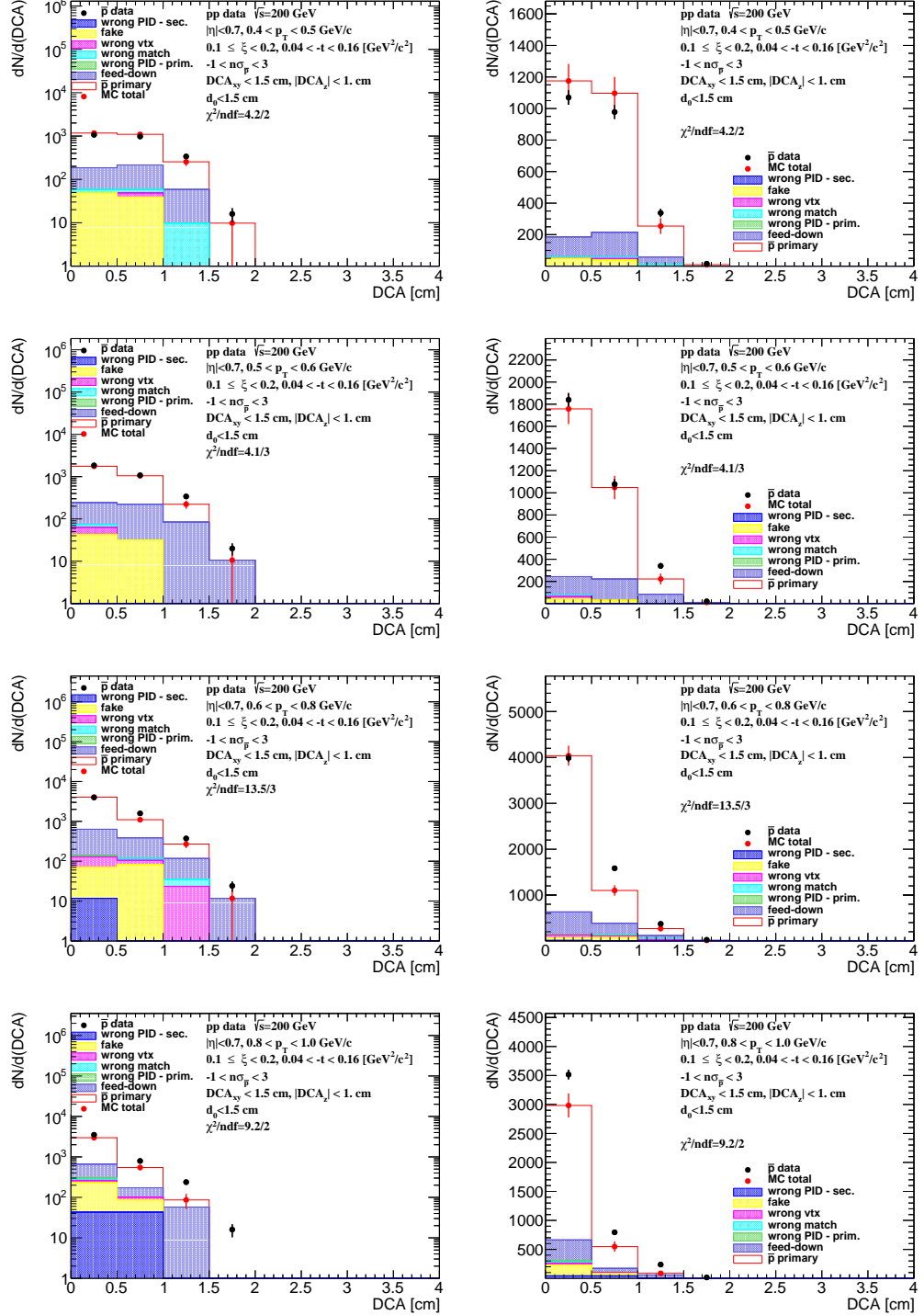


Figure A.12: Distributions of DCA for antiprotons in SD interactions with  $0.1 < \xi < 0.2$  and normal selection.

## B. Distributions of $n\sigma_{dE/dx}^i$ in SD

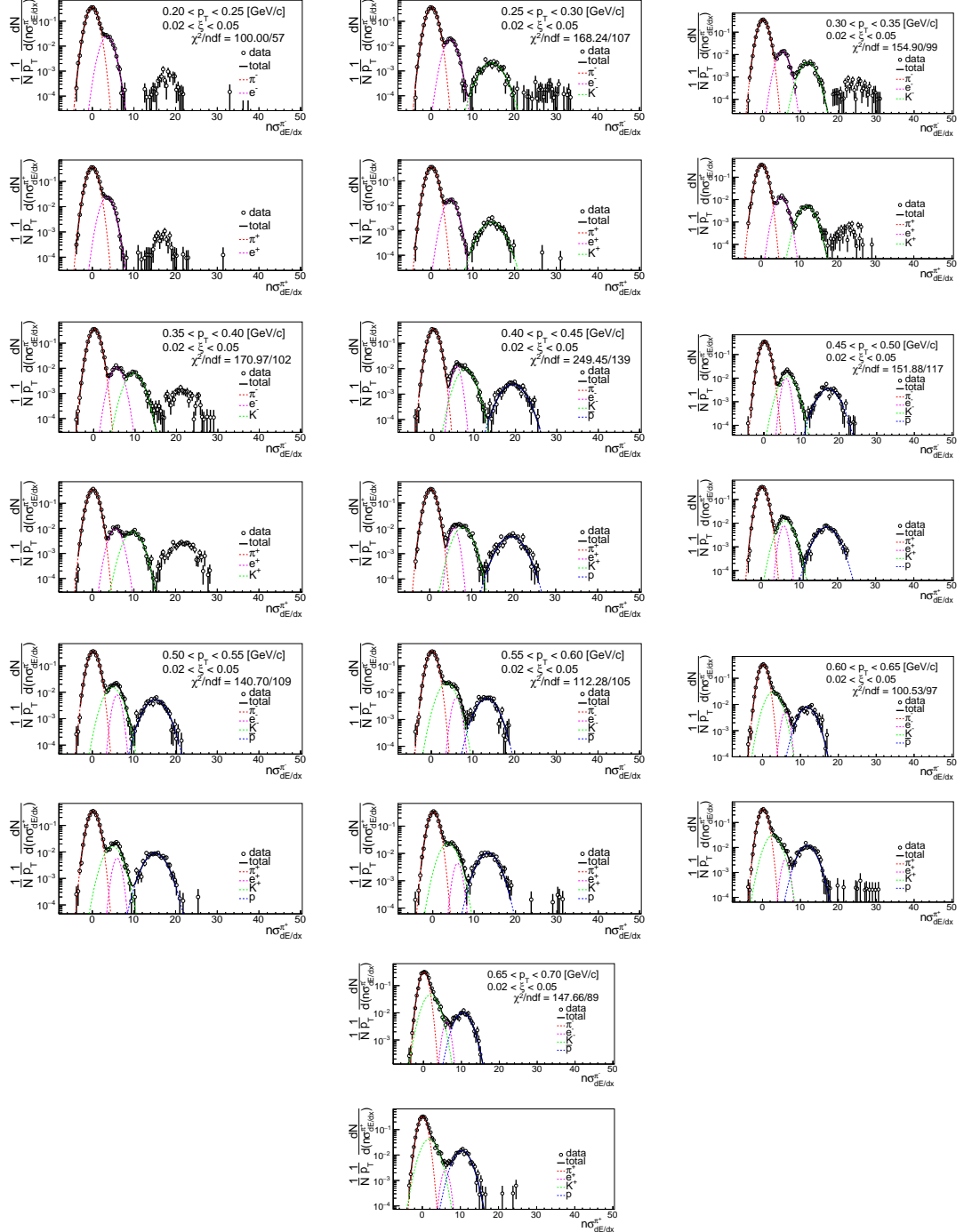


Figure B.1: Distributions of  $n\sigma_{dE/dx}^{\pi^\pm}$  for  $\pi^\pm$  in SD interactions with  $0.02 < \xi < 0.05$ .

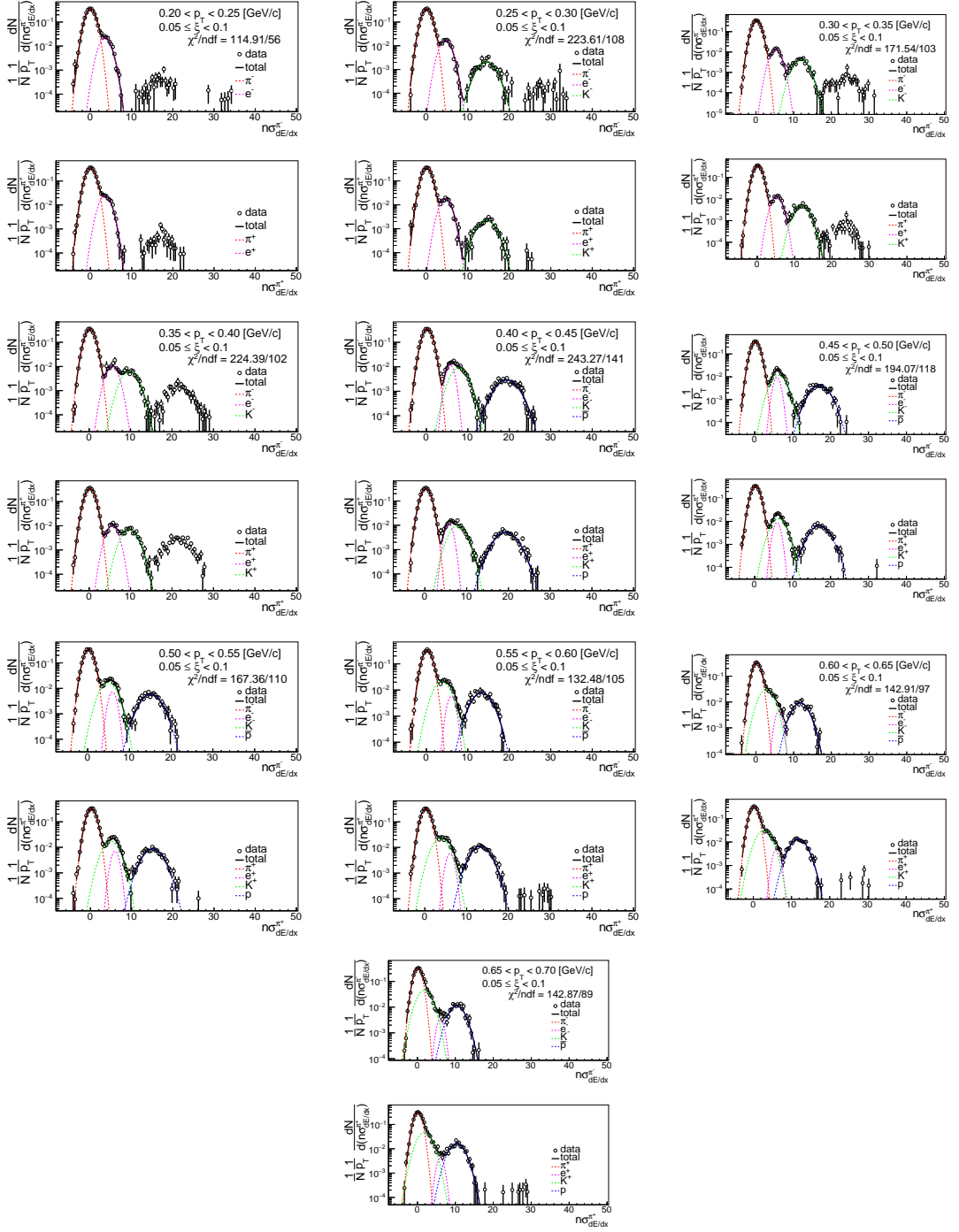


Figure B.2: Distributions of  $n\sigma_{dE/dx}^{\pi^\pm}$  for  $\pi^\pm$  in SD interactions with  $0.05 < \xi < 0.1$ .

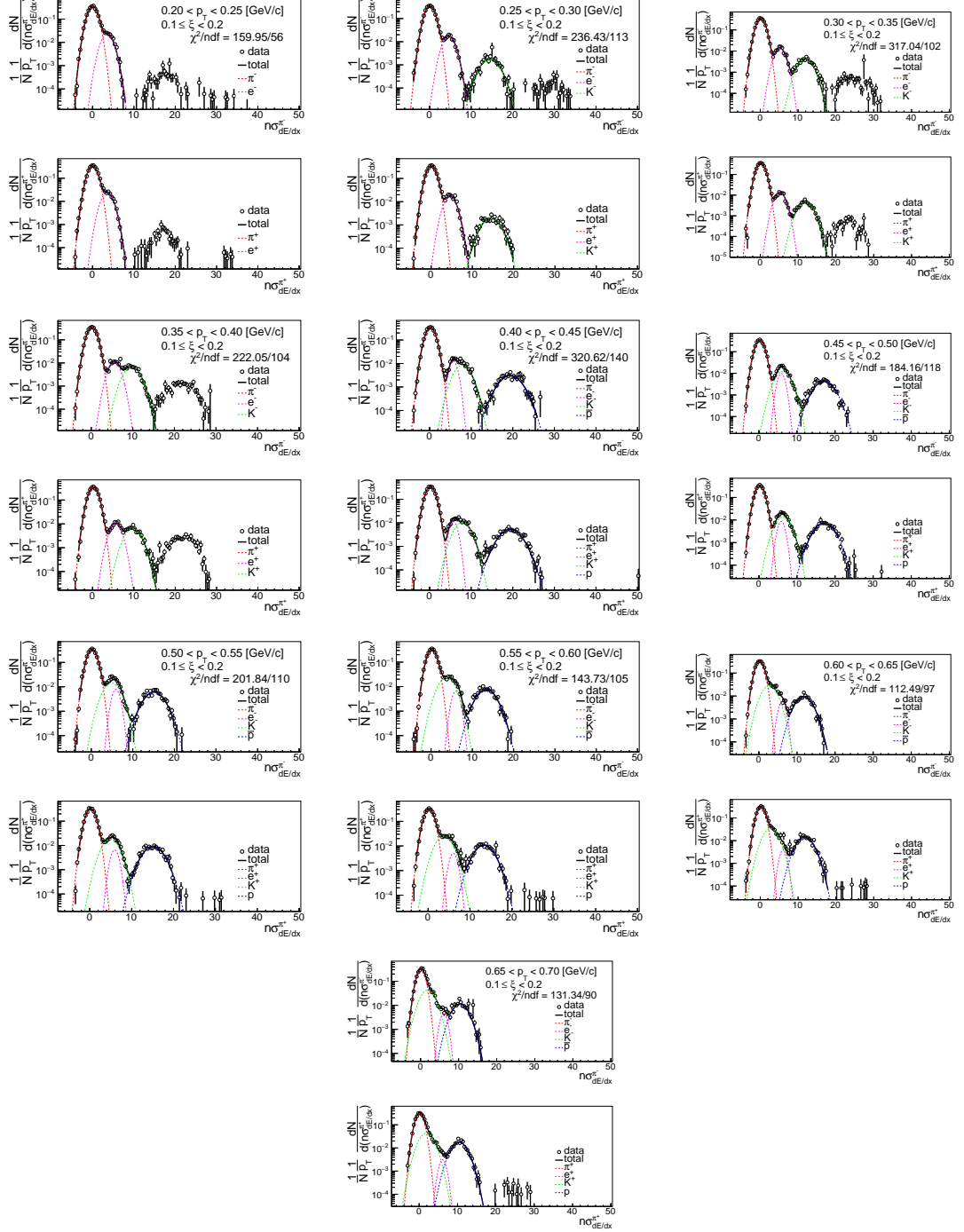


Figure B.3: Distributions of  $n\sigma_{dE/dx}^{\pi^\pm}$  for  $\pi^\pm$  in SD interactions with  $0.1 < \xi < 0.2$ .

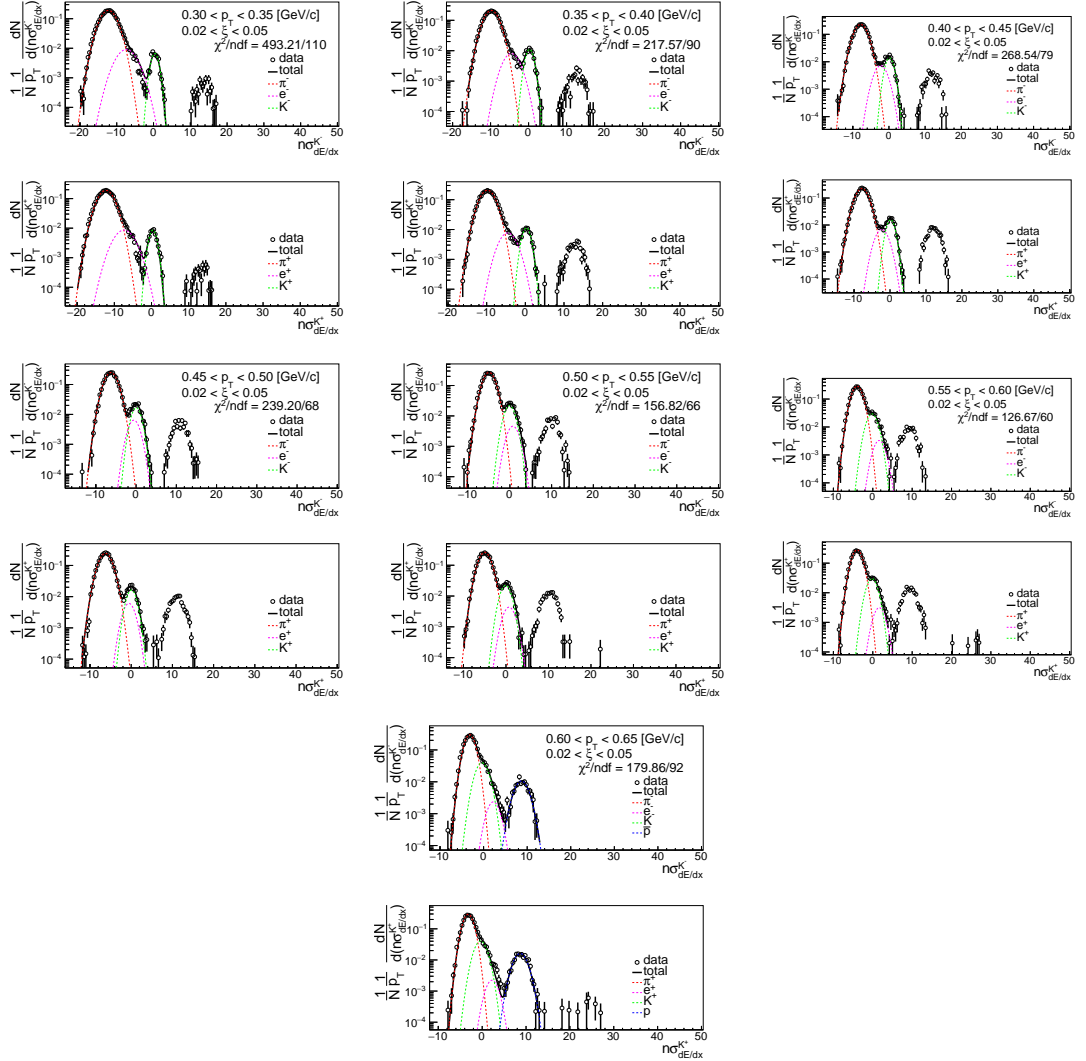


Figure B.4: Distributions of  $n\sigma_{dE/dx}^{K^\pm}$  for  $K^\pm$  in SD interactions with  $0.02 < \xi < 0.05$ .

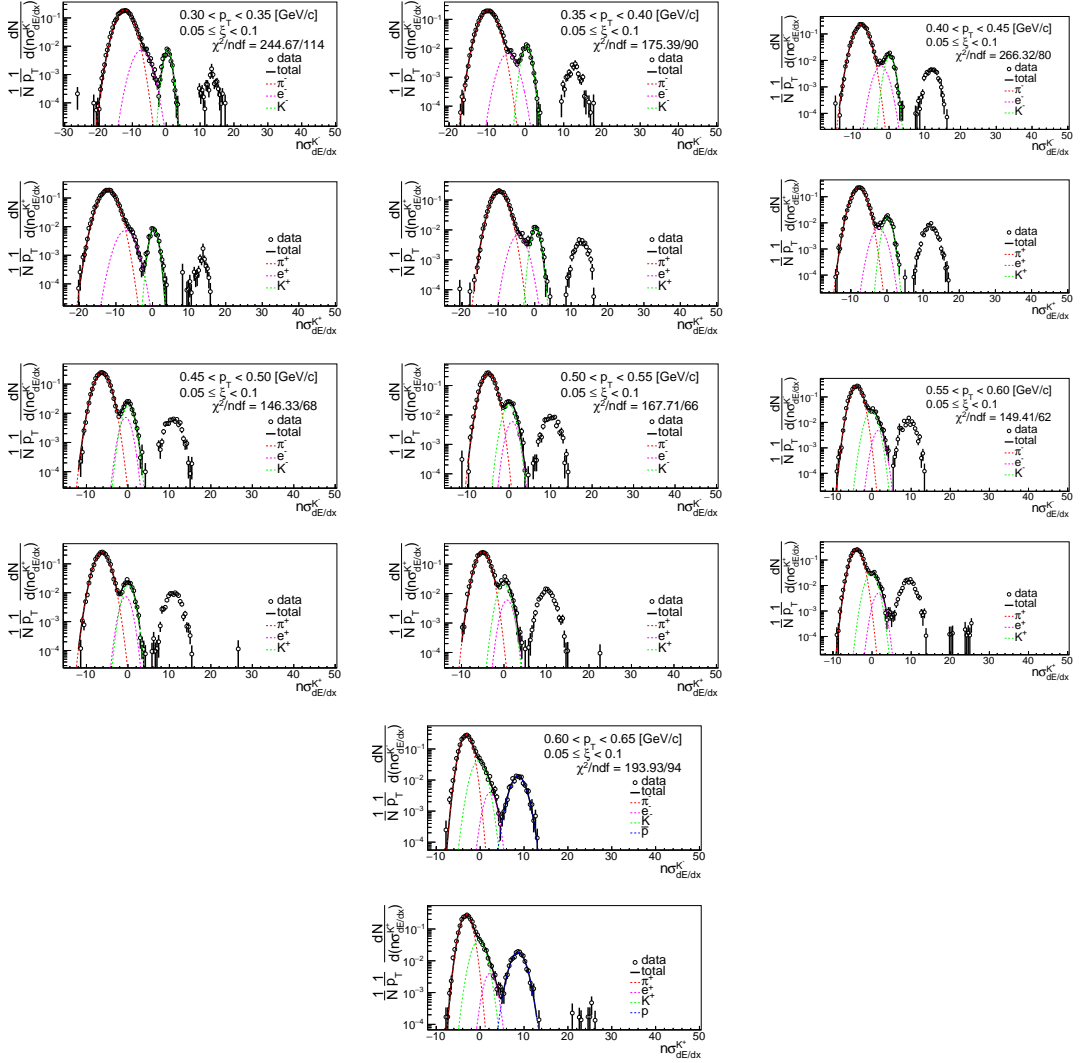


Figure B.5: Distributions of  $n\sigma_{dE/dx}^{K^\pm}$  for  $K^\pm$  in SD interactions with  $0.05 < \xi < 0.1$ .

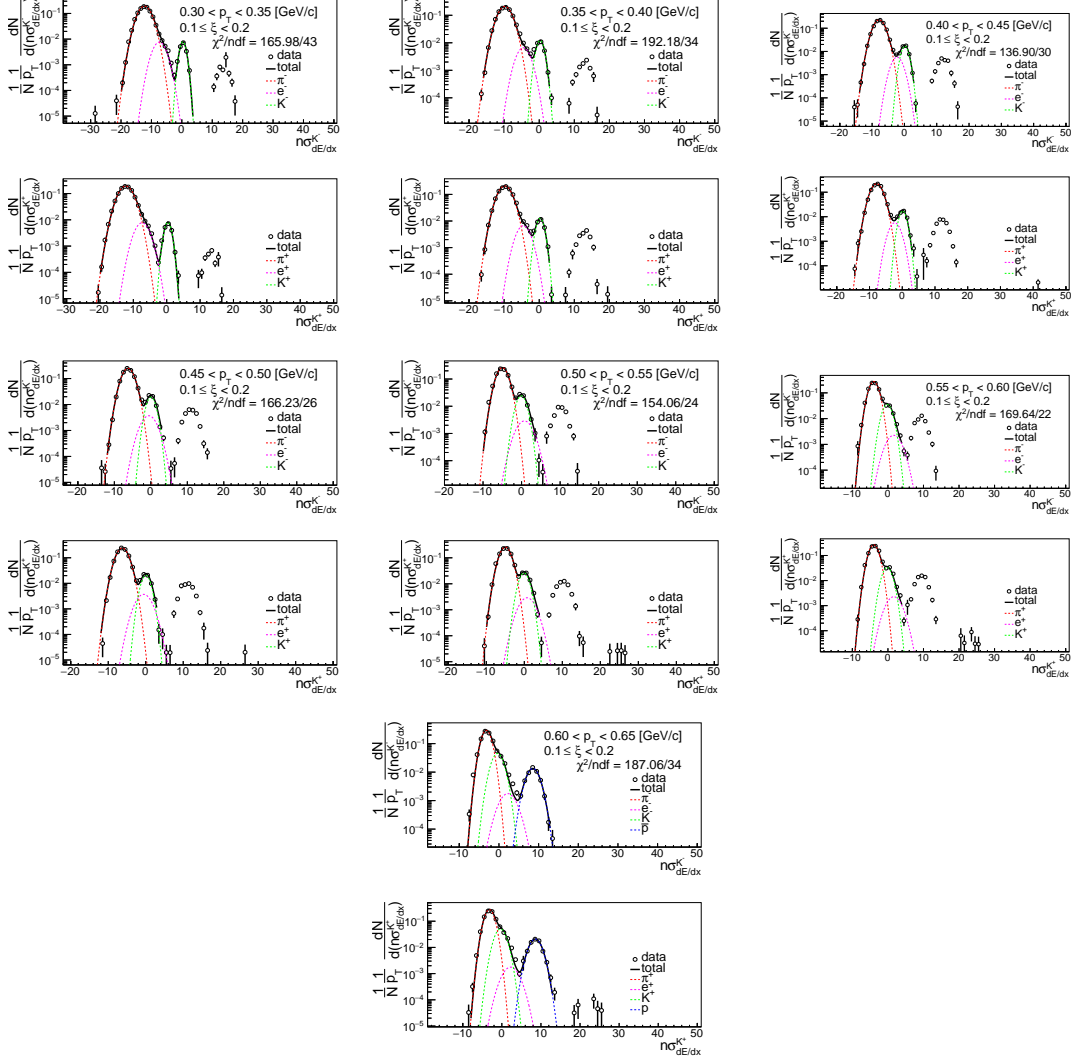


Figure B.6: Distributions of  $n\sigma_{dE/dx}^{K^\pm}$  for  $K^\pm$  in SD interactions with  $0.1 < \xi < 0.2$ .

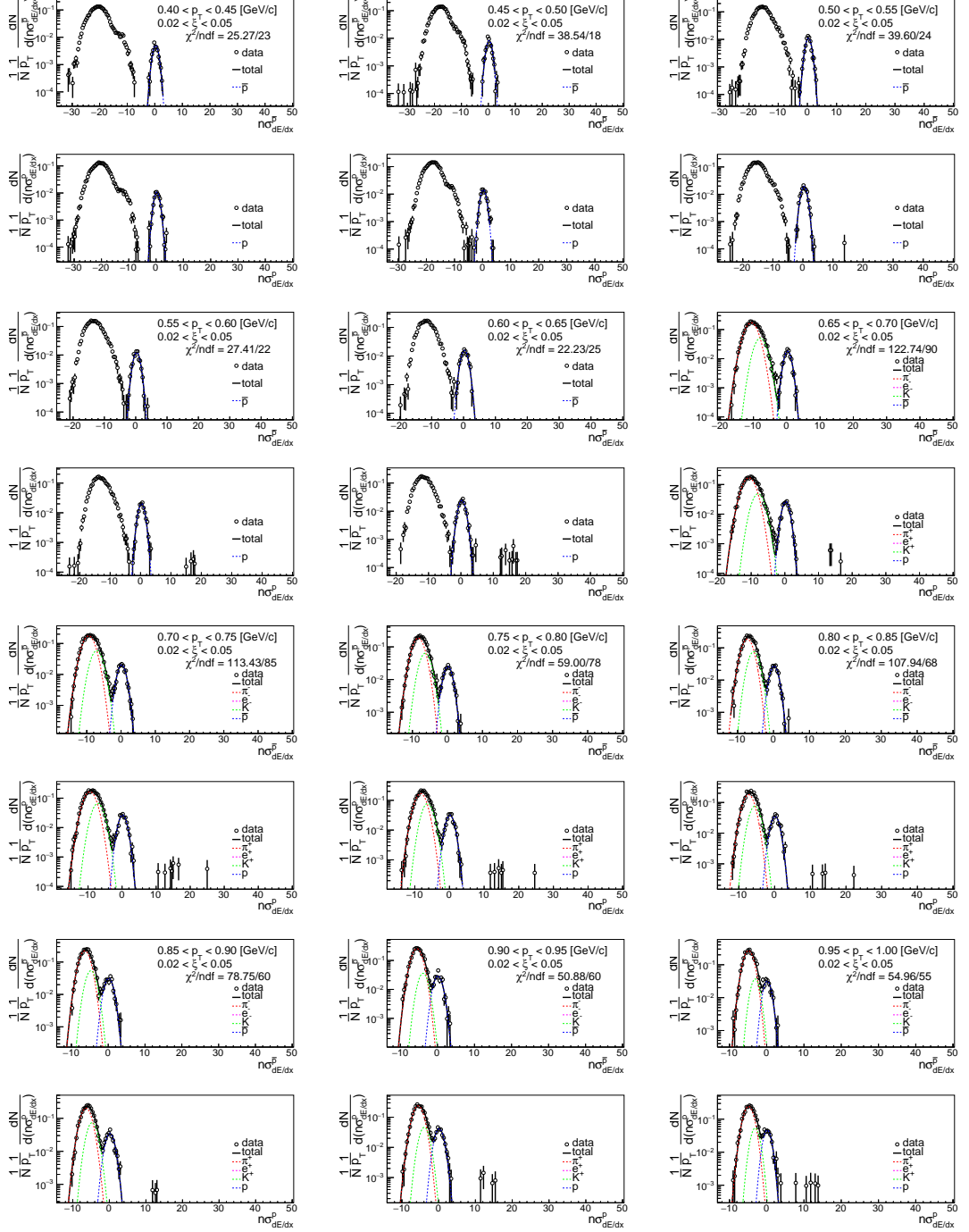


Figure B.7: Distributions of  $n\sigma_{dE/dx}^{\bar{p}, p}$  for  $\bar{p}, p$  in SD interactions with  $0.02 < \xi < 0.05$ .

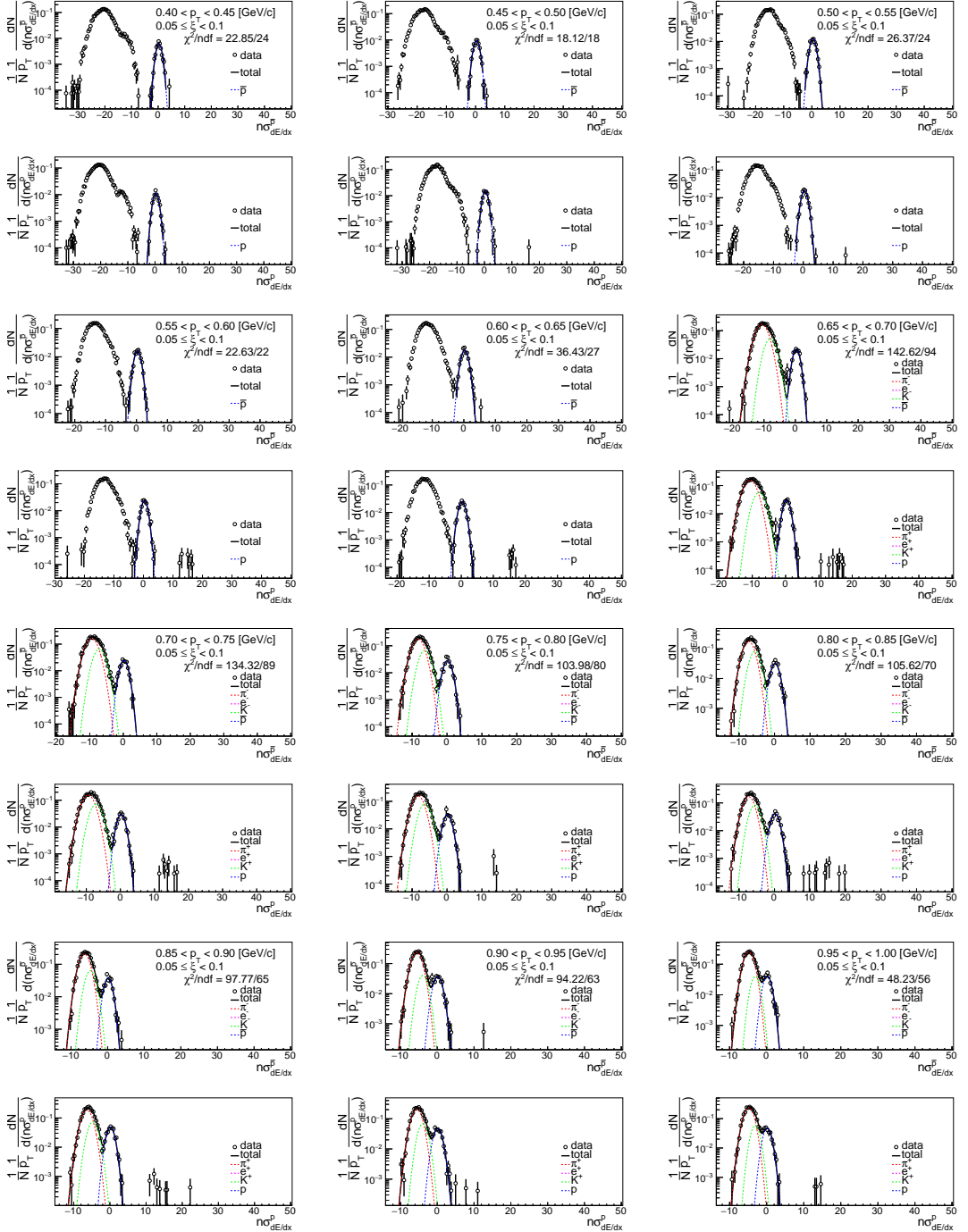


Figure B.8: Distributions of  $n\sigma_{dE/dx}^{\bar{p},p}$  for  $\bar{p}, p$  in SD interactions with  $0.05 < \xi < 0.1$ .

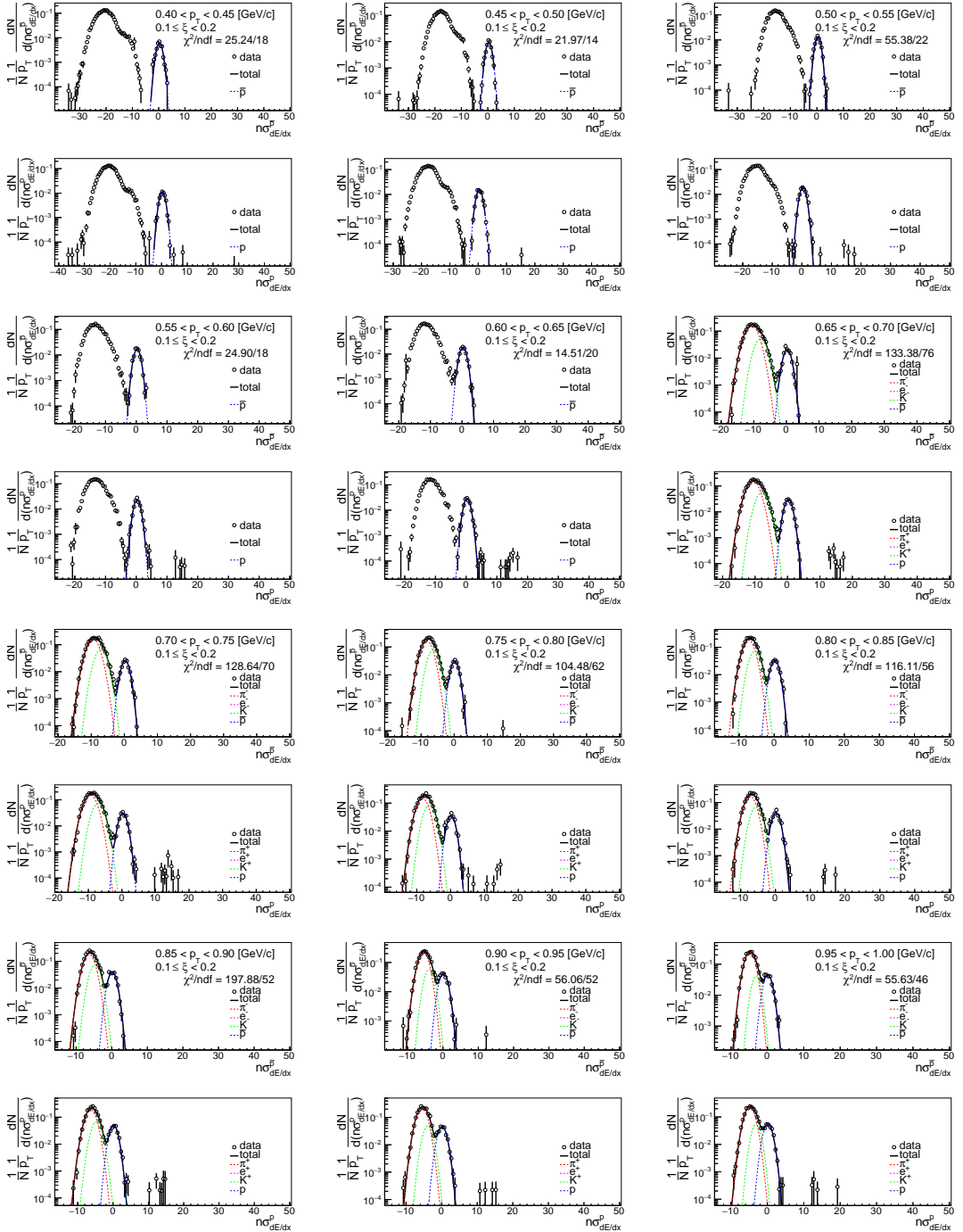


Figure B.9: Distributions of  $n\sigma_{dE/dx}^{\bar{p},p}$  for  $\bar{p}, p$  in SD interactions with  $0.1 < \xi < 0.2$ .